MEMOIRE

présenté à l'Université des Sciences et Technologies de Lille

par

Ludger WIRTZ

pour obtenir

L'HABILITATION à DIRIGER des RECHERCHES

Theoretical Spectroscopy of Boron Nitride Nanotubes and Graphene

Soutenue publiquement le 10 décembre 2008 devant le jury composé de

Rapporteurs :

Fabrizio Cleri	IEMN, Villeneuve d'Ascq, France
Annick Loiseau	ONERA, Châtillon, France
Stephan Roche	CEA, Grenoble, France

Examinateurs :

Christophe Delerue	IEMN, Villeneuve d'Ascq, France
Francesco Mauri	Université Pierre et Marie Curie, Paris, France
Angel Rubio	Universidad del País Vasco, San Sebastián, Espagne

Résumé

Le but de ce travail théorique est de présenter une vue détaillée de la spectroscopie des nanotubes de nitrure de bore et du graphène. Ces deux matériaux ont récemment attiré considerablement l'attention dans le domaine des nanosciences et leur caractérisation par spectroscopie est d'une grande importance.

Nous présentons les différentes techniques de spectroscopie qui sont frequemment utilisées pour les nanotubes de BN. Nous résumons les données expérimentales et fournissons des calculs détaillés issus de la spectroscopie Raman, de la spectroscopie par absorption optique, de la luminescence et de la spectroscopie par perte d'energie (EELS). Le couplage de toutes ces méthodes permet la caractérisation de la structure électronique et des propriétés vibrationelles des nanotubes de BN. Les spectres optiques sont dominés par un exciton de forte énergie de liaison dont le calcul nécessite l'utilisation des techniques du problème à N-corps. Il en résulte que le gap optique des nanotubes de BN d'un diamètre supérieur à 7 Å est indépendant du diamètre et de la chiralité (contrairement aux nanotubes de carbone).

En ce qui concerne le graphène et le graphite nous présentons des calculs de la structure de bandes électroniques et des relations de dispersion des phonons. Il est démontré dans les deux cas que l'inclusion des effet de correlation electron-electron (au niveau de l'approximation GW) implique des modifications importantes par rapport aux calculs classiques DFT. On constate que la vitesse de Fermi du graphène (pente du croisement linéaire des bandes π au point de Dirac) est renormalisé d'environ 17%. La pente de la bande du phonon optique la plus haute autour du point de haute symmetrie K est augmentée d'un facteur deux. Ces résultats sont importants pour la description des récentes mesures ARPES et pour la compréhension de la dispersion des pics dans les spectres Raman en fonction de l'energie du laser.

Abstract

The aim of this work is to give theoretical insight into the spectroscopy of Boron Nitride nanotubes and of graphene. These two materials have recently received considerable attention in the field of nanoscience. Their characterization by spectroscopy is therefore of great importance.

We review the different spectroscopic techniques that are currently used for BN-nanotubes. We summarize the available experimental data and provide detailed calculations on Raman spectroscopy, optical absorption spectroscopy, luminescence spectroscopy, and electron-energy loss spectroscopy. The combination of all those methods allows for a fairly complete characterization of the electronic structure and of the vibrational properties of BN tubes. The optical spectra are dominated by a strongly bound exciton whose calculation requires the use of many-body perturbation theory. The resulting optical gap of BN-tubes with diameter larger than 7 Å is independent of tube diameter and chirality (in contrast to the case of carbon nanotubes).

For graphene and graphite, we present calculations of the electronic band-structure and of phonon dispersion relations. It turns out that in both cases, the proper inclusion of electron-electron correlation (on the level of the GW-approximation) leads to important modifications with respect to standard DFT calculations. The Fermi velocity in graphene (slope of the linear crossing of the π-bands at the Dirac point) is renormalized by 17%. The slope of the highest-optical phonon branch around the high-symmetry point K is increased by a factor of two. These findings are important to describe recent ARPES measurements and to understand the dispersion of the dominant Raman peaks as a function of the laser light energy.

Contents

Preface

This manuscript describes my scientific work on the theoretical spectroscopy of nanostructures. The work was performed during my time as a Postdoc in San Sebastián (march 2002 - september 2004) and my time as a CNRS researcher at the IEMN (since october 2004).

My postdoc position was financed through the European network COMELCAN ("Coupled mechanical and electronic properties of carbon nanotubes bases systems"). Since this was mainly a network of experimental teams, I worked a lot in collaboration with experimentalists. In particular, I worked on the prediction and interpretation of measured spectra of Boron Nitride nanotubes. The 1st chapter, "Optical and vibrational properties of boron nitride nanotubes", is a slightly modified reprint of a book chapter that I have written together with A. Rubio for the book *B-C-N Nanotubes and Related Nanostructures*, edited by Y.K. Yap, which will appear in Springer (2009). Besides a general overview about the spectroscopy of BN tubes, it is in particular a summary of my own work on the theoretical aspects of the different spectroscopical methods. I have included a reprint of my two key publications in this field ([19] and [21]).

In Lille, I started a project on graphene. This was motivated by the experimental production of single graphene-layers[1] and by my earlier experience on the electronic and vibrational spectra of hexagonal systems. Graphene has a very simple structure (just two atoms in the periodic unit cell), but due to the linear crossing of two bands at the Fermi surface, it displays very interesting physical properties. Even seemingly simple properties such as the electronic band dispersion and the phonon dispersion continue to present surprises in experiment and theory. The interpretation of Raman spectra of single and double-layer graphene flakes lead us to conclude that there was a deviation from previously measured and calculated dispersion relations for the highest optical branch around the high symmetry point K. This deviation and its explanation is the subject of the second chapter entitled "Excitations in Graphene and Graphite".

So far, I have been using ab-initio methods for the calculation of electronic properties of materials. Even with the tremendous increase in computer power during the last years, ab-initio methods are reaching their limit if one tries to describe "large" nanostructures, i.e., structures with many atoms in the unit-cell. One of my current activities that extends into the future lies in the development of a computational code that combines tight-binding methods with many-body perturbation theory. This tool should enable the routine calculation of systems with several hundres of atoms and yet include electron-electron and electron-hole interaction whenever those are important. This activity is briefly described in the outlook.

In general, references are printed as foot notes. References in square brackets refer to my own publication list (Appendix A).

---

[1] K.S. Novoselov et al., Science **306**, 666 (2004)

Acknowledgments

The work described in this habilitation report has been done in collaboration. I would like to express my profound gratitude towards all the people who contributed in one way or the other to these activities.

- *Angel Rubio* convinced me to come as a postdoc to San Sebastián where he introduced me to the world of nanotubes and to the wonders of Basque cuisine. He has been a constant source of ideas for new projects and got me in touch with many collaborators.
- *Christophe Delerue* has been my “responsable scientifique” at IEMN. He helped me to settle down in the French scientific community and, together with *Guy Allan*, introduced me to the amazing things that tight-binding techniques can do.
- Life and work in San Sebastián would not have been the same without the many discussions and dinners with *Andrea Marini*, *Miguel Marques* and *Alberto Castro*. Andrea taught me the methods of many-body perturbation theory and it has been a great pleasure to work with him on the excitonic effects in one-dimensional systems.
- *Valerio Olevano* and *Lucia Reining* welcomed me for several research visits at the Ecole Polytechnique and guided my first steps in the calculation of optical properties.
- With *Silvana Botti*, I have had a very fruitful collaboration in the framework of a joint young researchers' project of the French National Research Agency.
- *Claudio Attaccalite* worked as a postdoc at IEMN and contributed an important part to the work presented here.
- A lot of motivation for my work on boron nitride nanotubes came from the experimental achievements of *Annick Loiseau*, *Raul Arenal de la Concha*, and *Perine Jaffrennou*.
- With *Michele Lazzeri* and *Francesco Mauri* I have had very pleasant collaborations on the calculation of Raman spectra and on the electron-phonon coupling in graphene.
- It has been very stimulating to work with *Christoph Stampfer* on so different subjects as the development of semiclassical methods in mesoscopic transport and the interpretation of Raman spectra of single and few-layer graphene.
- Motivation for the work on graphite came also from the excellent experimental work of *Alexander Grüneis* and *Thomas Pichler* (ARPES) and of *Jorge Serrano* (inelastix X-ray scattering).

- *Thierry Melin*, *Heinrich Diesinger*, and *Catherine Priester* helped me a lot to settle down in Lille and at IEMN.
- Last but not least I would like to thank the reviewers of this habilitation report: *Fabrizio Cleri*, *Stephan Roche*, and *Annick Loiseau*, as well as the members of the jury: *Francesco Mauri*, *Angel Rubio*, and *Christophe Delerue*.

Chapter 1

Optical and Vibrational Properties of Boron Nitride Nanotubes

1.1 Introduction

Boron nitride (BN) is isoelectronic to carbon and displays, among others, a graphite-like hexagonal phase (h-BN). The elastic constants are very similar (although smaller), but the polar nature of the BN bond leads to significant changes in the electronic structure of h-BN as compared to graphite. While graphite is a semimetal (zero bandgap in the single sheet), h-BN has a large bandgap (above 6 eV). Furthermore, its high thermal stability and relative chemical inertness distinguishes it from its carbon counterpart.

Briefly after the discovery of carbon nanotubes and based on the similarities among graphite and other sp^2-like bonded materials, the existence of Boron-Nitride nanotubes[1] [2] was predicted. Synthesis of these nanotubes was achieved shortly afterwards[3]. In contrast to C-nanotubes which can be either semiconducting or metallic, depending on the chirality of the tube, BN-nanotubes are always semiconducting with a large band gap that is nearly independent of the tube diameter, chirality and whether the nanotube is single-walled, multi-walled, or packed in bundles[1] [2]. A structural difference between BN and C tubes is that for tubes with small diameter, the BN system buckles with the B atoms moving inward and the N atoms outward [2]. This results in a dipolar double cylinder shell structure. The uniform electronic properties and the dipolar barrier suggest that BN nanotubes may have significant advantages for applications in electronic and mechanical devices. Furthermore, the bottom of the conduction band is a nearly free electron like-state (NFE). This state remains the bottom of the conduction band even in the multiwall case and, in the case of n-type doping, will play an important role for potential applications in field emission devices and molecular transport.

Several spectroscopic methods are commonly used for the identification and characterization of BN nanotube samples. High-resolution transmission electron (HRTEM) allows for a quick view at the scene with almost atomic resolution. Scanning tunneling microscopy and spectroscopy (STM/STS) allow to get atomic resolution and to map the electronic structure

---

[1] A. Rubio, J. L. Corkill, and M. L. Cohen, Phys. Rev. B **49**, 5081(R) (1994).

[2] X. Blase, A. Rubio, S. G. Louie, and M. L. Cohen, Europhys. Lett **28**, 335 (1994).

[3] N.G. Chopra, R.J. Luyken, K. Cherrey, V.H. Crespi, M.L. Cohen, S.G. Louie, and A. Zettl, Science **269**, 966 (1995).

to the underlying nanotube geometry. In optical spectroscopy, using laser light, the spatial resolution is lost. However, alternative information about the band structure and the vibrational properties of the constituents can be gained. Optical absorption spectroscopy probes the electronic band structure by direct excitation of an electron from the valence to the conduction band. Since BN tubes have a wide bandgap, either multiphoton processes or UV light are necessary for this process to occur in BN nanotubes. The detailed knowledge of the optical properties of BN tubes is indispensable for their characterization and may help to guide their use as nanoelectronic devices: e.g, BN nanotubes have been used to build a field effect transistor[4] and the observed high yield of ultraviolet luminescence[5] of bulk hexagonal BN suggest the use of BN nanotubes as ultraviolet light sources. Therefore, it is important to know about possible excitonic states whose dominant influence has been shown for the opto-electronic properties of carbon nanotubes.

At lower energy, infrared (IR) absorption probes the direct excitation of phonons. Raman spectroscopy probes the excitation of phonons by measuring the frequency shift in elastically scattered laser light. In contrast to carbon nanotubes, in BN tubes the Raman scattering is non-resonant due to the large bandgap of the tubes. The resulting spectra are, therefore, weaker in intensity and must be carefully separated from a possible overlap by resonant Raman scattering from contaminants. On the other hand, the efficiency of IR-absorption is enhanced by the polarity of the material and gives rise to a much more pronounced IR spectrum than in the case of carbon tubes where the IR spectra have very little structure and can hardly be distinguished from the IR spectrum of graphite For the interpretation of such spectra, an accurate knowledge of the phonon frequencies as a function of tube diameter and chirality together with the corresponding photoabsorption cross-section is indispensable. Therefore, we present in detail the calculations of phonons in BN nanotubes and their symmetry analysis. For zigzag and chiral nanotubes, the set of infrared-active modes is a subset of the Raman-active modes. In particular, the radial breathing mode is not only Raman but also infrared active. However, for armchair tubes, the sets of infrared- and Raman-active modes are disjoint.

This chapter is organized as follows. First we provide a detailed description of the absorption spectra of bulk hexagonal BN and the tubes, making a connection between the two and highlighting the relevance of many-body correlations (quasiparticle and excitonic corrections). Then we will address some important issues related to the high yield luminescence in BN samples and how it can be externally controlled and modified by the presence of intrinsic defects in the samples. Furthermore we will discuss the excitation of plasmons in electron-energy loss spectroscopy. The second part of the chapter will be devoted to the phonons and the infrared and Raman spectroscopy of BN tubes.

1.2 Optical absorption spectra of BN nanotubes

Due to the large band gap of hBN (> 6 eV), optical absorption only starts in the ultraviolet regime. Thus, optical absorption spectra of BN tubes are difficult to measure and may not be the method of choice for the characterization of tubes. However, their understanding on

---

[4] M. Radosavljević, J. Appenzeller, V. Derycke, R. Martel, P. Avouris, A. Loiseau, J.-L. Cochon, D. Pigache, Appl. Phys. Lett. **82**, 4131 (2003).

[5] K. Watanabe, T. Taniguchi and H. Kanda, Nature Materials **3**, 404 (2004).

a theoretical level is of utmost importance as a first step towards the understanding of luminescence in BN tubes. Furthermore, we will see that the absorption spectra are conceptually interesting because they are dominated by a strongly bound exciton.

1.2.1 Absorption spectra in the independent-particle picture

The absorption cross section of an isolated nanotube is given by the imaginary part of its polarizability (per unit length). To first order, absorption of a photon of energy $\hbar\omega$ is commonly explained through the vertical excitation of an electron from a state $|n_v, k>$ with energy E_v in the valence-band to a conduction-band state $|n_c, k>$ of energy E_c:

$$Im[\alpha(\omega)] \propto \int dk \sum_{n_v n_c} |\langle n_v, k|D|n_c, k\rangle|^2 \, \delta(E_c - E_v - \hbar\omega). \tag{1.1}$$

The matrix element of the dipole operator D "selects" only certain "allowed" transitions. Since the photon carries vanishing momentum, both valence and conduction band states must have the same wave vector k. Eq. (1.1) corresponds to the so-called random-phase approximation (RPA). It is also called the "one-electron" or "independent-particle" picture of absorption. The latter name stems from the assumption that the Coulomb potential in which the active electron is moving and which is caused by the charge density of all other electrons is static and independent of the state of the active electron. While this assumption is reasonable for many materials, we will see below that it has serious deficiencies for hBN and BN nanotubes. Nevertheless, it is instructive to start the exploration of the absorption spectra of BN nanotubes in the independent-particle picture.

The electronic structure of BN nanotubes can be constructed from the electronic structure of the single sheet via the zone-folding procedure. Therefore, we present in Fig. 1.1 the band-structure of an hBN sheet and of a (6,6) armchair BN-nanotube. The band-structure of the sheet is characterized by the large direct gap at the K-point.[6] According to the zone-folding procedure, the band-structure of the tube can be obtained by cutting the band-dispersion of the sheet along certain parallel lines in the reciprocal space (vertical black lines in the grey-shaded area of Fig. 1.1 c). The distance of the lines is determined by the quantization of the wave-vector component $K_\perp$ along the tube circumference. The different lines correspond to different angular momenta (quantum number m) along the axis of the tube. Comparing the band-structure of the sheet to that of the tube, we see that the highest valence band and the lowest conduction band of the tube can be directly obtained from the π and π^* bands of the sheet along the line $M \rightarrow K$ and beyond (see red line in panel c). The wave-functions of the π and π^* bands are predominantly composed of atomic p_z orbitals (i.e., p orbitals with an orientation perpendicular to the plane). We show in Fig. 1.2 the corresponding wave-functions for the sheet at the point K. The π-band wavefunction is predominantly located at the nitrogen atoms and the π^*-band wavefunction is mostly located at the boron atoms. This is due to the higher electronegativity of nitrogen. It is the strong difference in electronegativity between B and N that leads to the large band-gap. (In a graphene sheet, where both atoms

---

[6] Much can be written about the exact value of the gap. For the dispersion in Fig. 1.1, we have used density-functional theory (DFT) and the local-density approximation (LDA) for the exchange-correlation functional. This yields a gap of 4.5 eV. The exact value of the band-gap is discussed further in the text.

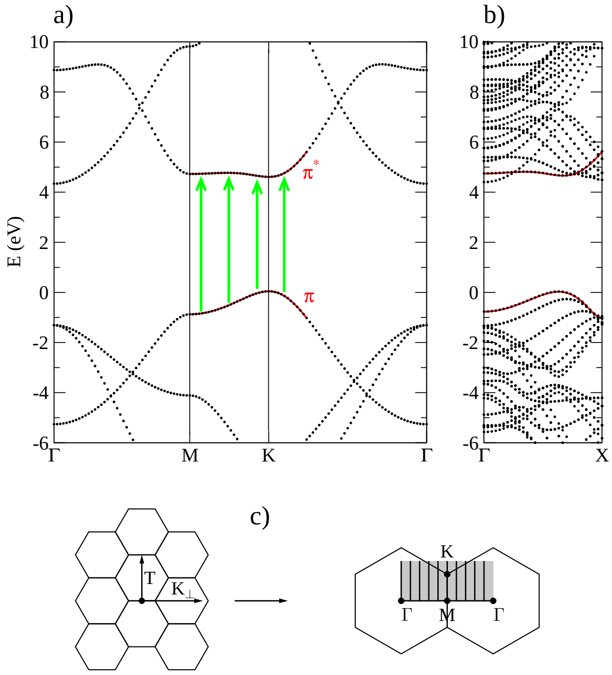

Figure 1.1: Band-structure (calculated with DFT-LDA) for the single sheet of hBN (a) and for the (6,6) BN nanotube (b); c) demonstrates how the band-structure of the tube can be obtained by cutting the band-structure of the sheet along certain lines (zone-folding): The left panel shows a piece of a hBN sheet that is roled up along the vector $K_\perp$, thus forming an armchair tube. The right panel shows the corresponding reciprocal space with quantized values of the momentum in circumferential direction.

in the unit-cell are equivalent, The π and π^* bands are degenerate at K, leading to the linear crossing of the two bands.)

In order to understand how an absorption spectrum is constructed via Eq. (1.1), we look in the following at the RPA-spectrum of a single sheet of hBN and of the (6,6) nanotube. Fig. 1.3 shows the RPA-absorption spectrum of the sheet. In the low energy regime ($<$ 10 eV) and for for light-polarization parallel to the sheet (panel a), the dipole-matrix element in Eq. (1.1) only selects transition from the π to the π^* band (green arrows in Fig. 1.1). The onset of the spectrum is at 4.5 eV which corresponds to the direct gap of the sheet at K. The peak at 5.7 eV stems from the M-point where the π and π^* bands display saddle-points and the joint density of states has a maximum. If the light is polarized perpendicularly to the sheet (Fig. 1.3 b), the π-π^* transitions are dipole-forbidden. Optical absorption is due to σ-π^* and π-σ^* transitions and the onset of the RPA-spectrum is only at about 10 eV. Fig. 1.3 also demonstrates the effect of depolarization. The dashed line shows the spectrum calculated with Eq. (1.1). The external field polarizes the charge distribution of the sheet, creating a layer of dipoles. This dipole layer, in turn, leads to an induced electric field that is directed opposite to the external field. The absorption spectrum must therefore be calculated self-consistently. (Mathematically, this corresponds to taking into account off-diagonal elements of the dielectric tensor in reciprocal space). The resulting spectrum (solid line in Fig. 1.3) is strongly reduced in oscillator strength in the energy range below 15 eV. For the parallel polarization (Fig. 1.3

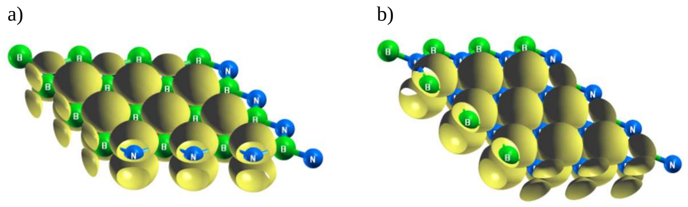

Figure 1.2: Wave-functions in the single BN-sheet of a) the π (N-based) and b) the π^* (B-based) band at K. Green/blue spheres denote Boron/Nitrogen atoms

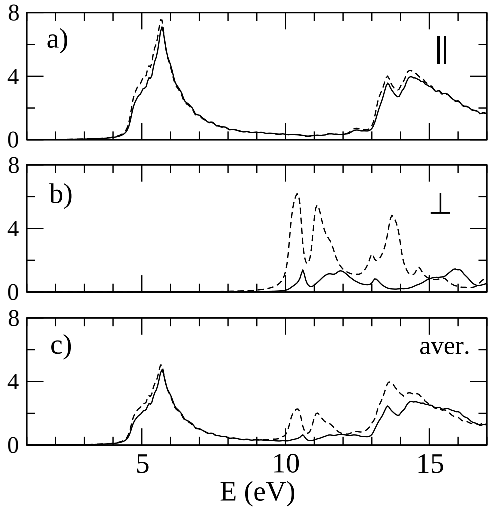

Figure 1.3: RPA-absorption spectrum of a single BN sheet with (solid lines) and without (dashed lines) depolarization effects: a) light-polarization parallel to the plane, b) polarization perpendicular to the plane, c) averaged spectrum.

a), the depolarization effects have only a minor influence. The direction-averaged spectra (Fig. 1.3 c) is dominated by the contribution from the parallel polarization.

In Fig. 1.4 a) we present the RPA spectra of bulk hBN, of the single-sheet of hBN and of different BN nanotubes with diameters ranging from 2.8 Å for the purely hypothetical BN(2,2) tube to 9.7 Å for the BN(7,7) tube which is at the lower border of the range of experimentally produced tubes. The light polarization is set parallel to the planes or tube-axis, respectively, because, as discussed above, depolarization effects strongly suppress the absorption in the perpendicular direction. For the bulk and for the single-sheet the spectra are almost indistinguishable. This is due to the relatively weak interaction between neighboring sheets in the bulk phase.

Since the bands of the tubes can be constructed from the sheet via the zone-folding procedure, the RPA spectra of the tubes display transitions at the same energies as in the sheet. With increasing diameter, the shape of the tube spectra converges rapidly towards the

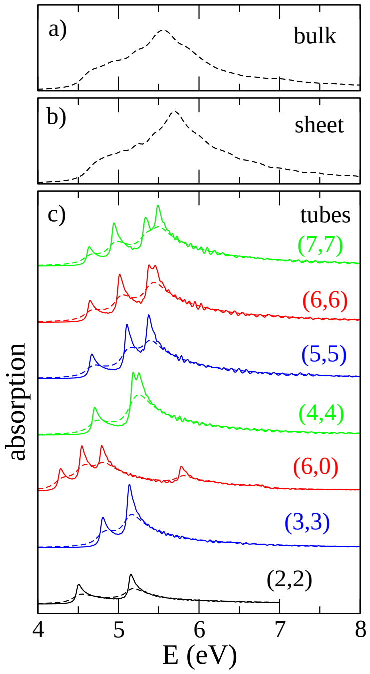

Figure 1.4: RPA-absorption spectra of (a) bulk hexagonal BN, (b) a single sheet of hexoganl BN, (c) six different BN tubes with increasing diameter d. Solid lines are calculated with a Lorentzian broadening of 0.025 eV, dashed lines with a broadening of 0.1 eV.

sheet spectrum, in particular if plotted with a Lorentzian broadening of 0.1 eV (corresponding roughly to usual experimental broadening). A calculation with a fine broadening of 0.025 eV (and a correspondingly fine sampling with 200 $\mathbf{k}$-points in the first Brillouin zone), reveals additional fine-structure below 5.5 eV. This structure is due to the van-Hove singularities in the one-dimensional density of states. For tubes with larger radii, the density of the fine-structure peaks increases and the RPA spectrum approaches that of the 2D sheet. The onset of absorption is constantly at 4.7±0.1 eV for all tubes except for the (2,2) and the (6,0) tube (and other small diameter zigzag tubes) where the gap is lowered due to curvature effects[1]. A very detailed discussion of the RPA absorption spectra can be found in Ref. [7]. We would like to emphasize however, that for BN materials, the RPA-absorption spectra are of purely academic interest. We will discuss below that correlation effects strongly modify the shape of the spectra (i.e., the position and strength of the main peak-structure and the onset of the continuum).

---

[7] G. Y. Guo and J. C. Lin, Phys. Rev. B **71**, 165402 (2005).

1.2.2 Influence of correlation effects on the absorption spectra

What is the practical meaning of "correlation effects" in the context of optical absorption? A photon is absorbed by exciting an electron from the valence band to the conduction band. For a quantitative prediction of the spectrum, we thus need to know the exact size of the band-gap. Furthermore, we have to take into account that the excited electron may interact with the hole that is left behind in the valence band. These studies are done using many-body perturbation theory with a self-energy formalism in which electron-correlations are treated on the level of the GW approximation while the electron-hole attraction is dealt with by means of a static Bethe-Salpeter equation.

The band gap problem

The band-gap is defined as the energy difference between the lowest unoccupied molecular orbital (LUMO) and the highest occupied molecular orbital (HOMO). The energy of the HOMO is the energy that it would take to extract an electron from that orbital. Experimentally, the HOMO energy can be directly measured by photoemission spectroscopy. The energy of the LUMO is the energy that one gains (or looses) by adding an electron to the neutral cluster. Experimentally, the LUMO energy can be measured by inverse photo-emission (an electron-beam of a specific energy is directed at a surface and the energy of the emitted photons is measured). For strongly insulating materials both photo-emission and inverse photo-emission are very difficult to perform (the accuracy in direct photoemission, reaching meV resolution, is at present much larger than for inverse photoemission). Hence, for bulk hBN (and equally for the single-sheet and for the tubes), no direct experimental data for the band-gap exists and we have to rely on theoretical predictions.

The situation for theorists is similarly difficult. We discuss here briefly the performance of the two most frequently used methods for band-structure calculations: the Hartree-Fock approximation (HFA) and density functional theory (DFT). Let's assume that in both approximations, the HOMO energy is described properly. The problem lies then in the LUMO energy. If an additional electron is attached to the material, it interacts with the other electrons through the dielectrically screened electron-electron repulsion which leads to a polarization of the environment. This is a correlation effect and lowers the energy of the LUMO with respect to an imaginary system where correlation effects are absent. In the HFA, correlation effects are not included (the electron density is the static charge density of the neutral ground-state). Therefore, in general, the HFA severely overestimates the band-gap. DFT in the local-density approximation (LDA) or in the generalized-gradient approximation (GGA) tends to overestimate the screening of additional electrons. This results, in general, in an underestimation of the band-gap. In this way, we obtain for the single sheet of hBN a gap of 4.5 eV in LDA, 4.6 eV in GGA and 14 eV within the HFA! The real band-gap must lie within these limiting values. Using more sophisticated exchange-correlation functionals in DFT, one can get closer to the exact band-gap. With the B3LYP hybrid functional[8], we obtain 6.4 eV. Baumeier et al.[9] report a value of 6.3 eV, using a self-interaction corrected DFT approach. A reliable calculation of the gap can only be achieved taking electron-electron correlation explicitly into

---

[8] A.D. Becke, J. Chem. Phys. **98**, 5648 (1993).

[9] B. Baumeier, P. Krüger, and J. Pollmann, Phys. Rev. B **76**, 085407 (2007).

account. This is achieved in the so-called GW-approximation which will be briefly discussed below. In the GW approximation, the band-gap of the single hBN sheet is 8.1 eV [21].

The only exact way to calculate the band-gap of a material consists in the use of the methods of many-body perturbation theory. Starting from either HFA or DFT wave-functions and energies, the first step is the calculation of the inverse dielectric function ϵ^{-1} on the level of the random-phase approximation. The dielectric function describes how the bare Coulomb-potential V_c between two electrons is screened by the other charges in the material. Within the GW-approximation[10] [11] [12] the quasi-particle energies (single-particle excitation energies), $E_{n\mathbf{k}}$, are calculated by solving the quasi-particle equation.

$$\left[-\frac{\nabla^2}{2}+V_{ext}+V_{Hartree}+\Sigma(E_{n\mathbf{k}})\right]\psi_{n\mathbf{k}}=E_{n\mathbf{k}}\psi_{n\mathbf{k}}. \tag{1.2}$$

Atomic units are used all through this chapter unless otherwise stated. The self-energy $\Sigma = iGW$ is non-local and energy-dependent. It is approximated as the product of the one-particle Green's function G and the dynamically screened Coulomb interaction $W = \epsilon^{-1}V_c$. The resulting energy levels are "true" electron-removal and electron-addition energies, i.e., they include the effect of dynamic screening upon removing an electron from the valence band or adding one to the conduction band, respectively.

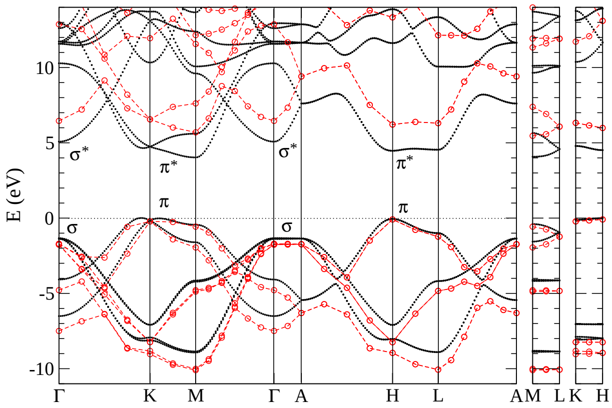

Figure 1.5: Band-structure of bulk hBN: LDA (dotted line), GW-approximation (circles and dashed lines)

In Fig. 1.5, we show the effect of the GW-approximation on the band-structure of bulk hBN[13] [14]. Note that with respect to the band-structure of the single-sheet (see Fig. 1.1), in bulk hBN, the π and π^* bands are split into two bands each. (This is a consequence of the AA'-stacking of the layers in the bulk.) The minimum direct gap of 4.47 eV in LDA is shifted to 6.26 eV in the GW approximation. The large shift points to a strong electron-electron interaction which can be associated with the layered structure of hBN: electrons are mostly

---

[10] M.S. Hybertsen and S.G. Louie, Phys. Rev. B **34**, 5390 (1986).

[11] W.G. Aulbur, L. Jönsson, and J. W. Wilkins, *Quasiparticle calculations in solids* in Solid State Physics, edited by H. Ehrenreich and F. Spaepen (Academic, New York, 2000), Vol. 54, p. 1.

[12] G. Onida, L. Reining, and A. Rubio, Rev. Mod. Phys. **74**, 601 (2002).

[13] X. Blase, A. Rubio, S.G. Louie and M. L. Cohen, Phys. Rev. B **51**, 6868 (1995).

[14] B. Arnaud, S. Lebègue, P. Rabiller, and M. Alouani, Phys. Rev. Lett. **96**, 026402 (2006).

confined to 2-dimensional sheets, hopping between the layers is weak. For the single-sheet, the gap opening is even stronger: from 4.5 eV in LDA to 8.1 in the GW-approximation! This huge GW-shift is due to (i) the fact that electrons are strictly confined to a two-dimensional sheet and (ii) due to the much weaker screening in the isolated sheet as compared to the bulk crystal.

Excitonic effects

In addition to electron-electron (e-e) interaction, the electron-hole (e-h) interaction can play an important role for the quantitative description of absorption spectra. The excited electron in the conduction band and the hole left behind in the valence band interact through an attractive Coulomb potential. As in the case of e-e interaction, the attractive e-h potential is screened through the inverse dielectric function. In many large band-gap materials, the e-h attraction leads to the formation of bound excitons, i.e. discrete states in the band-gap. On a qualitative level, bound excitons can be compared with bound states of the hydrogen atom. In analogy to the hydrogen atom, the Hamiltonian of the exciton can be written as

$$H^{exc}(r) = \frac{p^2}{2\mu^*} - \frac{e^2}{\epsilon r}, \tag{1.3}$$

where r is the electron-hole distance and μ^* is the reduced effective mass which is the average of the electron and hole effective masses: $\mu^* = (m_e^* m_h^*)/(m_e^* + m_h^*)$. As in the case of hydrogen, the eigenvalues form a Rydberg series of bound states with energies

$$E_n^{exc} = E_c - \frac{1}{2n^2}\frac{\mu^* e^4}{2\epsilon^2\hbar^2}, \tag{1.4}$$

where E_c is the minimum of the conduction band. The "Bohr radius" of the lowest bound exciton is

$$a_0^{exc} = \frac{\hbar^2\epsilon}{\mu^* e^2}. \tag{1.5}$$

For typical semiconductors, the dielectric constant is of the order of 10 and the reduced effective mass is smaller than half the free electron mass. This leads to typical excitonic binding energies of several tens of meV and to Bohr radii that are large compared to the inter-atomic distance in the lattice. In the excitonic state, the electron is on the average quite far from the hole from where it was excited. This justifies the use of the average dielectric constant in Eq. (1.3). If the dielectric constant is small ($\epsilon \rightarrow 1$), i.e., if dielectric screening is weak, the excitonic radius shrinks to the order of the lattice constant and the binding energy can attain several hundred meV. In this case, however, the use of the simple excitonic Hamiltonian (Eq. (1.3)) is no longer justified.

A precise calculation of the exciton energies has to take into account the band structure of the material (going beyond the simple effective mass approach of Eq. (1.3)). Furthermore, the non-locality of the screening has to be taken into account. This is achieved by the Bethe-Salpeter equation[15] [12] [16]:

$$(E_{c\mathbf{k}} - E_{v\mathbf{k}})A^S_{vc\mathbf{k}} + \Sigma_{\mathbf{k}'v'c'} \langle vc\mathbf{k}|K_{eh}|v'c'\mathbf{k}'\rangle A^S_{v'c'\mathbf{k}'} = \Omega^S A^S_{vc\mathbf{k}}. \tag{1.6}$$

---

[15] G. Strinati, Phys. Rev. B **29**, 5718 (1984).

[16] M. Rohlfing and S.G. Louie, Phys. Rev. Lett. **81**, 2312 (1998).

Here, the excitons are expressed in the basis of electron-hole pairs (i.e., vertical excitations at a given $\mathbf{k}$-point from a state in the valence band with quasi-particle energy $E_{v\mathbf{k}}$ to a conduction-band state with energy $E_{c\mathbf{k}}$. The $A^S_{vc\mathbf{k}}$ are the expansion coefficients of the excitons in the electron-hole basis and the Ω^S are the eigenenergies (corresponding to the possible excitation energies of the system). If the interaction kernel K_{eh} is absent, Eq. (1.6) simply yields $\Omega^S = (E_{c\mathbf{k}} - E_{v\mathbf{k}})$, i.e., the excitations of the system correspond to independent electron-hole pairs. The interaction kernel K_{eh} "mixes" different electron transitions from valence band states v, v' to conduction band states c, c' leading to modified transition energies Ω^s. It is defined by

$$\begin{aligned}\langle vc\mathbf{k}|K^{eh}|v'c'\mathbf{k}'\rangle = & - \int d\mathbf{r} \int d\mathbf{r}' \phi^*_{c\mathbf{k}}(\mathbf{r}) \phi_{c'\mathbf{k}'}(\mathbf{r}) \int d\mathbf{r}_1 \epsilon^{-1}(\mathbf{r}, \mathbf{r}_1) \frac{1}{|\mathbf{r}_1 - \mathbf{r}'|} \phi_{v\mathbf{k}}(\mathbf{r}') \phi^*_{v'\mathbf{k}'}(\mathbf{r}') \\ & + \int d\mathbf{r} \int d\mathbf{r}' \phi^*_{c\mathbf{k}}(\mathbf{r}) \phi_{v\mathbf{k}}(\mathbf{r}) \frac{2}{|\mathbf{r} - \mathbf{r}'|} \phi_{c'\mathbf{k}'}(\mathbf{r}') \phi^*_{v'\mathbf{k}'}(\mathbf{r}'). \end{aligned} \tag{1.7}$$

The first term on the RHS of Eq. (1.7) represents the screened Coulomb interaction between electrons and holes. The first second is the (unscreened) exchange interaction. The overall effect of the interaction kernel on the optical absorption spectrum is a redistribution of oscillator strength as well as the appearance of bound excitons within the band-gap.

1.2.3 Absorption spectrum of bulk hBN

Before we discuss the influence of e-e and e-h interaction onto the spectra of the tubes, we turn our attention to the absorption spectrum of bulk hBN for two reasons: (i) bulk hBN is the precursor material for the fabrication of BN nanotubes and spectroscopic methods should thus be able to distinguish tubes and bulk; (ii) for bulk hBN, sufficient experimental data exists to judge the validity of the combined approach of GW for the e-e interaction and the Bethe-Salpeter Equation for the e-h correlation (in the following abbreviated by GW+BS).

Results for the energy-dependent dielectric function of hBN (light polarization parallel to the layers) are shown in Fig. 1.6 a) and compared with the experimental data from electron-energy loss spectroscopy (EELS)[17] in panel b). The dash-dotted line shows the RPA absorption spectrum which is in agreement with earlier RPA calculations[18] [7] [15]. The broad peak with a maximum at 5.6 eV is entirely due to the continuum of inter-band transitions between the π and π^* bands (see Fig. 1.5). The calculated GW+BS absorption spectrum displays a double peak structure with the main peak at 5.7 eV and a second peak at 6.4 eV. The shape of the spectrum is entirely different from the RPA spectrum: the first peak is due to a strongly bound exciton [14], and the second peak contains contributions from higher excitons and from the onset of the continuum of inter-band transitions (see below). The similarity between the RPA and GW+BS spectra stems exclusively from the strong broadening employed in the calculation. The main peaks in the two spectra are at about the same position because of an almost-cancellation between the bandgap widening due to the GW-approximation and the red-shift of oscillator strength due to excitonic effects. Comparison with Fig. 1.6 b) shows that the shape of the GW+BS spectrum is in much better agreement with experiment than

---

[17] C. Tarrio and S.E. Schnatterly, Phys. Rev. B **40**, 7852 (1989).

[18] Y. N. Xu and W. Y. Ching, Phys. Rev. B **44**, 7787 (1991)

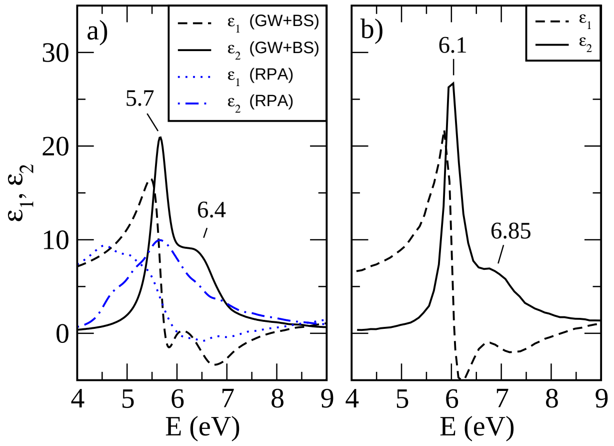

Figure 1.6: a) Real (ϵ_1) and imaginary (ϵ_2) parts of the dielectric function of hBN calculated in the GW+BSE approach and in RPA. b) Experimental data from EELS [17], where ϵ_1 and ϵ_2 are calculated from the loss function via a Kramers-Kronig transform. The calculations include a Lorentzian broadening of 0.2 eV (full-width at half-maximum) in order to mimick the estimated experimental broadening. The light-polarization is parallel to the BN layers.

the RPA spectrum. This underlines the importance of excitonic effects in hBN. The influence of excitonic effects becomes even more pronounced when we compare the real part of ϵ. Only the GW+BS calculation can reproduce qualitatively the shape of the experimental ϵ_1.

The excitonic nature of the absorption spectrum becomes clear if plotted with a very small broadening as in Fig. 1.7. The dominant first peak at 5.7 eV in the theoretical absorption spectrum is clearly a discrete bound exciton. Its huge binding energy of 0.7 eV was explained by Arnaud et al.[14] as due to the fact that the excitonic wave-function is mostly confined within one layer. In the pure 2D limit, the binding energy of a hydrogenic system is increased by a factor of four compared to the 3D case[19]. Even if the exciton confinement to one layer in bulk hBN is not perfect, it leads to a considerable enhancement of the exciton binding energy with respect to non-layered materials. In the inset c) of Fig. 1.7, we show an image of the excitonic wave-function [33]. Since only the relative position between electron and hole can be shown, we choose the position of the hole at a small distance above one of the nitrogen atoms. (The hole is localized there with a high likelihood, because the HOMO stems from a superposition of nitrogen p_z orbitals, as shown in Fig. 1.2). The wave-function plot thus represents the probability density to find the excited electron if the hole is at a given position. Clearly, the probability is enhanced around the boron atoms (the LUMO being a superposition of boron p_z orbitals). Furthermore, the probability density is confined to within a few atomic distances. According to the hydrogenic exciton model (Eqs. (1.4) and (1.5)), the strong confinement of the exciton is linked to a strong binding energy.

Not all excited states that are obtained with the Bethe-Salpeter equation are optically active. We indicate in Fig. 1.7 that about 90 meV below the dominant excitonic peak, there is a “dark” bound exciton. This exciton cannot be directly excited through absorption of a photon, but it may play a role in luminescence. Both the dark and the bright exciton are

---

[19] M. Shinada and S. Sugano, J. Phys. Soc. Jpn. **21**, 1936 (1966); T. G. Pedersen, Phys. Rev. B **67**, 073401 (2003).

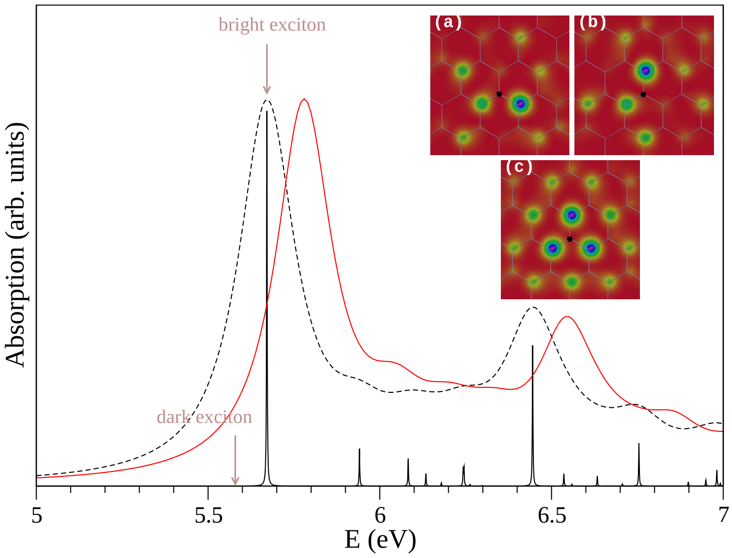

Figure 1.7: Optical absorption spectrum of hBN with a broadening of 0.001 eV (black solid line) and with an estimated experimental broadening of 0.1 eV calculated with `Yambo` (black dashed line) and with VASP (red solid line). Inset: Two dimensional projections of the probability density $|\Psi^{\lambda}(r_h, r_e)|^2$ of the degenerate exciton states with a) $\lambda = 3$ and b) $\lambda = 4$. The hole is located 0.4 a.u. above the nitrogen atom in the center (black circle). Summing the two densities (panel c) restores the three-fold rotation symmetry.

doubly degenerate states. The electron densities of each of the two states that contribute to the bright exciton are not rotationally symmetric Fig. 1.7 a) and b), but adding the densities of the two states, we recover the expected three-fold rotation symmetry Fig. 1.7 c). If the symmetry of the perfect crystal is broken, the degeneracy of the excitons is lifted and the dark exciton acquires some oscillator strength [33].

Fig. 1.7 shows calculations with two different GW+BS codes. Small differences in the absolute position of the spectra (of the order of 0.1 eV) stem probably from the different pseudopotentials which plays a role for the GW-correction to the band gap. The code `Yambo`[20] that was used for the black curve in Fig. 1.7 uses norm-conserving pseudopotentials, while `VASP`[21] (red curve in Fig. 1.7) uses the projector-augmented-wave (PAW) method[22]. Both spectra have in common that they are about 0.3 eV too low in comparison with the various experimental data[17] [23]. One reason for this (small) mismatch may be that the GW-approximation is only the first-order correction to the band gap. Higher-order corrections may enlarge the theoretical band-gap even further and thus blue-shift the spectrum. Another explanation is the effect of phonon-renormalization on the absorption spectrum. Theoretical calculations are usually performed at zero temperature. Only recently, the first ab-initio calculations of exci-

---

[20] A. Marini et al., the `Yambo` project, http://www.yambo-code.org/.

[21] G. Kresse and J. Furthmüller, Phys. Rev. B **54**, 11169 (1996); M. Shishkin and G. Kresse, Phys. Rev. B **74**, 035101 (2006).

[22] P.E Blöchl, Phys. Rev. B **50**, 17953 (1994).

[23] J. S. Lauret, R. Arenal, F. Ducastelle, A. Loiseau, M. Cau, B. Attal-Tretout, and E. Rosencher, Phys. Rev. Lett. **94**, 037405 (2005).

tonic effects including the exciton-phonon coupling were achieved[24]. This allowed to calculate absorption spectra at finite temperature. For bulk hBN at room temperature the dominant excitonic peak has been shown to be at 5.98 eV, in excellent agreement with the experimental data[17] [23].

1.2.4 Absorption spectrum of BN-tubes

After the discovery of carbon nanotubes in 1991, for several years, the optical spectra were only discussed in the independent-particle picture. In 1997, the presence of excitons in carbon tubes was predicted by Ando[25]. Since GW+BS calculations are quite expensive and since the unit-cell of nanotubes comprises more than 20 atoms, it was only in 2004 that the first ab-initio excitonic spectra of carbon tubes were published [26] [27] [28]. The excitonic nature of the spectra was confirmed in numerous experiments, e.g., Refs.[29] [30].

Since BNNTs have a much larger band-gap than semiconducting CNTs, it can be expected that excitonic effects are even more pronounced than in CNTs. This has been indeed confirmed by GW+BS calculations [21] [31]. Due to the lower dimensionality (and due to lower screening of the e-e interaction), both in the single-sheet and in isolated BN nanotubes, the GW-band gap correction (with respect to the DFT-LDA band structure) is strongly enhanced compared to bulk hBN: 3.6 eV for the single sheet [21] and 3.25 eV for the (8,0) tube[31] as compared to 1.8 eV for bulk hBN.

Fig. 1.8 shows the absorption spectrum of the BN (8,0) tube with and without e-h interaction (in both cases, GW-corrections to the band-gap are included). Without e-h interaction, the continuum of band-to-band transitions would start above 8 eV. A strong excitonic binding energy of 2.3 eV leads, however, to a first absorption peak at 5.72 eV. As in the case of bulk hBN, the first absorption peak comprises most of the oscillator strength of the entire absorption spectrum.

The wave-function of the 5.72 eV exciton is displayed in Fig. 1.9 (a)-(c) and compared to the wave-function of the lowest bright exciton in an (8,0) carbon nanotube (panels (d)-(f)). The hole is located above a chosen N (C) atom on one side of the tube. While the exciton in the carbon tube is delocalized around the whole tube circumference, the exciton in the BN tube is localized on the side where the hole is located. Also along the tube axis, the exciton in the BN tube is much more localized then the one in the carbon tube. This is in line with the much higher excitonic binding energy in BN tubes than in C tubes.

Fig. 2 of Ref. [21] (which is reprinted in the following), presents the excitonic absorption spectra for the same series of BN nanotubes as in Fig. 1.4. We compare with the spectra of the single sheet and of bulk hBN. With increasing diameter, the shape of the tube spectra converges rapidly towards the sheet spectrum which in turn is not very different from the

---

[24] A. Marini, Phys. Rev. Lett. **101**, 106405 (2008).

[25] T. Ando, J. Phys. Soc. Jpn. **66**, 1066 (1997).

[26] C.D. Spataru, S. Ismail-Beigi, L.X. Benedict, and S.G. Louie, Phys. Rev. Lett. **92**, 077402 (2004).

[27] C.D. Spataru, S. Ismail-Beigi, L.X. Benedict, and S.G. Louie, Appl. Phys. A **78**, 1129 (2004).

[28] E. Chang, G. Bussi, A. Ruini, and E. Molinari, Phys. Rev. Lett. **92**, 196401 (2004).

[29] F. Wang, G. Dukovic, L. E. Brus, and T. F. Heinz, Science **308**, 838 (2005).

[30] Y.-Z. Ma, S.L. Dexheimer, L. Valkunas, S.M. Bachilo, and G.R. Fleming, Phys. Rev. Lett. **94**, 157402 (2005); Y.-Z. Ma, L. Valkunas, S.M. Bachilo, and G.R. Fleming, J. Phys. Chem. B **109**, 15671 (2005).

[31] C.-H. Park, C.D. Spataru, S.G. Louie, Phys. Rev. Lett. **96**, 126105 (2006).

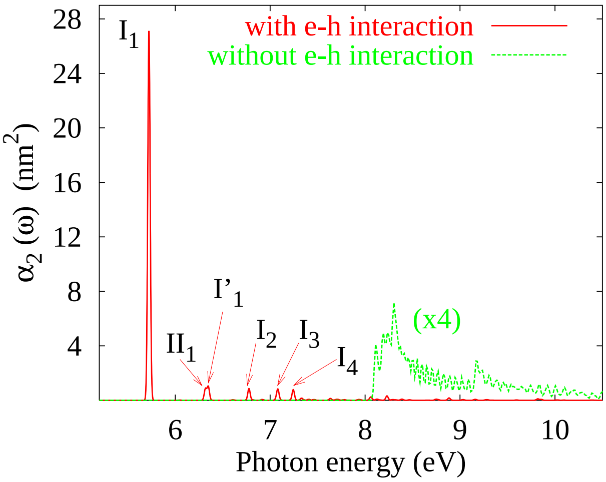

Figure 1.8: Absorption spectra of the (8,0) SWBNNTs. The imaginary part of the polarizability per unit of tube length, $\alpha_2(\omega)$, is given in unit of nm^2. The spectra are broadened with a Gaussian of 0.0125 eV. Figure reprinted from Ref. [31]

spectrum of the bulk. The rapid convergence as a function of tube diameter towards the sheet spectrum can be understood from Fig. 1.9. Since the exciton is not delocalized around the circumference but localized within a few nearest neighbors' distance, it "sees" a locally flat environment and behaves thus as an exciton in the flat sheet. We note that there is a chirality dependence of the optical spectra but it is only visible for the smallest diameter tubes. The spectra of the armchair tubes converge much faster to the 2D case than the ones of the zig-zag tubes.

Many-body effects in carbon nanotubes have been found to be quite different[26 28]: binding energies and quasiparticle shifts are much smaller, and the extension of the excitonic wave-function (several nm) is larger than the typical tube circumference. Thus, excitonic binding energies strongly vary with the diameter. Excitons in carbon nanotubes are one-dimensional objects, i.e. squeezed in the circumferential direction.

The strongly localized nature of the exciton in BN structures restricts the appearance of one-dimensional confinement effects to small diameter tubes, i.e, tubes for which the extension of the excitonic wavefunction is comparable to the nanotube circumference. As the experimental tubes have diameters around 1.4 nm, the 1D-nature of the tubes cannot be observed and only the 2D nature of the local exciton environment (tube surface) controls the optical activity.

We remark that dimensionality effects in the electronic properties of BN nanostructures would be more visible in other spectroscopic measurements such as photoemission spectroscopy, where we mainly map the quasiparticle spectra, and this (as the exciton binding itself) is sensitive to the change in screening going from the tube to the sheet to bulk hexagonal BN. In particular the *quasi-particle band-gap* will vary strongly with dimensionality (opening as dimensionality reduces). In the following, we present a reprint of our work on the excitonic effects of BN nanotubes [21].

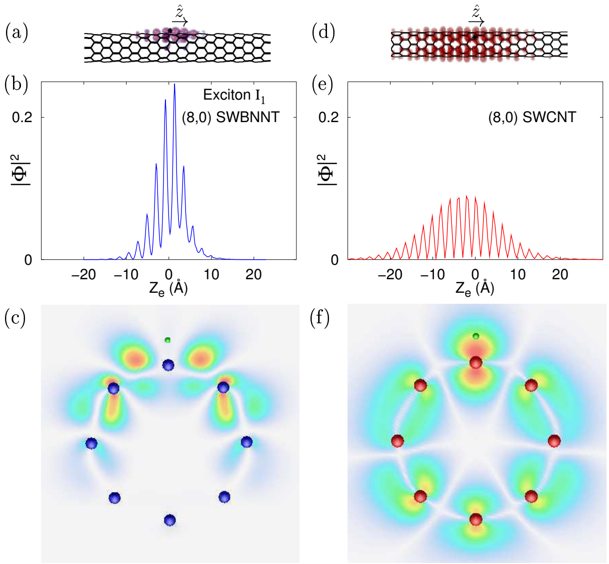

Figure 1.9: (a)-(c): Wavefunction of the lowest energy bright exciton of the (8,0) BNNT. (a) Isosurface plot of electron probability distribution $|\Phi(\mathbf{r}_e, \mathbf{r}_h)|^2$ with the hole fixed at the position indicated by black star. (b) $|\Phi(\mathbf{r}_e, \mathbf{r}_h)|^2$ along the tube axis, averaged over the tube cross section. The hole position is set at zero. (c) $|\Phi(\mathbf{r}_e, \mathbf{r}_h)|^2$ evaluated on a cross-sectional plane of the tube. (d)-(f): Wavefunction of the lowest energy bright exciton of the (8,0) SWCNT. Plotted quantities are similar to those in (a)-(c). Figure reprinted from Ref. [31]

PRL **96,** 126104 (2006) PHYSICAL REVIEW LETTERS week ending 31 MARCH 2006

Excitons in Boron Nitride Nanotubes: Dimensionality Effects

Ludger Wirtz,[1,2] Andrea Marini,[3,2] and Angel Rubio[4,5,6,2]

[1]*Institute for Electronics, Microelectronics, and Nanotechnology (IEMN), CNRS-UMR 8520, B.P. 60069, 59652 Villeneuve d'Ascq Cedex, France*
[2]*European Theoretical Spectroscopy Facility (ETSF), 20018 San Sebastián, Spain*
[3]*Istituto Nazionale per la Fisica della Materia e Dipartimento di Fisica dell'Universitá di Roma "Tor Vergata", Via della Ricerca Scientifica, I-00133 Roma, Italy*
[4]*Donostia International Physics Center (DIPC), 20018 Donostia-San Sebastián, Spain*
[5]*Department of Material Physics, UPV/EHU and Centro Mixto CSIC-UPV, 20018 San Sebastián, Spain*
[6]*Institut für Theoretische Physik, Freie Universität Berlin, Arnimallee 14, D-14195 Berlin, Germany*

(Received 29 August 2005; published 30 March 2006)

We show that the optical absorption spectra of boron nitride (BN) nanotubes are dominated by strongly bound excitons. Our first-principles calculations indicate that the binding energy for the first and dominant excitonic peak depends sensitively on the dimensionality of the system, varying from 0.7 eV in bulk hexagonal BN via 2.1 eV in the single sheet of BN to more than 3 eV in the hypothetical (2, 2) tube. The strongly localized nature of this exciton dictates the fast convergence of its binding energy with increasing tube diameter towards the sheet value. The absolute position of the first excitonic peak is almost independent of the tube radius and system dimensionality. This provides an explanation for the observed "optical gap" constancy for different tubes and bulk hexagonal BN.

DOI: 10.1103/PhysRevLett.96.126104 PACS numbers: 81.07.De, 61.46.−w, 71.35.−y

In complete analogy to carbon nanotubes, boron nitride (BN) nanotubes [1,2] can be thought of as cylinders that are obtained when a single sheet of hexagonal BN (hBN) is rolled onto itself. Since hexagonal BN is a large band-gap insulator [3], the band gap of BN tubes is similarly large, independent of their radius and chirality. The detailed knowledge of the optical properties of BN tubes is indispensable for their characterization and may help to guide their use as nanoelectronic devices. Example BN nanotubes have been used to build a field effect transistor [4]. Furthermore, experiments on ultraviolet luminescence [5] of bulk hexagonal BN suggest to explore the use of BN nanotubes as ultraviolet light sources. In this context, it is crucial to know about possible excitonic states whose importance has been recently shown for the optical spectra of carbon nanotubes [6,7]. For the wide band-gap BN tubes, we expect even stronger excitonic effects.

Very recently, two experimental studies of the optical properties of BN nanotubes have appeared in this journal which strongly contradict each other. Both studies compare their spectra to the one of bulk BN which has its first absorption peak at 6.1 eV and an onset of absorption at about 5.8 eV. Lauret *et al.* [8] have measured two additional peaks in the optical absorption spectra of BN tubes at 4.45 and 5.5 eV. The lower of these two peaks was interpreted as a due to a bound exciton. Arenal *et al.* [9], on the contrary, have measured the electron-energy loss spectra (EELS) of isolated BN tubes and obtained a constant "optical gap" of 5.8 eV for bulk BN and different single and multiwall tubes. For a proper interpretation of the spectra, one has to take into account that already the absorption peak of bulk hexagonal BN at 6.1 eV is due to a strongly bound Frenkel exciton [10,11]. The question to be asked is therefore: how does the binding energy of this exciton change as we compare the quasi-two-dimensional BN sheet and the quasi-1D BN nanotubes with the 3D bulk BN? Furthermore: up to which diameter do tubes exhibit one-dimensional excitonic effects? We show in this Letter that the excitonic binding energy increases strongly with lower dimensionality. At the same time, however, the quasiparticle gap strongly increases such that the absolute position of the first (excitonic) absorption peak remains almost constant in agreement with Ref. [9].

So far, the optical properties of BN nanotubes have only been calculated [12,13] on the level of the random-phase approximation (RPA), i.e., in the picture of independent-particle excitations. Here, we use the methods of many-body perturbation theory to include electron-electron and electron-hole effects [14]. Our calculations of the optical absorption spectra proceed in three steps. We first calculate the wave functions of the valence band states and a large number of conduction band states using density functional theory (DFT) in the local-density approximation (LDA) [15–17]. In the second step, we use the *GW* approximation [14,18] to calculate the quasiparticle energies ("true" single-particle excitation energies). In the third step, effects of electron-hole attraction (excitonic effects) are included by solving the Bethe-Salpeter (BS) equation [14].

Calculation details: we use a trigonal array of tubes with minimum interwall distance of 20 a.u. in order to minimize intertube interaction and to simulate as closely as possible the properties of isolated tubes. The tubes are geometry optimized (forces on the atoms less than 5×10^{-5} a.u.). In the *GW* calculation [19] we perform a "semiself consistent" (GW_0) calculation by updating the quasiparticle energies in G (but not in W) until the resulting quasiparticle energies are converged [20]. For the optical absorption spectra of (n, n) armchair tubes and $(n, 0)$ zigzag tubes with polarization along the tube axis, transitions between the highest $2n$ valence bands (the π bands) and the lowest $2n$ conduction bands (the π^* bands) are taken into account (the other transitions being dipole forbidden).

In Fig. 1, we investigate the influence of the supercell geometry on the excitonic binding energy and on the quasiparticle gap of the single sheet of hexagonal BN. The spectrum is dominated by the lowest bound exciton which collects most of the oscillator strength in the energy range between 0 and 8 eV [see Fig. 2(b)]. The excitonic binding energy is measured as the distance between this peak and the onset of the continuum which is given by the direct quasiparticle gap between the π and π^* bands. With increasing intersheet distance, approaching the limit of a quasi-2D isolated sheet, the excitonic binding energy increases and converges towards the value of 2.1 eV [as compared to the binding energy of 0.7 eV that is found for the 3D bulk hexagonal BN [11]]. This increase of the binding energy is due to two effects: (i) separating the layers, screening is reduced and becomes more anisotropic. In particular, for the perpendicular direction, it gets close to 1. The weaker screening leads thereby to an increase of the excitonic binding energy. (ii) An increased electron-hole overlap in the reduced dimensionality leads also to a stronger binding energy [in the purely 2D limit, the binding energy for a hydrogenic system is increased by a factor of 4 compared to the 3D case [21]]. At the same time, reduced dimensionality and reduced screening lead to an increased electron-electron correlation and thereby to an increase of the quasiparticle gap [22]. Figure 1 demonstrates that the increase of the quasiparticle gap almost exactly cancels the increase of the binding energy. *The position of the first absorption peak remains almost constant*. What changes is the onset of the continuum. For the BN sheet, however, the absorption at the onset of the continuum is almost zero (also the higher excitonic peaks carry very low oscillator strength). The excitonic spectrum can therefore be calculated to a good approximation already with an intersheet distance of 20 a.u. We made a similar series of calculations for the hypothetical BN(2, 2) tube which has a diameter of 2.8 Å and is close to being a 1D system. Again, as we increase the intertube distance, the increase of the quasiparticle gap almost cancels the increase of the excitonic binding energy. While the latter converges towards a value higher than 3 eV, the absolute position of the first absorption peak remains constant to within 0.2 eV. In the following, we present therefore calculations for different tubes in a supercell geometry with 20 Å interwall distance. We remark that dimensionality effects would be more visible in other spectroscopic measurements such as photoemission spectroscopy, where we mainly map the quasiparticle spectra, and this (as the exciton binding itself) is sensitive to the change in screening going from the tube to the sheet to bulk hexagonal BN. In particular, the *quasiparticle band gap* will vary strongly with dimensionality (opening as dimensionality reduces).

In Fig. 2 we present the spectra of bulk hexagonal BN, of the single sheet of hexagonal BN, and of different BN nanotubes with diameters ranging from 2.8 Å (for the purely hypothetical BN(2, 2) tube) to 9.7 Å (for the BN(7, 7) tube) which is at the lower border of the range of experimentally produced tubes. The light polarization is set parallel to the planes or tube axis, respectively. On the left-hand side, we show the RPA spectra which are almost

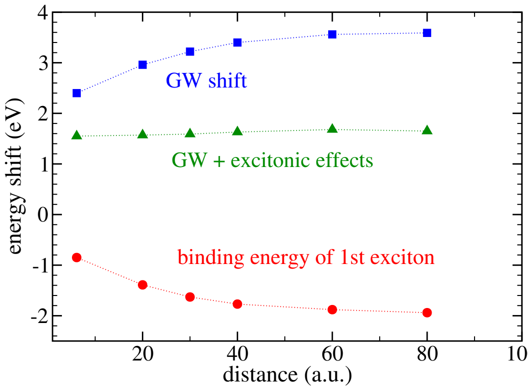

FIG. 1 (color online). Single sheet of hexagonal BN: dependence of the excitonic binding energy and the quasiparticle gap on the intersheet distance in a supercell geometry.

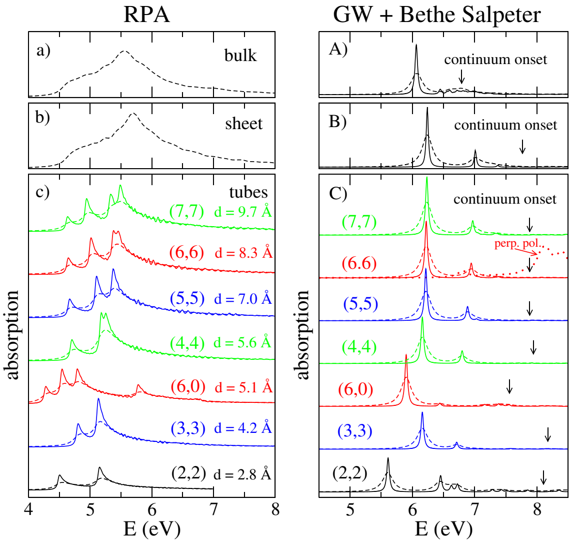

FIG. 2 (color online). Optical absorption of (a) hexagonal BN, (b) BN sheet, and (c) six different BN tubes with increasing diameter d. We compare the results of the GW + Bethe-Salpeter approach (right-hand side) with the random-phase approximation (left-hand side). Solid lines are calculated with a Lorentzian broadening of 0.025 eV, dashed lines with a broadening of 0.1 eV (for comparison with experimental data). The light polarization is parallel to the plane/tube axis, respectively [except for the dotted line in the (6, 6) case where the light polarization is perpendicular to the tube axis; see main text for discussion].

indistinguishable for the bulk and for the single sheet. The selection rules only allow transitions between the π and π^* bands (band 4 and 5 in the sheet). The band structure of the tubes can be constructed via the zone-folding procedure, i.e., by cutting the 2D band structure of the sheet along certain discrete lines that correspond to quantized wave vector along the circumferential direction. The RPA spectra of the tubes display therefore transitions at the same energies as in the sheet. [For a comparison of tube and sheet band-structures, see Refs. [1,3,13].] With increasing diameter, the shape of the tube spectra converges rapidly towards the sheet spectrum, in particular, if plotted with a Lorentzian broadening of 0.1 eV (corresponding roughly to usual experimental values). A calculation with a fine broadening of 0.025 eV (and a correspondingly fine sampling with 200 **k** points in the first Brillouin zone) reveals additional fine structure below 5.5 eV. This structure is due to the van Hove singularities in the one-dimensional density of states. For tubes with larger radii, the density of the fine-structure peaks increases and the RPA spectrum approaches that of the 2D sheet. The onset of absorption is constantly at 4.7 ± 0.1 eV for all tubes except for the $(2, 2)$ and the $(6, 0)$ tube (and other small diameter zigzag tubes) where the gap is lowered due to curvature effects [1].

While the RPA spectra are due to a continuum of interband transitions, the BS + GW optical spectra on the right-hand side of Fig. 2 are dominated by discrete excitonic peaks where the first peak comprises most of the oscillator strength. For bulk hexagonal BN, we have shown [11] that the broadened excitonic spectrum properly reproduces the experimental spectral shape [23]. The sheet spectrum contains three bound excitonic peaks of rapidly decreasing intensity and absorption at the onset of the continuum is reduced to almost zero. As explained above, the stronger binding energy of the first bound exciton is almost compensated by an increase of the quasiparticle gap due to the reduced dimensionality. The same holds for the tube spectra: except for the three smallest tubes, the position of the first and dominant excitonic peak remains constant. With increasing tube diameter, the spectrum rapidly converges towards the three-peak spectrum of the flat sheet. Also, the onset of the continuum converges towards the value in the sheet (note that we compare here the values for a supercell geometry with intersheet or intertube distance of 20 a.u.). The rapid convergence of the excitonic peaks is an indication for a strong confinement of the exciton wave function. Plotting the wave function, we have verified that this Frenkel type exciton is confined to within a few interatomic distances for either tubes, sheet or bulk hexagonal BN [see also the plot for an exciton in bulk hexagonal BN in Ref. [10]]. With increasing tube diameter, the excitons only "see" a *locally flat environment* which explains the rapid convergence towards the sheet spectrum. The strongly localized nature of the exciton in BN structures makes the appearance of one-dimensional confinement effects very restricted to small diameter tubes, i.e., tubes for which the extension of the excitonic wave function is comparable to the nanotube circumference. As the experimental tubes have diameters around 1.4 nm, the 1D nature of the tubes cannot be observed and only the 2D nature of the local exciton environment (tube surface) controls the optical activity. Many-body effects in carbon nanotubes have been found to be quite different [6,7]: binding energies and quasiparticle shifts are much smaller, and the extension of the excitonic wave function (several nm) is larger than the typical tube circumference. Thus, excitonic binding energies strongly vary with the diameter. Contrary to the case of BN tubes, where we quickly reach the two-dimensional limit of the flat sheet, excitons in carbon nanotubes remain one-dimensional objects, i.e., squeezed in the circumferential direction.

For the $(6, 6)$ tube, we display in Fig. 2(c) also the spectrum for light polarization perpendicular to the tube axis. The spectrum exhibits a major excitonic peak that lies slightly below the second excitonic peak obtained for light polarized along the tube axis. Note that the sheet is completely transparent up to 9 eV for light polarized perpendicular to the plane.

We compare our results now to two recent contradictory measurements of the optical properties of BN nanotubes [8,9]: in the EELS experiment of Arenal *et al.* [9], the electron beam passes the tube in the tangential direction. A quantitative explanation of the spectral shape would require the calculation of the imaginary part of the polarizability $\alpha_{m,k}$, where m is the index for the multipole expansion in circumferential direction and k is the wave vector of the Fourier expansion along the tube axis [24]. However, the dipolar contribution ($m = 0$) in the limit $k \longrightarrow 0$, calculated in this Letter, is the dominant part in the expansion of α. The constancy of the first excitonic peak in Fig. 2 explains why the "optical gap" observed in Fig. 2 of Ref. [9] is always 5.8 eV, independently if they measure multiwall tubes, or single-wall tubes of different diameters. The shoulder on the right-hand side of the main peak in Fig. 2c of Ref. [9] is the effect of the 2nd excitonic peak. Figure 2 demonstrates that the second (and less intense) excitonic peak starts to form a shoulder of the first peak as we plot the spectra with a stronger broadening. Our calculations also reproduce the finding of Ref. [9] that the dominant peak is higher in energy for the tubes [their Figs. 2(a)–(c)] than for bulk BN [their Fig. 2(d)] [25].

We note that there is a chirality dependence of the optical spectra but it is only visible for the smallest diameter tubes. The spectra of the armchair tubes converge much faster to the 2D case than the ones of the zigzag tubes. However, as experimental tube diameters [9] are much larger than the 5.1 Å of the $(6, 0)$ zigzag tube that is presented in this Letter, we expect the chiral dependence to be marginal. [Results similar to the $(6, 0)$ tube are presented in Ref. [26] for the $(8, 0)$ tube]. Our calculations show that the explanation of Ref. [8] for the two peaks at 4.45 and 5.5 eV in their absorption spectra of a sample containing BN tubes does not hold: the peaks are neither due to additional van Hove singularities (since the spectra are entirely dominated by discrete excitonic peaks) nor can they be explained by an increased excitonic binding energy (which is canceled by an increased quasiparticle gap).

So far, we have concentrated on singlet active excitons. For bulk hexagonal BN [11], we have shown previously that there is a dark singlet exciton and two triplet excitons below the first optically active exciton. For the single sheet (and light polarization parallel to the plane), we find that the lowest optically active exciton is doubly degenerate. There is no dark singlet exciton below, but a doubly degenerate triplet exciton at 0.1 eV lower energy. For the (6, 6) tube (and light polarization parallel to the tube axis), we find that the degeneracy of the singlet exciton is lifted, leading to a dark singlet exciton slightly (0.01 eV) below the optically active singlet exciton. The degeneracy of the triplet exciton is lifted as well: the two triplet excitons are 0.1 eV and 0.08 eV lower in energy than the optically active singlet exciton. Similar results hold for the (5, 5) and the (7, 7) tubes. A recent study for C tubes [27] has shown that the room temperature luminescence is enhanced once the complete series of active and dark excitons is taken into account. This would hold also in the present case. Furthermore, due to the minor differences in the optical spectra of tubes and bulk BN we expect the BN tubes to exhibit a strong ultraviolet lasing behavior as already observed for bulk BN [5]. The fact that this luminescence response would be rather insensitive to tube diameter and chirality makes the BN tubes ideal candidates for optical devices in the UV regime as the carbon nanotubes are in the infrared regime [28]. The photoluminescence quantum yield of BN tubes should surpass the efficiency of carbon [5].

We acknowledge helpful discussions with D. Varsano, V. Olevano, and L. Reining. The work was supported by the EU network of excellence NANOQUANTA (NMP4-CT-2004-500198) and the French GDR "nanotubes." Calculations were performed at IDRIS (Project No. 51827) and CEPBA. A. R. acknowledges the Humboldt Foundation.

---

[1] A. Rubio, J. L. Corkill, and M. L. Cohen, Phys. Rev. B **49**, R5081 (1994); X. Blase, A. Rubio, S. G. Louie, and M. L. Cohen, Europhys. Lett. **28**, 335 (1994).
[2] N. G. Chopra *et al.*, Science **269**, 966 (1995).
[3] X. Blase, A. Rubio, S. G. Louie, and M. L. Cohen, Phys. Rev. B **51**, 6868 (1995).
[4] M. Radosavljević *et al.*, Appl. Phys. Lett. **82**, 4131 (2003).
[5] K. Watanabe, T. Taniguchi, and H. Kanda, Nat. Mater. **3**, 404 (2004).
[6] C. D. Spataru, S. Ismail-Beigi, L. X. Benedict, and S. G. Louie, Phys. Rev. Lett. **92**, 077402 (2004); Appl. Phys. A **78**, 1129 (2004).
[7] E. Chang, G. Bussi, A. Ruini, and E. Molinari, Phys. Rev. Lett. **92**, 196401 (2004).
[8] J. S. Lauret *et al.*, Phys. Rev. Lett. **94**, 037405 (2005).
[9] R. Arenal, O. Stéphan, M. Kociak, D. Taverna, A. Loiseau, and C. Colliex, Phys. Rev. Lett. **95**, 127601 (2005).
[10] B. Arnaud, S. Lebègue, P. Rabiller, and M. Alouani, Phys. Rev. Lett. **96**, 026402 (2006).
[11] L. Wirtz, A. Marini, M. Grüning, and A. Rubio (to be published); cond-mat/0508421.
[12] A. G. Marinopoulos, L. Wirtz, A. Marini, V. Olevano, A. Rubio, and L. Reining, Appl. Phys. A **78**, 1157 (2004).
[13] G. Y. Guo and J. C. Lin, Phys. Rev. B **71**, 165402 (2005).
[14] For a recent review see, e.g., G. Onida, L. Reining, and A. Rubio, Rev. Mod. Phys. **74**, 601 (2002).
[15] W. Kohn and L. J. Sham, Phys. Rev. **140**, A1133 (1965).
[16] We use the code ABINIT: X. Gonze *et al.*, Comput. Mater. Sci. **25**, 478 (2002).
[17] We used Trouiller-Martins pseudopotentials in the Kleinman-Bylander form with cutoff radius of 1.59 a.u. for B and 1.50 a.u. for N. An energy cutoff of 25 hartree is used in the plane-wave expansion of the wave functions.
[18] M. S. Hybertsen and S. G. Louie, Phys. Rev. B **34**, 5390 (1986).
[19] We use the computer code SELF, http://www.fisica.uniroma2.it/~self/, written by A. Marini.
[20] This procedure yields a quasiparticle band gap for the single sheet and for the tubes that is about 0.25 eV higher than the one obtained on the nonself consistent (G_0W_0) level. Still, for bulk hexagonal BN we have shown [11] that this GW_0 calculation starting from LDA wave functions yields a quasiparticle band gap that is too low by 0.65 eV. In the present work, we assume that the same underestimation of the LDA GW_0 band gap holds also for the single sheet and for the tubes. Consequently, we add a 0.65 eV "scissor" shift to the calculated GW_0 band structure. The assumption that this shift is constant for bulk, sheet, and tubes is certainly only a zero order approximation. Closer comparison with the measured "optical gap" data of BN tubes in Fig. 2 of Ref. [9] indicates that this shift could be up to 0.35 eV higher for the tubes than for the bulk.
[21] M. Shinada and S. Sugano, J. Phys. Soc. Jpn. **21**, 1936 (1966); T. G. Pedersen, Phys. Rev. B **67**, 073401 (2003).
[22] C. Delerue, G. Allan, and M. Lannoo, Phys. Rev. Lett. **90**, 076803 (2003).
[23] C. Tarrio and S. E. Schnatterly, Phys. Rev. B **40**, 7852 (1989).
[24] D. Taverna, M. Kociak, V. Charbois, and L. Henrard, Phys. Rev. B **66**, 235419 (2002).
[25] This energy shift is 0.55 eV in Ref. [9] while we obtain in Fig. 2 a shift of 0.2 eV. This indicates that the underestimation of the band gap by the *GW* approximation is indeed slightly higher for the tubes than for bulk BN [see Ref. [20]].
[26] C.-H. Park, C. D. Spataru, and S. G. Louie, this issue, Phys. Rev. Lett. **96**, 126105 (2006).
[27] C. D. Spataru, S. Ismael-Beiji, R. B. Capaz, and S. G. Louie, Phys. Rev. Lett. **95**, 247402 (2005).
[28] J. A. Misewich, R. Martel, Ph. Avouris, J. C. Tsang, S. Heinze, and J. Tersoff, Science **300**, 783 (2003).

1.3 Luminescence spectroscopy

Recently, the observed high luminescence yield in bulk hBN crystals[5] [32] has raised the interest in BN compounds as potential candidates for UV light-emitting materials. The main luminescence peak (for very pure hBN crystals) was measured at 215 nm (5.77 eV) [5]. It is ascribed to the radiative decay of the lowest lying exciton. In the electronic structure community, this exciton is called a "bound exciton" because it corresponds to an electron that is "bound" to a hole in the valence band. Thus the energy of this state lies below the range of "free" conduction band electrons (see the discussion on optical absorption above). In contrast, the luminescence spectroscopy community tends to call this exciton a "free exciton" because it is independent of structural defects of the material. For the remainder of this section, we we will use the notation of the luminescence spectroscopy.

In comparison to the main absorption peak which is located between 6 and 6.1 eV[17] [23], the luminescence peak experiences a strong Stokes shift towards lower energy. We note, however, that recent photo luminescence excitation (PLE) spectra (i.e., measuring the luminescence intensity as a function of the exciting laser energy) locate the absorption peak corresponding to the "free" exciton rather at 5.81 eV[33]. This yields only a very small Stokes shift of the luminescence peak (5.77 eV).

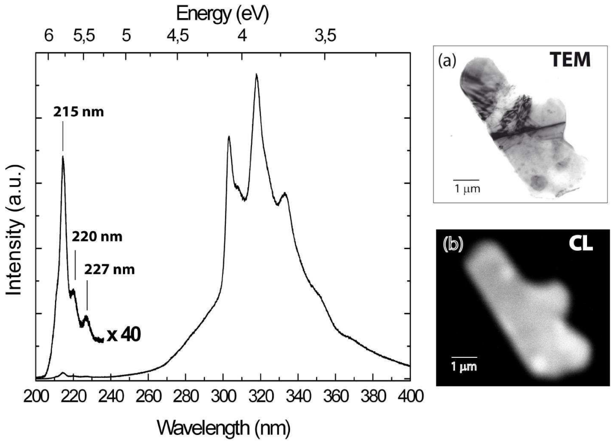

Figure 1.10: Cathodoluminescence spectrom of hBN crystallite at T=100K. (a) TEM image of the hBN crystallite and (b) polychromatic CL image. Figure reprinted from Ref. [34].

At low temperature $(< 100K)$, additional luminescence peaks at 220 nm (5.64 eV) and 227 nm (5.46 eV) have been observed[5] [34] (see Fig. 1.10). Jaffrennou et al. found that luminescence at the latter two wave-lengths occurs at the grain boundaries and around dislocations. They ascribed the two peaks to excitons that are bound to structural defects and thus have a higher binding energy than the free exciton (and thus a lower position in the luminescence spectrum). At very low temperature (8 K), Museur and Kanaev[33] found an additional "bound" exciton line at 5.56 eV and a line at 5.3 eV that they ascribed to a transition between filled acceptor

---

[32] Y. Kubota, K. Watanabe, O. Tsuda, and T. Taniguchi, Science **317**, 932 (2007).

[33] L. Museur and A. Kanaev, J. Appl. Phys. **103**, 103520 (2008).

[34] P. Jaffrennou, J. Barjon, J.-S. Lauret, B. Attal-Trétout, F. Ducastelle, and A. Loiseau, J. Appl. Phys. **102**, 116102 (2007).

and donor states.

Luminescence peaks in hBN have also been observed in the energy region of 4 eV[35] [36] [37] [33] (see Fig. 1.10). They have a much lower intensity than the high energy peaks and are explained by the presence of deep level impurities, probably due to Carbon or Oxygen atoms. Indeed, when hBN crystals were grown under ultra-clean conditions, the 4 eV energy band disappeared from the luminescence spectra.[38] The main peak displays several phonon replica on the low energy side. The proof that those peaks are really due to electron-phonon coupling was given by Han et al.[37] who showed that the splitting between the peaks, i.e., the vibrational frequency, changes as a function of the Boron isotope. The nature of the deep level impurity is not clear. However, calculations indicate the stability of Oxygen in substitution for Nitrogen atoms[37]. Vacancies and other impurities as C, could give rise to deep levels as well. The assignment of all the defect related peaks observed in luminescence requires more detailed theoretical work. However, it seems that all luminescence features observed below the main absorption peak are defect-mediated excitations, i.e., excitons bound to structural defects or transitions from/to acceptor/donor levels.

Luminescence on multi-walled BNNT samples was observed by several groups. Wu et al.[39] performed photoluminescence (PL) on multi-wall BN tubes. They only detected the deep-level impurity peaks around 4 eV. The zero-phonon line at 4.02 eV was falsely ascribed to the direct band gap. Other groups also detected the excitonic bands in the luminescence of multi-walled BNNTs[40] [41] [42] [37]. Bound excitonic peaks were observed at 5.49 and 5.34 eV [42], i.e., at somewhat lower energy than in bulk hBN (5.77 eV). This difference was tentatively explained in Refs.[41] [42]: trapping of excitons on crystalline defects appears to be a major phenomenon. In the tubes, dislocations and stacking faults along the walls may lead to a stronger trapping of excitons than in hBN and to an absence of the "free-exciton line" at 5.77 eV. The stronger trapping leads to slight red-shift of the bound excitonic lines with respect to the corresponding lines in the PL spectra of bulk hBN.

From this discussion it is a logical next step trying to build lasing or opto-electronic devices with BN nanotubes. In this respect, it is interesting to know if the optical properties can be tuned in a controlled way. It has been shown theoretically[43] [27] that the band gap of BNNTs can be reduced by applying an electric field perpendicular to the tube axis. This decrease of the gap is due to the Stark-effect, i.e., the charge densities of the top of the valence band

---

[35] C.A. Taylor II, S. W. Brown, V. Subramaniam, S. Kidner, S.C. Rand, and R. Clark, Appl. Phys. Lett. **65**, 1251 (1994).

[36] M.G. Silly, P. Jaffrennou, J. Barjon, J.-S. Lauret, F. Ducastelle, A. Loiseau, E. Obraztsova, B. Attal-Tretout, and E. Rosencher, Phys. Rev. B **75**, 085205 (2007).

[37] W.-Q. Han, H.-G. Yu, C. Zhi, J. Wang, Z. Liu, T. Sekiguchi, and Y. Bando, Nano Lett. **8**, 491 (2008).

[38] T. Taniguchi and K. Watanabe, J. Cryst. Growth **303**, 525 (2007).

[39] J. Wu, W.-Q. Han, W. Walukiewicz, J.W. Ager III, W. Shan, E.E. Haller, A. Zettl, Nano Letters **4**, (4) 647 (2004).

[40] P. Jaffrennou, F. Donatini, J. Barjon, J.-S. Lauret, A. Maguer, B. Attal-Tretout, F. Ducastelle, and A. Loiseau, Chem. Phys. Lett. **442**, 372 (2007).

[41] P. Jaffrennou, J. Barjon, J.-S. Lauret, A. Maguer, D. Goldberg, B. Attal-Trétout, F. Ducastelle, and A. Loiseau, phys. stat. sol. (b) **244**, 4147 (2007).

[42] P. Jaffrennou, J. Barjon, T. Schmid, L. Museur, A. Kanaev, J.-S. Lauret, C. Y. Zhi, C. Tang, Y. Bando, D. Goldberg, B. Attal-Trétout, F. Ducastelle, and A. Loiseau, Phys. Rev. B **77**, 235422 (2008).

[43] K.H. Koo, M.S.C. Mazzoni, and S.G. Louie, Phys. Rev. B **69**, 201401(R) (2004); C.-W. Chen, M.-H. Lee, and S.J. Clark, Nanotechnology **15**, 1837 (2004).

and bottom of the conduction band become spatially separated on opposite sides of the tube. Even though the gap is reduced considerably, the effect of an electric field on the optical absorption spectrum was found to be less pronounced [27] (for light polarization parallel to the tube axis which gives the dominant contribution to the averaged light-scattering cross Section). This situation may, however, change for luminescence spectra. Peaks around 4 eV in the luminescence spectra are related to defect levels (possible candidates discussed above are vacancies, oxygen or carbon substitutions). As an example, we have calculated the influence of the electric field on the acceptor level that is due to the replacement of a nitrogen atom by a carbon atom. (The calculations have been performed in a large supercell.) In Fig. 1.11 we show the density of states of the pure (9,9) BNNT, calculated within DFT-LDA. Adding the carbon impurity in panel b) introduces an impurity level at about 0.5 eV above the valence band edge. Depending on the orientation of the carbon impurity with respect to the direction of the electric field, this impurity level can move up or down with respect to the valence and conduction band edges (Fig.. 1.11 c and d). Photoluminescence may involve transitions from the conduction band to the impurity level and from the impurity level to the valence band. Defect mediated luminescence spectra may thus be more sensitive to the influence of an electric field than the spectra of pure BNNTs [27].

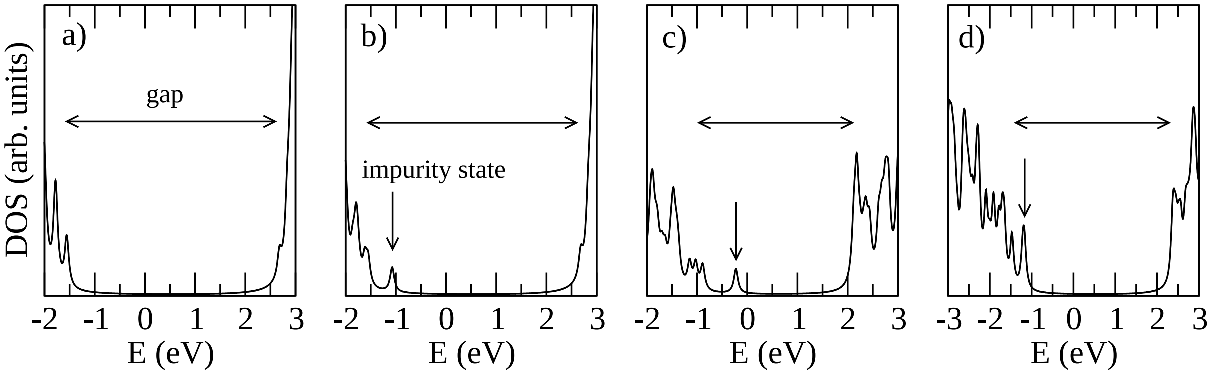

Figure 1.11: Density of states of a) a pure (9,9) BN nanotube, b) a tube with a Carbon impurity atom, c) with a C atom and a perpendicular E-field of 0.2 V/Å, d) with a C atom on the opposite side and an E-field of 0.2 V/Å. The light-polarization is parallel to the tube axis.

1.4 Plasmons and electron-energy loss spectroscopy

The loss function is calculated as the imaginary part of the inverse dielectric function, i.e., Im$\{-1/\epsilon(\omega,q)\}$. The loss function of bulk hBN with wave-vector q parallel to the layers has been measured with electron-energy loss spectroscopy (EELS) by Tarrio and Schnatterly [17]. The spectrum for $q \rightarrow 0$ displays two peaks, the so-called "π plasmon" at 8.7 eV and the "$\pi+\sigma$ plasmon" at 26.5 eV (this curve is also reproduced in Fig. 1.12 e). The names indicate that the latter plasmon represents the collective excitation mode of all the valence electrons in hBN while the first one is a collective oscillation of the π electrons alone. The loss function of bulk hBN is quite well reproduced if $\epsilon(\omega,q)$ is calculated on the level of the random-phase approximation (RPA) [15].

The measured loss-function of bundled multi-wall BNNTs in the limit $q \rightarrow 0$ displays the same two plasmonic peaks as bulk hBN, however red-shifted by 0.6 eV[44]. The similarity of the two spectra is expected, since the inner-radius of the multi-wall tubes was quite large (3.1 nm). The origin of the 0.6 eV shift, was tentatively assigned [44] to the curvature of the inner tubes. Indeed, calculations for small diameter BN tubes have demonstrated a downshift of the "π" plasmon [15]. Fuentes et al. also presented data on the q dispersion of the π plasmon which is similar to the dispersion in bulk hBN.

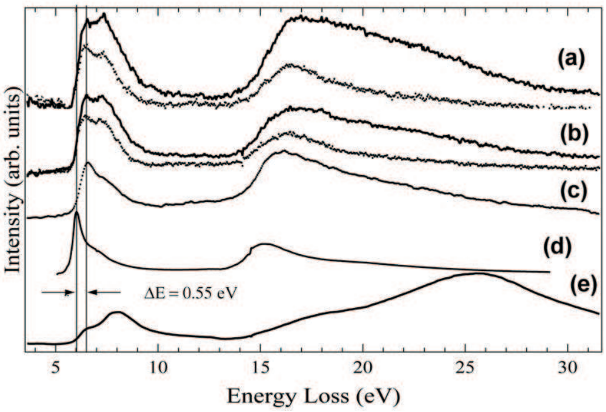

Figure 1.12: Experimental deconvoluted EELS for: (a) a triple-wall nanotube, electrons passing inside the tube and at grazing incidence, (b) a double-wall nanotube, electrons passing inside the tube and at grazing incidence, (c) a single-wall tube, (d) $\epsilon_{\|}$, extracted from the bulk loss spectrum in (e). Figure reprinted from Ref.[45].

The experiments of Fuentes et al. were performed on "bulk-like" samples of tubes. This allowed for a momentum (q) resolution of the loss spectra. The opposite limit was reached in spatially resolved EELS measurements on *isolated* BN tubes[45]. For isolated tubes, the "dielectric constant" ϵ (which is a bulk quantity) looses its meaning. Indeed, when a fast electron beam passes (near or through) a nanotube, the EELS spectrum is proportional to a weighted sum of multipolar polarizabilities $\alpha_m(q)$ with weights decreasing rapidly as a function of the azimuthal momentum m[46]. To a good approximation, the EELS spectra of isolated BN nanotubes are proportional to Im$(\alpha_0(q \rightarrow 0))$, i.e., to the optical polarizability. In the "continuum dielectric theory"[47],

$$\alpha_0(\omega) \propto \mathrm{Im}\left\{-\frac{1}{\epsilon_{\perp}(\omega, q \rightarrow 0)} + \epsilon_{\|}(\omega, q \rightarrow 0)\right\}, \tag{1.8}$$

where $\epsilon_{\perp}$ and $\epsilon(\|))$ are, respectively, the components of the dielectric tensor perpendicular and parallel to the layers. Since $\epsilon_{\perp}$ is strongly reduced through depolarization effects, the main contribution to the spatially resolved EELS of isolated BN tubes is thus given by Im$\{\epsilon_{\|}(\omega, q \rightarrow$

---

[44] G. G. Fuentes, E. Borowiak-Palen, T. Pichler, X. Liu, A. Graff, G. Behr, R. J. Kalenczuk, M. Knupfer, and J. Fink, Phys. Rev. B **67**, 035429 (2003).

[45] R. Arenal, O. Stéphan, M. Kociak, D. Taverna, A. Loiseau, and C. Colliex, Phys. Rev. Lett. **95**, 127601 (2005).

[46] D.Taverna, M. Kociak, V. Charbois, and L. Henrard, Phys. Rev. B **66**, 235419 (2002).

[47] L. Henrard and P. Lambin, J. Phys. B **29**, 5127 (1996).

$0)\}$. Therefore one can access the direct optical gap in EELS experiments, in contrast to bulk materials where one needs to perform a Kramers-Kronig analysis of the experimental data to extract the dielectric constant.

Indeed, the EELS data (see Fig. 1.12) displays a lot of similarity with the measured $\epsilon_{\|}(\omega)$ from optical absorption. Most importantly, the "optical gap" was shown to remain almost constant as a function of tube diameter and as a function of the number of tube walls [45]. Furthermore, it was measured to be almost the same as in bulk hBN. This behavior can be understood from the calculations of $\epsilon_{\|}(\omega)$ (Fig. 2 of Ref. [21]). While the quasi-particle band-gap of the tubes is strongly increased with respect to bulk hBN, the optical gap displays only minor changes. This is because the increased binding energy of the dominant excitonic peaks almost cancels the increase in the quasi-particle gap as one passes from bulk BN via the 2D single sheet to the 1D tubes.

1.5 Phonons and vibrational spectroscopy

Raman and infrared (IR) spectroscopy in which phonons are excited by inelastic scattering of light or light absorption, respectively, are convenient tools to investigate the composition of macroscopic samples of nanotubes. Carbon nanotubes have been investigated extensively through vibrational spectroscopy. Early Raman[48] and infrared[49] investigations were performed on samples of multi-wall carbon nanotubes (MWNT's) and showed signatures close to those of graphite. However, after the production of single-wall nanotubes (SWNT's) in large quantities, resonant Raman spectroscopy turned into a very precise, highly diameter selective identification tool [50]. Especially the low frequency Raman modes such as the radial breathing mode (RBM) strongly depend on the tube diameter and facilitate thus the characterization of tubes. The high frequency modes are only weakly diameter dependent, but their intensity in the resonant Raman spectra strongly depends on the diameter through the electronic excitation energy[51]. IR spectroscopy on single-wall carbon nanotubes[52] shows only small differences when compared to IR data of graphite.

For BN nanotubes, the situation is quite different: The Raman intensities in the visible light frequencies are weaker than for C nanotubes, since the Raman scattering (for lasers in the visible light regime) is non-resonant due to the wide band gap. On the other hand, BN nanotubes are a polar material and show a much higher IR absorbance than C-nanotubes [53]. It is expected, that the combination of Raman and IR spectroscopy will develop into a standard characterization tool for BN-tubes such as it is already in the case of C-tubes. At this stage

---

[48] P. C. Eklund, J. M. Holden, R. A. Jishi, Carbon **33**, 959 (1995).

[49] J. Kastner, T. Pichler, H. Kuzmany, S. Curran, W. Blau, D. N. Weldon, M. Delamesiere, S. Draper, and H. Zandbergen, Chem. Phys. Lett. **221**, 53 (1994).

[50] A. M. Rao, E. Richter, S. Bandow, B. Chase, P. C. Eklund, K. A. Williams, S. Fang, K. R. Subbaswamy, M. Menon, A. Thess, R. E. Smalley, G. Dresselhaus, and M. S. Dresselhaus, Science **275**, 187 (1997).

[51] R. Saito, T. Takeya, T. Kimura, G. Dresselhaus, and M. S. Dresselhaus, Phys. Rev. B **57**, 4145 (1998).

[52] U. Kuhlmann, H. Jontoljak, N. Pfänder, P. Bernier, C. Journet, and C. Thomsen, Chem. Phys. Lett. **294**, 237 (1998).

[53] E. Borowiak-Palen, T. Pichler, G. G. Fuentes, B. Bendjemil, X. Liu, A. Graff, G. Behr, R. J. Kalenczuk, M. Knupfer, and J. Fink, Chem. Comm. 82 (2003).

it is very important to have a detailed knowledge of phonon frequencies in BN-nanotubes and to understand the dependence on diameter and chirality, in order to guide future experiments. We will give in the following a short description on how phonons are calculated. The phonons of bulk hBN and BN nanotubes are presented and Raman and IR active modes are analyzed. We present the calculation of non-resonant Raman intensities and give an overview on the experimental results as compared to the theoretical predictions.

1.5.1 Phonon calculations

The phonons are obtained from the change in total energy as the atoms are displaced from their equilibrium position. Mathematically, the phonon frequencies ω as a function of the phonon wave-vector $\mathbf{q}$ are obtained as the solution of the secular equation

$$\det\left|\frac{1}{\sqrt{M_s M_t}} C_{st}^{\alpha\beta}(\mathbf{q}) - \omega^2(\mathbf{q})\right| = 0. \tag{1.9}$$

M_s and M_t denote the atomic masses of atoms s and t and the dynamical matrix is defined as

$$C_{st}^{\alpha\beta}(\mathbf{q}) = \frac{\partial^2 E}{\partial u_s^{*\alpha}(\mathbf{q}) \partial u_t^{\beta}(\mathbf{q})}, \tag{1.10}$$

where u_s^{α} denotes the displacement of atom s in direction α. The second derivative of the energy in Eq. (1.10) corresponds to the change of the force acting on atom t in direction β with respect to a displacement of atom s in direction α:

$$C_{st}^{\alpha\beta}(\mathbf{q}) = \frac{\partial}{\partial u_s^{*\alpha}(\mathbf{q})} F_t^{\beta}(\mathbf{q}). \tag{1.11}$$

Note the $\mathbf{q}$ dependence of the dynamical matrix and the displacements. In an explicit calculation of the dynamical matrix by displacing each of the atoms of the unit cell into all three directions, a periodic supercell has to be used which is commensurate with the phonon wave length $2\pi/q$. Fourier transform of the q-dependent dynamical matrix leads to the real space force constant matrix $C_{st}^{\alpha\beta}(\mathbf{R})$ where $\mathbf{R}$ denotes a vector connecting different unit cells.

A phonon calculation starts thus with a determination of the dynamical matrix in real space or reciprocal space. For hBN and BN tubes, three different approaches have been used: i.) In the force constant approach[54], a reduced set of $C_{st}^{\alpha\beta}(\mathbf{R})$ was fitted in order to reproduce the experimental phonon dispersion relation[55]. ii.) The force constants were obtained from total-energy calculations using a semi-empirical tight-binding approach[56]. iii.) Force constants were obtained from *ab-initio* total energy calculations [12,14]. We will first discuss the equilibrium geometry of nanotubes following from *ab-initio* calculations and afterwards the resulting phonon dispersion and the Raman and IR active modes.

---

[54] V. N. Popov, Phys. Rev. B **67**, 085408 (2003).

[55] E. Rokuta, Y. Hasegawa, K. Suzuki, Y. Gamou, C. Oshima, and A. Nagashima, Phys. Rev. Lett. **79**, 4609 (1997).

[56] D. Sánchez-Portal and E. Hernández, Phys. Rev. B **66**, 235415 (2002).

1.5.2 Equilibrium geometry

In the isolated sheet of hBN, *ab-initio* calculations on the level of DFT-LDA yield a BN-bond length of 1.44 Å which is close to the literature value of 1.45 Å for bulk h-BN. In the tubes, the boron-nitrogen bonds display a buckling [2] [12] with the Nitrogen atoms moving slightly outwards and the Boron atoms moving slightly inwards (see inset of Figure 1.13). This leads to the formation of a negative outer N-cylinder and a positive inner B-cylinder. Figure 1.13 shows that the buckling distance between these two cylinders is to a very good approximation inversely proportional to the tube diameter (except for the tubes with very small diameters where the decrease is faster). The threefold coordinated (and slightly positively charged) Boron atoms have the tendency to keep the planar sp^2 bonding geometry with bond angles of 120° while the (slightly negatively charged) Nitrogen atoms are more susceptible to an admixture of sp^3 hybridization leading to smaller bond angles [2]. With this hypothesis, a very simple explanation of the $1/r$ dependence can be given. The inset of Fig. 1.13 shows a two-dimensional projection of the buckled geometry for a $(n, 0)$ zigzag tube. The nitrogen atoms are located at the corners of the polygon with distance r_N from the center. The boron atoms are accordingly placed at the midpoints of the sides of the polygon. The angle θ is inversely proportional to n and thereby to the tube radius r. Therefore, also the buckling distance is inversely proportional to the radius: $r_N - r_B = r - r\cos\theta \approx r - r(1 - \frac{1}{2}\theta^2) \propto 1/r$. For smaller tube diameters ($D < 7$Å) the strain energy due to the curvature of the tube (see Ref.[2]) becomes so large that the boron atoms no longer keep their planar bonding geometry but also acquire an admixture of sp^3 hybridization.

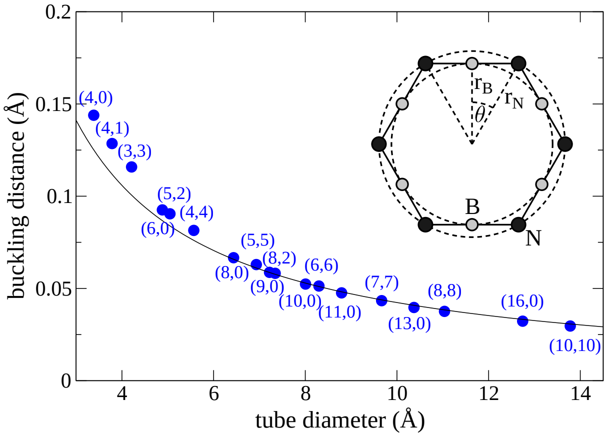

Figure 1.13: Buckling distance in BN single wall nanotubes as a function of tube diameter.

1.5.3 Phonon dispersion relations

Bulk hBN

Detailed information on the phonons in BN tubes is up to date only available from theoretical calculations. In order to check the predictive power of these, we compare first the results of

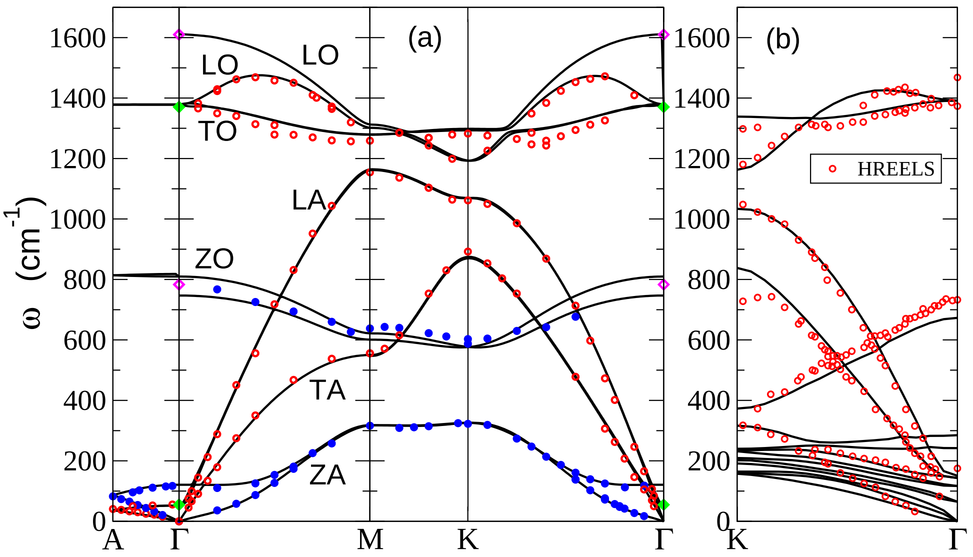

Figure 1.14: (a) Phonon dispersion relations of *h*-BN along the main symmetry directions. The open (red) circles display modes polarized in the hexagonal plane whereas the solid (blue) circles correspond to modes polarized along the c-axis. The solid curves represent the calculated phonon dispersion and infrared[59] and Raman[60] [61] data are displayed at the Γ point by open (magenta) and solid (green) diamonds. (b) Calculated phonon dispersions of a monolayer of *h*-BN deposited on 3 layers of Ni (solid lines) compared to the EELS data from Ref.[55] (red open circles). Note that in the experiment only vibrational modes involving boron or nitrogen atoms were detected while in the calculations also the vibrational modes of the Ni substrate are included.

ab-initio calculations of the phonon dispersion relation of bulk hBN[57] [58] [24] with available experimental data[59] [60] [61] [24].

Hexagonal BN has a crystal structure with 4 atoms in the unit cell and space group P6$_3$/mmc. Hence, the phonon dispersion relations show 12 different branches that can be divided into the 2E$_{1u}$+2A$_{2u}$+2E$_{2g}$+2B$_{1g}$ irreducible representations at the center of the Brillouin zone (Γ-point). The branches are usually classified in the following terms: longitudinal optical (LO) and transverse optical (TO) denote the high frequency in plane optical modes with vibration amplitude parallel/perpendicular to the phonon wave-vector, respectively. Analogous terms are used for the in-plane acoustic (LA and TA) modes. ZA/ZO denote the out-of-plane acoustic/optical modes. At the (Γ-point), the E$_{1u}$ (LO/TO) and A$_{2u}$(ZO) modes are infrared active, the E$_{2g}$(TO/LO) are Raman active. The B$_{1g}$ (ZA and ZO) modes cannot be observed, neither with Raman nor with infrared spectroscopy.

Fig. 1.14 shows the phonon dispersion, measured by inelastic x-ray scattering [24] along with the Raman and IR data at Γ and compared with *ab-initio* calculations. The agreement is very good and confirms the validity of *ab-initio* calculations for the phonons in hBN systems.

---

[57] G. Kern, G. Kresse, and J. Hafner, Phys. Rev. B **59**, 8551 (1999).

[58] W.J. Yu, W.M. Lau, S.P. Chan, Z.F. Liu, and Q.Q. Zheng, Phys. Rev. B **67**, 014108 (2003).

[59] R. Geick, C.H. Perry, G. Rupprecht, Phys. Rev. **146**, 543 (1966).

[60] R.J. Nemanich, S.A. Solin, R.M. Martin, Phys. Rev. B **23**, 6348 (1981).

[61] S. Reich, A.C. Ferrari, R. Arenal, A. Loiseau, I. Bello, J. Robertson, Phys. Rev. B **71**, 205201 (2005).

BN is a polar material. In the optical modes, the positive ions vibrate in opposition to the negative ions which leads to a local time-dependent dipole moment. The resulting crystal field gives rise to a splitting between the LO E$_{1u}$ and the TO E$_{1u}$ modes (Lyddanne-Sachs-Teller relation). In contrast, the E$_{2g}$ modes are doubly degenerate at Γ and the LO E$_{2g}$ mode displays a strong overbending close to Γ.

The gap between the ZA and ZO modes at the K point, predicted by the theoretical models, is well reproduced by the IXS data. Contrary to this, in the EELS (electron-energy loss spectroscopy) measurements of Rokuta *et al.*[55] on a monolayer of *h*-BN deposited on a Ni(111) substrate, an almost-degeneracy of ZA and ZO was found at K. This is caused by the influence of the interlayer-interaction with the substrate. The influence of the binding to the Ni substrate has been demonstrated by *ab-initio* calculations of the phonon dispersion of a BN-sheet on a Nickel surface. The calculated dispersion [24] and the EELS data are in excellent agreement, as displayed in Fig. 1.14(b). The differences between the EELS and IXS dispersions can therefore be attributed to the binding between the hBN monolayer and the Ni substrate.

We remark that although modes related to interlayer vibrations should be very much sensitive to errors in the correlation functional (as the typical variations in the correlation energy that has to be resolved are up to 2 orders of magnitude smaller for interlayer phonons than for structural characterization), a description of exchange-correlation effects beyond the LDA do not modify the phonon dispersion relations shown in Fig. 1.14 [62], indicating the robustness and accuracy of the present DFT-based approach to describe the ion-dynamics in polar-nanostructures.

Single sheet of hBN

The calculated phonon dispersion of the single hexagonal BN-sheet is presented in Fig. 1.15 together with the one of a single graphene sheet. In general, the phonons of the BN-sheet are softer than the phonons of the graphene sheet: the purely covalent bonds of graphene are stronger than the (mostly covalent, but partially ionic) bonds of BN. Furthermore, the degeneracy at K of the out-of-plane acoustic and optical (ZA and ZO) modes and the degeneracy of the longitudinal acoustic and optical (LA and LO) modes in graphene is lifted in BN due to the different masses of B and N. Fig. 1.16 presents sketches of the optical phonons of the BN-sheet at Γ.

The phonon dispersion relation of the sheet follows very closely the *ab initio* calculated dispersion relation of bulk hexagonal BN when one subtracts the phonon branches that are influenced by the inter-plane interaction. This is analogous to the comparison of phonon dispersion relations of the graphene sheet[63] and of bulk graphite [17] and is due to the fact that the inter-layer interaction is much weaker than the interaction between atoms within one layer. The effect of LO-TO splitting is absent in a 2-dimensional single sheet. However, the LO mode displays an overbending close to Γ that is more pronounced than the overbending in the corresponding bulk LO mode. The phonon-dispersion of the sheet will be used below in order to derive the phonon-dispersion and the diameter-dependence of phonons of the tubes via the zone-folding procedure.

---

[62] A. Marini, P. García-Gonzalez and A. Rubio, Phys. Rev. Lett. **96**, 136404 (2006).

[63] O. Dubay and G. Kresse, Phys. Rev. B **67**, 035401 (2003).

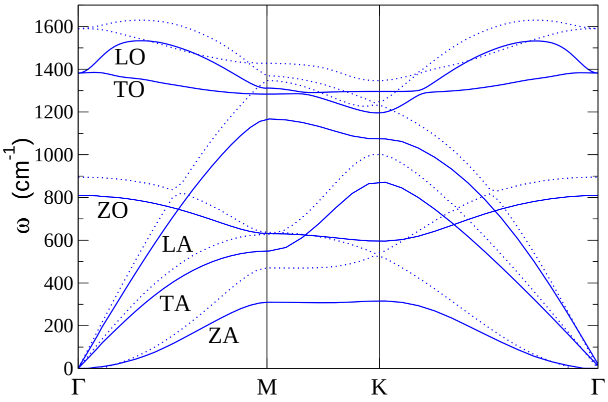

Figure 1.15: Calculated phonon dispersion relation of the single hexagonal BN sheet (solid lines) in comparison with graphene (dotted lines).

Tubes

In Fig. 1.17 we compare the ab initio phonon dispersion relation of a (6,6) BN nanotube with the corresponding zone-folding dispersion relation. The zone-folding method works equally good as in the case of carbon nanotubes [63]. Here and there, the major difference lies in the low frequency part of the spectrum and is due to the coupling of in-plane and out-of-plane modes of the sheet upon rolling into a tube. This leads to a stiffening of the low-frequency tube modes with respect to the zone-folding model. In general, the zone-folding method does not only reproduce quite well the dispersion relation, but also yields a good estimate of the total phonon density of states (right panel of Fig. 1.17).

1.5.4 Symmetry Analysis

In Raman and IR spectroscopy, only phonons at (or close to) the Γ-point of the 1-dim Brillouin zone can be excited (as long as we restrict our discussion to first order processes). Furthermore, in Raman spectroscopy, only modes that transform under symmetry operations as a quadratic form are active, in IR spectroscopy only modes that transform as a vector[64] For (infinitely extended) systems with translational symmetry, the "point group in the space group" determines through the selection rules which modes are active and which are not. In quasi-one-dimensional systems with translational symmetry, it is accordingly the "point group in the rod group" that has to be evaluated[65] Fig. 1.18 summarizes the findings for BN-tubes: It can be easily seen that the unit-cell of a $(n, 0)$ zigzag-tube possesses an n-fold rotation axis (with rotation angle $\phi = 2\pi/n$). In addition, n (indeed, even 2n) vertical reflection-symmetry planes (containing the tube axis) can be found. Thus the unit cell of a zigzag tube transforms under the C_{nv} symmetry group. In the infinitely extended tube, the operations of the C_{nv} point group are valid as well, but - in addition - a rotation by $\phi/2$ with subsequent translation by $T/2$ also maps the system onto itself. This leads to the conclusion that for the infinitely

---

[64] The selection rules for Raman and IR spectroscopy are discussed in many textbooks. E.g., a nice introduction can be found in: D. C. Harris and M. D. Bertolucci, *Symmetry and Spectroscopy: an Introduction to Vibrational and Electronic Spectroscopy* (Dover, New York, 1989).

[65] O. E. Alon, Phys. Rev. B **63**, 201403 (2001).

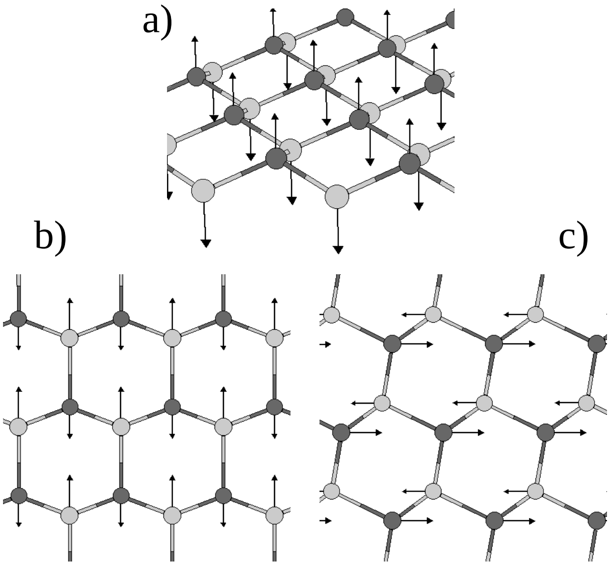

Figure 1.16: Sketch of the optical phonon modes at Γ in the hexagonal BN-sheet: a) out-of-plane mode, b) transverse optical (TO) mode, c) longitudinal optical (LO) mode. For the assignment of "transverse" and "longitudinal", the phonon wave-vector points in horizontal direction with $q \rightarrow 0$.

extended system, the C_{2nv} symmetry group is the relevant one for symmetry analysis of Raman and IR active modes. Analogously, for (n,n) armchair tubes, the symmetry group of the unit-cell is C_{nh} and the symmetry group of the infinitely extended tube is C_{2nh}. Finally, for chiral (n,m) tubes, the unit-cell has the low point-group symmetry C_d, where d is the greatest common divisor of n and m. However, the infinitely extended tube is described by the C_N symmetry group, where N is the number of hexagons (= two times the number of atoms) per unit cell which is, in general, much larger than d.

The number of active modes is found by determining how often each irreducible representation appears in the (reducible) representation of the symmetry group (C_{2nv}, C_{2nh}, or C_N, respectively) which is given by the $12n$ vibrational degrees of freedom of the unit cell. For zigzag tubes this leads to 14 Raman active modes[65] (3 with A_1 symmetry, 5 with E_1 symmetry, and 6 with E_2 symmetry, where the E_1 and the A_1 modes with vanishing frequency have already been subtracted). Out of these modes, 8 modes ($3A_1$ and $5E_1$) are also IR active. In the case of chiral tubes, there are 15 Raman active modes ($4A$, $5E_1$, and $6E_2$) out of which 9 modes ($4A$ and $5E_1$) are also IR active. The small difference in the number of active modes between zigzag and chiral tubes stems from the fact that the additional vertical reflection symmetry of the zigzag tube causes a distinction between Raman+IR active A_1 modes and non-active A_2 modes. The sets of Raman and IR active modes for BN armchair tubes are disjoint: 9 modes are Raman active (3 with A_g symmetry, 2 with E_{1g} symmetry and 4 with E_{2g} symmetry) and 4 modes are IR active (1 with A_u symmetry and 3 with E_{1u} symmetry)[66].

---

[66] The fact that for zigzag and chiral tubes, the IR active modes are a a subset of the Raman active modes is different in BN-tubes and C-tubes and is due to the reduced symmetry (= less strict selection rules) for BN-tubes. In carbon tubes, only the set of IR active modes of chiral tubes partially overlaps with the set of Raman active modes[65]. For zigzag and armchair C-tubes, the sets of Raman and IR active modes are disjoint.

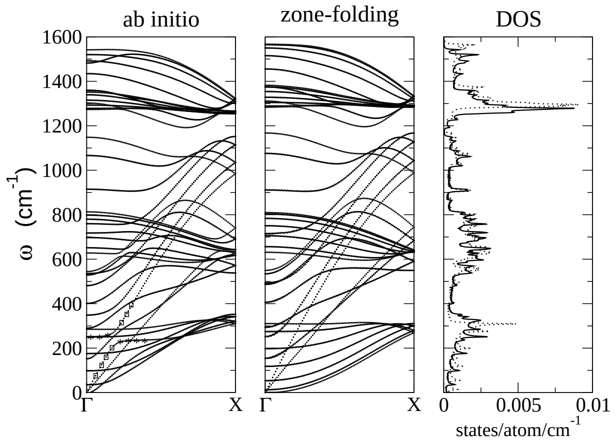

Figure 1.17: Calculated phonon dispersion relation and density of states (DOS) in the $(6,6)$ armchair BN-nanotube. We compare the results of *ab initio* calculations with the zone-folding method (see text for details). In the right panel the solid line is the *ab initio* DOS and the dotted line the zone-folding DOS. The symbols in the left panel indicate the avoided crossing between the RBM (asterisks) and the longitudinal acoustic A_1 mode (boxes).

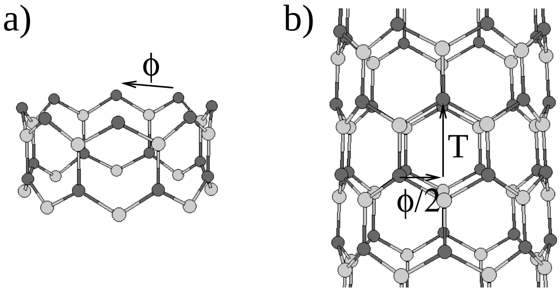

Figure 1.18: Comparison of the point-group symmetry of the unit cell with the space-group symmetry of zigzag BN-tubes.

In the next section, it will be explained how these modes can be constructed from the modes at or close to the Γ-point in the BN-sheet.

1.5.5 Zone-folding method

Here, we review the zone-folding method which has been frequently used for the calculation of electronic band structure and phonons in C-nanotubes[67] and demonstrate how the different Raman and Infrared active modes can be deduced from it in the case of BN-nanotubes. Thus, the symmetry analysis of the previous section can be understood in a pictorial way. Fig. 1.19 a) demonstrates the scenario for $(n,0)$ zigzag nanotubes. The sheet is rolled up such that the tube-axis is parallel to the translation vector $\vec{T}$ whose lengths corresponds to the lengths of the 1-dimensional unit-cell of the tube. The component $K_\perp$ of the phonon wave vector $\vec{K}$ which points into the circumferential direction of the tube is quantized. For zigzag nanotubes, this

---

[67] R. Saito, G. Dresselhaus, and M. S. Dresselhaus, *Physical Properties of Carbon Nanotubes* (Imperial College Press, London, 1998).

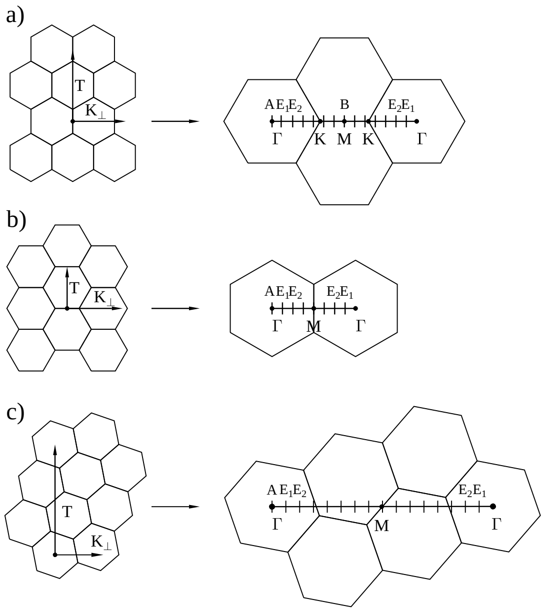

Figure 1.19: Sketch of the zone-folding method a) for $(n, 0)$ zigzag nanotubes, b) for (n, n) armchair nanotubes, and c) for $(4n, n)$ chiral nanotubes. Left side: A hexagonal BN-sheet is rolled in perpendicular direction to the primitive translation vector $\vec{T}$. The component $K_\perp$ of the phonon wavevector in circumferential direction is quantized. Right side: For zigzag nanotubes, the quantization of the circumferential momentum corresponds to $2n$ steps along the line $\Gamma \rightarrow K \rightarrow M \rightarrow K \rightarrow \Gamma$ in the 2-dim Brillouin zone of the sheet. In armchair nanotubes $2n$ discrete steps are taken along the line $\Gamma \rightarrow M \rightarrow \Gamma$, while in chiral tubes the discretization proceeds along a line connecting more distant Γ-points. The points at and close to Γ give rise to the Raman and IR active A, E_1, and E_2 modes.

means that in reciprocal space, $K_\perp$ can assume $2n$ discrete values ($\mu = 0, \ldots, 2n-1$) along the line $\Gamma \rightarrow K \rightarrow M \rightarrow K \rightarrow \Gamma$. The parallel component $K_\parallel$ is unrestricted. However, the Raman and IR active modes are modes at the Γ-point of the 1-dim Brillouin zone of the tube and correspond thus to $K_\parallel = 0$. Since the points at μ and $2n - \mu$ are equivalent in reciprocal space, all modes of the tube are doubly degenerate, except for the mode that corresponds to $\mu = 0$ (the Γ-point of the sheet) and the mode that corresponds to $\mu = n$ (the M-point of the sheet). If one applies the strict selection rules according to the C_{2nv} symmetry group, the modes of the sheet at Γ map onto tube modes with A symmetry, the modes at M map onto modes of B symmetry and the modes at $\mu = 1, \ldots, n-1$ map onto modes of symmetry $E_1, \ldots, E_{n-1}$. Since there are six different phonon branches in the sheet, there are six different phonon modes in the tube for each of the above symmetries. Each of the six phonon branches leads to $n+1$ different phonon modes in the tube, $(n-1)$ E modes, one A mode, and one B mode. Since the E modes are doubly degenerate, this sums up to $12n$ phonon modes corresponding to the $4n$ atoms in the unit cell of a zigzag tube.

Figs. 1.16 and 1.20 demonstrate the mapping of the three optical modes of the sheet at Γ onto the corresponding A modes of the tube. The out-of-plane optical (ZO) modes of the sheet lead to radial (R) "buckling" modes of the tube where all Boron atoms move inwards/outwards at the same time and all Nitrogen atoms move outwards/inwards, giving rise to an oscillation of the buckling amplitude in the tube. The transverse optical (TO) mode of the sheet maps onto a longitudinal (L) mode of the tube and, accordingly, the longitudinal optical (LO) mode of the sheet maps onto a transverse or tangential (T) mode of the tube. In the A modes, all atoms along the circumference move in phase (corresponding to $K_\perp = 0$). In the modes of E_i symmetry, there are $2i$ nodes along the circumference (i nodal planes containing the symmetry axis of the tube). The B modes contain $2n$ nodes along the circumference which means that a rotation by $\phi/2$ (with the proper translation along the tube axis) maps the mode onto its negative. In other words, for the B modes, neighboring "columns" of atoms oscillate with a phase difference of π.

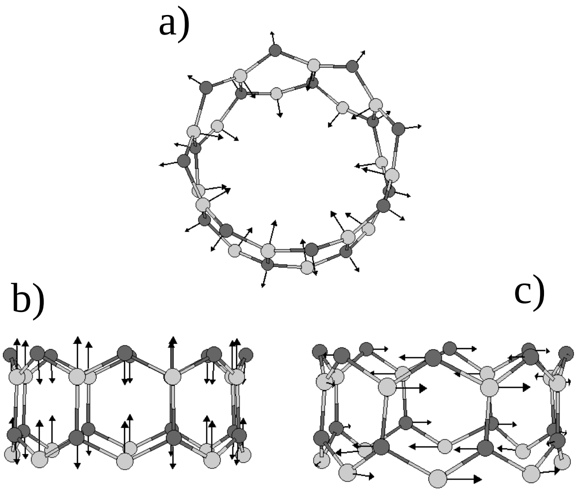

Figure 1.20: Sketch of high frequency A modes in a BN-zigzag tube: a) radial buckling (R) mode, b) bond-stretching or longitudinal (L) mode, c) bond-bending or tangential (T) mode.

The points in the Brillouin zone of the sheet that give rise to the Raman and IR active A, E_1, and E_2 modes are denoted in Fig. 1.19. They are the points at and close to Γ. With larger tube diameter (increasing n), the points giving rise to the E_1 and E_2 modes converge towards the Γ-point of the BN-sheet. Therefore, as a first check on the frequencies of active modes of large diameter tubes, it is sufficient to look at the frequencies at the Γ-point of the sheet. The frequencies of modes that correspond to the acoustic branches of the sheet converge accordingly to zero for large diameters. Note that not all of the A, E_1, and E_2 modes may be Raman active, because one still has to distinguish between the different "sub-symmetries". E.g. the TO mode of the sheet at Γ (see Fig. 1.16 b) folds into a tube mode of A_1 symmetry (see Fig. 1.20 b) and is thus Raman active, whereas the LO mode of the sheet at Γ (see Fig. 1.16 c) folds into a mode of A_2 symmetry (see Fig. 1.20 c) which changes sign under reflection at a plane that contains the symmetry axis of the tube.

The zone-folding for armchair tubes works in an analogous way to the zone-folding for zigzag tubes (see Fig. 1.19 b). The only difference is that the active modes of the tube correspond to a discrete set of modes along the line $\Gamma \rightarrow M \rightarrow \Gamma$ in the reciprocal space of the sheet.

Finally, Fig. 1.19 c) illustrates the zone-folding for a general chiral nanotube. In the example, we have chosen a (4n,n) tube with a relatively short primitive translation vector $\vec{T}$. As in the case of armchair and zigzag tubes, the quantization of the circumferential phonon wave vector corresponds in the reciprocal space of the sheet to a discrete set of modes along a line $\Gamma \rightarrow M \rightarrow \Gamma$. However, the line does not connect nearest or next-nearest Γ-points but connects Γ-points further apart (with the distance depending on the chirality of the tube).

1.5.6 Diameter-dependence of Raman and IR active modes

In this section we present the results of ab-initio calculations of selected zigzag, chiral and armchair tubes [12] and compare with the results obtained by zone-folding the *ab initio* dispersion relation of the single sheet. Figure 1.21 displays the frequencies of the Raman and IR active modes of the three types of tubes as a function of the tube diameter D. The *ab initio* values are plotted as symbols, while the zone-folding values are connected by lines in order to guide the eye and extrapolate to larger tube diameters. Three frequency regimes are easily distinguishable:
1.) The low frequency modes whose frequencies approach zero for $D \rightarrow \infty$ are the modes that are derived from the acoustic branches of the sheet.
2.) The three modes that approach $\omega \approx 818cm^{-1}$ for $D \rightarrow \infty$ are radial (R) modes (see Fig. 1.20 a) which are related to the optical out-of-plane (ZO) modes (Fig. 1.16 a) in the dispersion relation of the sheet (Fig. 1.15).
3.) The high frequency regime above $1200cm^{-1}$ consists of longitudinal (L) and transverse (T) modes (Fig. 1.20 b,c) which are zone-folded TO and LO modes of the sheet (Fig. 1.16 b,c)
We discuss at first the three different frequency regimes separately in the case of the zigzag tubes (left panel of Fig. 1.21). Afterwards, we extend the discussion to the chiral and armchair tubes.

Fig. 1.22 is a double-logarithmic plot of the low frequency modes in the zigzag nanotubes. For the RBM (marked by asterisks), we have also included the values of chiral and armchair tubes. From phonon calculations in C-nanotubes, it is well known that the RBM is inversely proportional to the tube diameter[68]: $\omega_{RBM} \propto 1/D$. The same holds for BN-nanotubes. In fact, not only the RBM, but most of the low frequency modes display the same $1/D$ scaling. This can be easily understood from the phonon dispersion of the sheet (Fig. 1.15) in combination with the zone-folding procedure in Fig. 1.19: The LA and TA branches of the sheet have a linear slope at the Γ-point. The distance between the Γ-point and the points that map onto the E_1 and E_2 modes in Fig. 1.19 are proportional to $1/N$ (with N being the number of hexagons in the tube unit cell) and hence proportional to $1/D$. Hence, all the low frequency modes in the tubes that are folded from the LA and TA branches of the sheet exhibit the $1/D$ scaling. Only the frequency of the lowest E_2 mode in Fig. 1.22 displays a $1/D^2$ proportionality[63]. This is because it is folded from the ZA mode of the sheet which does not increase linearly but quadratically around the Γ-point [67]. For small diameter, the phonon modes deviate from the functional form A/D or A/D^2, because the linear/quadratic behavior in the acoustic branches of the sheet ceases to be valid further away from the Γ

---

[68] R. A. Jishi, L. Venkataraman, M. S. Dresselhaus, and G. Dresselhaus, Chem. Phys. Lett. **209**, 77-82 (1993).

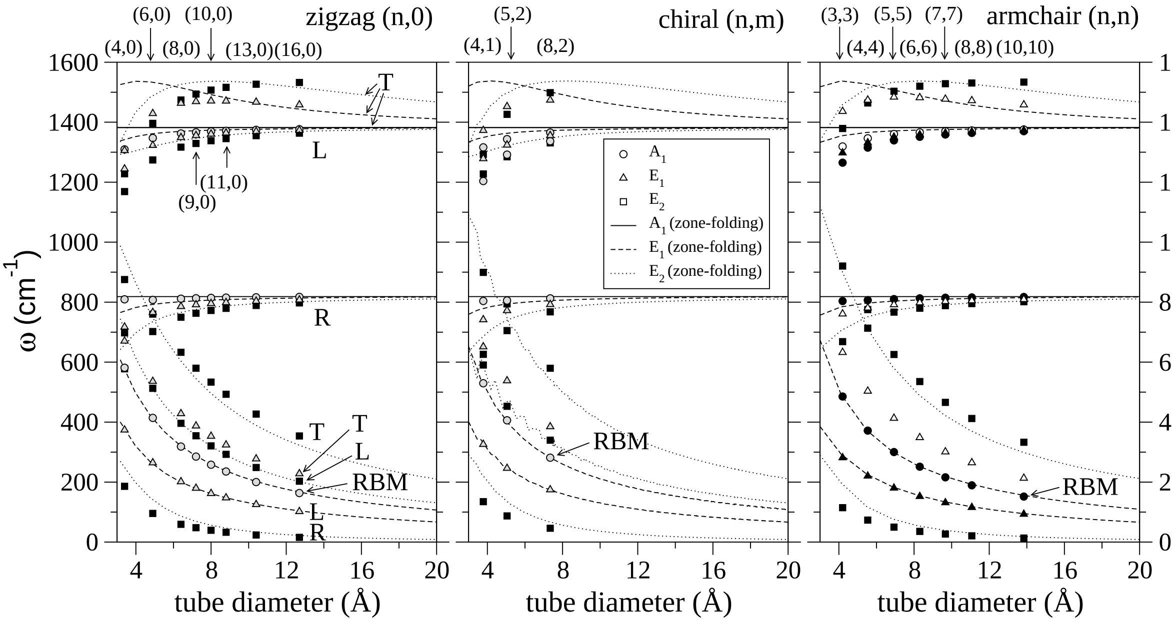

Figure 1.21: Frequencies of Raman and IR active modes in BN-nanotubes as a function of tube diameter: comparison of ab-initio values (symbols) with zone-folding method (lines). The shape of the symbols denotes the symmetry of the modes (see legend). Black filling marks modes which are Raman active only. White filling stands for IR active only. Grey filling stands for modes which are both Raman and IR active. R, L, T marks the radial, longitudinal, and tangential high frequency modes (as in Fig. 1.20)

point. Only the RBM follows the functional behavior A/D down to very low radius. While the RBM cannot be obtained from zone-folding of an *infinite* sheet, it is related to the in-plane stretching mode of a sheet of *finite* width [12] and the functional A/D behavior can be proven analytically[68].

The power law fit of the RBM scaling in Fig. 1.22 yields a scaling constant $A = 2060 \pm 2$ cm^{-1}Å and may be used for the diameter determination in Raman characterization of BN-tubes. As is the general trend of phonons in BN as compared to carbon, this value is considerably lower than the corresponding *ab initio* value $A_C = 2288$ cm^{-1}Å for the RBM in carbon nanotubes[69] [63]. Since the other low frequencies modes with the $1/D$ scaling may be used as well for the radius determination, we list in table 1.1 the corresponding scaling constants.

We discuss now the radial phonon modes in the intermediate frequency regime around 800 cm^{-1} (see, e.g., panel a) of Fig. 1.21). According to the zone-folding picture, the A mode should be diameter independent and have the constant frequency of ≈ 818 cm^{-1}. Indeed, the *ab initio* values lie almost exactly on this line. The E_1 branch is the nearest neighbor in frequency of the A mode and the E_2 branch is the next nearest neighbor, because in the zone-folding picture (Fig. 1.19), the E_1 and E_2 modes derive from the points close to the Γ-point of the sheet. Since in the dispersion relation of the BN-sheet (Fig. 1.15), the ZO branch approaches the Γ-point from below, the radial E_1 and E_2 modes both have lower frequencies than the corresponding A mode. At small diameters, the *ab initio* values lie below

---

[69] J. Kürti, G. Kresse, and H. Kuzmany, Phys. Rev. B **58**, R8869 (1998).

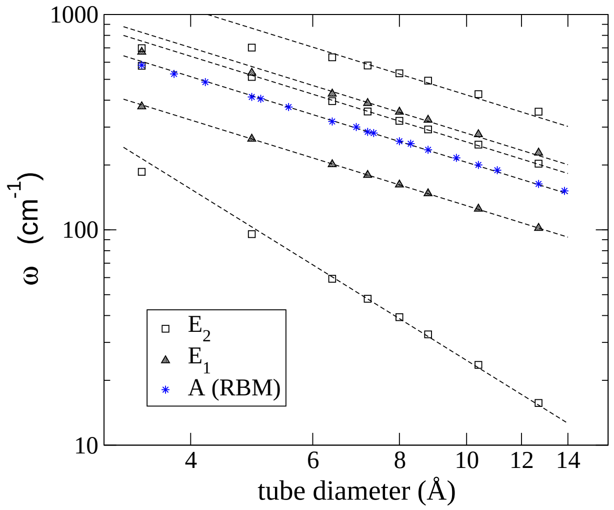

Figure 1.22: Double-logarithmic plot of the low phonon frequencies in the BN zigzag tubes. The dashed lines are least square fits to the form A/D^2 for the lowest E_2 mode and to the form A/D for all other modes. The fit has been performed on the diameter interval between 6 Å and 14 Å.

the zone-folding curves due to bond weakening introduced by curvature effects.

The L and T modes of the high-frequency branch converge towards the asymptotic value $\omega = 1380$ cm^{-1} for $D \rightarrow \infty$. In the zone-folding picture, the E_1 and E_2 L modes approach this value from below since in the dispersion relation of the sheet (Fig. 1.15), the corresponding TO branch from which these modes are derived approach the Γ point from below. The LO branch, in contrast, displays a strong over-bending which leads to the non-monotonic diameter scaling of the E_1 (T) and E_2 (T) modes in Fig. 1.21. The *ab initio* values follow the general trend of the zone-folding curves. However, all high-frequency T and L modes, even the A modes which should be diameter independent, experience a strong down-shift for small diameter. This general trend is also observed for the C nanotubes[63] and can be attributed to curvature effects. The E_1 (T) mode displays the non-monotonic behavior which is predicted by zone-folding, but due to the curvature induced softening at small radius, it reaches the maximum at a larger diameter than the zone-folding curve. The E_2 (T) mode displays a similar behavior. It reaches its maximum at a larger diameter than the E_1 (T) mode and ultimately converges towards the asymptotic value of 1380 cm^{-1}.

The scaling of the phonon frequencies with the tube diameter is very similar for zigzag, chiral and armchair tubes as can be seen from comparing the three panels of Fig. 1.21. In the case of the chiral tubes, the zone-folding lines of the low frequency L modes and - to a lesser extent - the ones of the low frequency T modes display a zigzag pattern. We have calculated all chiral nanotubes in the diameter range between 3 and 20 Å and connected the discrete points by lines in order to guide the eye. For large diameter, the frequencies of the low frequency modes follow the same scaling as given in Table 1.1 for the zigzag tubes. This is because the slope of the acoustic branches of the sheet at Γ is independent of the direction in the Brillouin zone (corresponding to an isotropic sound velocity in all directions). Only at smaller diameter, corresponding to larger distance from the Γ-point in the dispersion relation of the sheet where the LA and TA modes deviate from the linear behavior, the frequency

mode symmetry	A/cm^{-1}Å
E_1 (L)	1296
A (RBM)	2060
E_2 (L)	2560
E_1 (T)	2808
E_2 (T)	4232

Table 1.1: First principle determination of scaling constants for the A/D dependence of the low frequency modes as a function of the tube diameter D.

clearly depends on the chiral angle. The slopes of the zigzag and of the armchair curves are the limiting cases. E. g., the zone folding curve of the E_2 (T) mode reaches a value of 1000 cm^{-1} at $D = 3$Å for the zigzag tubes and a value of 1100 cm^{-1} for the armchair tubes.

In Fig. 1.21, only Raman or IR active modes are shown. This leads to a different number of displayed values in the three different panels. The fact that for zigzag and chiral tubes, the IR active modes are a subset of the Raman active modes while for armchair tubes the two sets are disjoint, should help in the experimental identification of the ratio of different chiralities in a macroscopic tube sample. In particular, the RBM can be detected both by Raman and IR spectroscopy in zigzag and chiral tubes, while in the case of armchair tubes, it should only appear in the Raman spectrum. Of course, an exact theoretical calculation of the chirality dependence of IR and Raman *intensities* is desirable for this purpose.

1.5.7 Raman intensities

So far, we have discussed only the position of the peaks in the Raman spectra. The positions are given by the frequencies ω_ν of the Raman active modes ν with null wave vector. Raman scattering in BNNTs takes place in the non-resonant regime, because the optical-gap of BNNTs exceeds the photon energies of lasers in the visible and near UV-range. The intensities for non-resonant Raman scattering, I^ν, can be written within the Placzek approximation[70].

$$I^\nu \propto |\mathbf{e}_i \cdot \mathbf{A}^\nu \cdot \mathbf{e}_s|^2 \frac{1}{\omega_\nu}(n_\nu + 1) \ . \tag{1.12}$$

Here $\mathbf{e}_i$ ($\mathbf{e}_s$) is the polarization of the incident (scattered) light and $n_\nu = [\exp(\hbar\omega_\nu/k_B T) - 1]^{-1}$ with T being the temperature. The Raman tensor $\mathbf{A}^\nu$ is

$$A^\nu_{ij} = \sum_\gamma B^{k\gamma}_{ij} \frac{w^\nu_{k\gamma}}{\sqrt{M_\gamma}}, \tag{1.13}$$

where $w^\nu_{k\gamma}$ is the kth Cartesian component of atom γ of the νth orthonormal vibrational eigenvector and M_γ is the atomic mass.

$$B^{k\gamma}_{ij} = \frac{\partial^3 \mathcal{E}}{\partial E_i \partial E_j \partial u_{k\gamma}} = \frac{\partial \alpha_{ij}}{\partial u_{k\gamma}}, \tag{1.14}$$

---

[70] *Light Scattering in Solids II*, edited by M. Cardona and G. Güntherodth (Springer-Verlag, Berlin, 1982).

where $\mathcal{E}$ is the total energy of the unit cell, $\mathbf{E}$ is a uniform electric field and $u_{k\gamma}$ are atomic displacements. This is equivalent to the change of the electronic polarizability of a unit cell, $\alpha_{ij} = \Omega\chi_{ij}$ (where Ω is the unit cell volume and χ_{ij} the electric susceptibility), upon the displacement $u_{k\gamma}$. The derivative tensor $B_{ij}^{k\gamma}$ can either be calculated approximately from a bond-polarizability model[54] [19] or can be calculated *ab-initio* with an extension of density-functional perturbation theory[71]

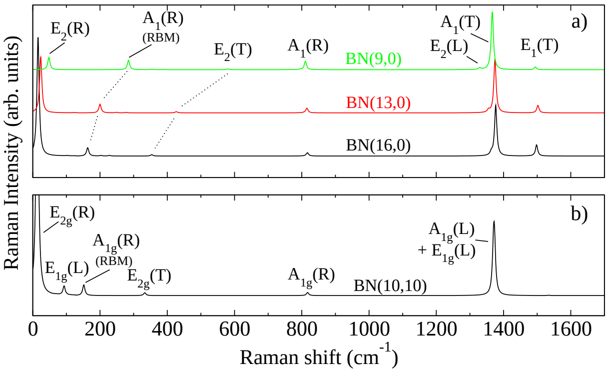

Figure 1.23: Calculated Raman intensities for a) three different zigzag BNNTs and b) the (10,10) armchair BNNT. The spectra are plotted with a full-width at half-maximum (FWHM) of 10 cm^{-1}.

We show in Fig. 1.23 the *ab-initio* Raman spectra [19] for the (9,0), (13,0), and (16,0) zigzag BN nanotubes and for the (10,10) armchair tube. The latter two have diameters (12.8 Å and 13.8 Å) in the range of experimentally produced BN tubes. The dominant peak (besides the low frequency E$_2(R)$ which is close to zero and thus hardly measurable) is the A$_1$ peak at about 1370 cm^{-1}. Note that for zigzag tubes this mode corresponds to a transverse (T) vibration of the atoms while for armchair tubes it corresponds to a longitudinal (L) vibration. Depending on the chirality of the tube, the dominant peak can have a side peak on the lower frequency side. With increasing diameter, this side-peak rapidly merges into the main-peak but remains visible as a shoulder. About 120 cm^{-1} above the main peak, The E$_1$(T) mode gives a small contribution to the spectrum. For chiral tubes, its intensity is reduced and becomes zero for armchair tubes. If Raman spectra of isolated single-walled BN tubes ever become available (due to the non-resonant character of the spectra, the intensity is very low), the intensity of this peak with respect to the intensity of the main peak can be taken as a measure of the tube chirality. The A$_1$ mode at 810 cm^{-1} is the radial buckling mode. Its intensity decreases with increasing diameter. Therefore it is not clear if it is detectable. In the low frequency regime, the radial breathing mode plays the dominant role and is a good measure for the radius of the tube (just as in the case of carbon nanotubes).

For the calculation of Raman intensities of large diameter BN nanotubes, we implemented a bond-polarizability model. The model includes local field effects which is important for the Raman scattering with light polarized perpendicularly to the tube axis. The details of this model can be found in Ref. [19] which is reprinted in the following.

---

[71] M. Lazzeri and F. Mauri, Phys. Rev. Lett. **90**, 036401 (2003).

RAPID COMMUNICATIONS

PHYSICAL REVIEW B **71**, 241402(R) (2005)

Raman spectra of BN nanotubes: *Ab initio* and bond-polarizability model calculations

Ludger Wirtz,[1,*] Michele Lazzeri,[2] Francesco Mauri,[2] and Angel Rubio[1]
[1]*Department of Material Physics, University of the Basque Country, Centro Mixto CSIC-UPV,*
and Donostia International Physics Center (DIPC), Po. Manuel de Lardizabal 4, 20018 Donostia-San Sebastián, Spain
[2]*Institut de Minéralogie et de Physique des Milieux Condensés, 4 Place Jussieu, 75252 Paris cedex 05, France*

(Received 2 February 2005; revised manuscript received 14 April 2005; published 6 June 2005)

We present *ab initio* calculations of the nonresonant Raman spectra of zigzag and armchair BN nanotubes. In comparison, we implement a generalized bond-polarizability model where the parameters are extracted from first-principles calculations of the polarizability tensor of a BN sheet. For light polarization along the tube axis, the agreement between model and *ab initio* spectra is almost perfect. For perpendicular polarization, depolarization effects have to be included in the model in order to reproduce the *ab initio* Raman intensities.

DOI: 10.1103/PhysRevB.71.241402 PACS number(s): 78.30.−j, 78.20.Bh, 81.07.De, 71.15.Mb

Besides its success in the characterization of a large range of materials,[1] Raman spectroscopy has also developed into an invaluable tool for the characterization of nanotubes. Since the first characterization of (disordered) carbon nanotube (CNT) samples,[2] the technique has been refined, including, e.g., polarized Raman studies of aligned nanotubes[3] and isolated tubes.[4] On the theoretical side, nonresonant Raman intensities of CNTs have been calculated within the bond-polarizability model.[5,6] The empirical parameters of this model are adapted to fit experimental Raman intensities of fullerenes and hydrocarbons. However, the transferability of the parameters and the quantitative performance in nanotubes, in particular distinguishing between metallic and semiconducting tubes, is still not clear.

In this Rapid Communication, we report on the Raman spectra of boron nitride nanotubes (BNNTs).[7,8] Recently, synthesis of BNNTs in gram quantities has been reported.[9] Their characterization through Raman and infrared spectroscopy is expected to play an important role. However, due to difficulties with the sample purification no experimental data on contamination-free samples has been reported. *Ab initio*[10] and empirical[11,12] phonon calculations have determined the position of the peaks in the spectra. However, due to missing bond-polarizability parameters for BN, the Raman intensities have been so far addressed using the model bond-polarizability parameters of carbon.[12] Only the intensities of high-frequency modes were presented, as it was argued that the intensity of low-frequency modes are very sensitive to the bond-polarizability values.[12] Here, we derive the polarizability parameters for BN sp^2 bonds from a single hexagonal BN sheet by calculating the polarizability tensor and its variation under deformation. We compare the resulting spectra for BNNTs with full *ab initio* calculations. We derive conclusions about the general applicability of the bond-polarizability model for semiconducting CNTs.

In nonresonant first-order Raman spectra, peaks appear at the frequencies ω_ν of the optical phonons ν with null wave vectors. The intensities I^ν are given in the Placzek approximation[1] as

$$I^\nu \propto |\mathbf{e}_i \cdot \mathbf{A}^\nu \cdot \mathbf{e}_s|^2 \frac{1}{\omega_\nu}(n_\nu + 1). \quad (1)$$

Here $\mathbf{e}_i(\mathbf{e}_s)$ is the polarization of the incident (scattered) light and $n_\nu = [\exp(\hbar\omega_\nu / k_B T) - 1]^{-1}$ with T being the temperature. The Raman tensor $\mathbf{A}^\nu$ is

$$A^\nu_{ij} = \sum_{k\gamma} B^{k\gamma}_{ij} \frac{w^\nu_{k\gamma}}{\sqrt{M_\gamma}}, \quad (2)$$

where $w^\nu_{k\gamma}$ is the kth Cartesian component of atom γ of the νth orthonormal vibrational eigenvector and M_γ is the atomic mass.

$$B^{k\gamma}_{ij} = \frac{\partial^3 \mathcal{E}}{\partial E_i \, \partial E_j \, \partial u_{k\gamma}} = \frac{\partial \alpha_{ij}}{\partial u_{k\gamma}}, \quad (3)$$

where $\mathcal{E}$ is the total energy of the unit cell, $\mathbf{E}$ is a uniform electric field and $u_{k\gamma}$ are atomic displacements. This is equivalent to the change of the electronic polarizability of a unit cell, $\alpha_{ij} = \Omega \chi_{ij}$ (where Ω is the unit cell volume and χ_{ij} the electric susceptibility), upon the displacement $u_{k\gamma}$. The phonon frequencies and eigenvectors[10] are determined by density functional perturbation theory[13] as implemented in the code ABINIT.[14] For the determination of the derivative tensor $B^{k\gamma}_{ij}$ we proceed in two ways: (i) we calculate it from first principles using the approach of Ref. 15 and (ii) we develop a generalized bond-polarizability model.

The basic assumption of the bond-polarizability model[1,16,17] is that the total polarizability can be modeled in terms of single bond contributions. Each bond is assigned a longitudinal polarizability, α_l, and a polarization perpendicular to the bond, α_p. Thus, the polarizability contribution α^b_{ij} of a particular bond b is

$$\alpha^b_{ij} = \frac{1}{3}(2\alpha_p + \alpha_l)\delta_{ij} + (\alpha_l - \alpha_p)\left(\hat{R}_i \hat{R}_j - \frac{1}{3}\delta_{ij}\right), \quad (4)$$

where $\hat{R}$ is a unit vector along the bond. The second assumption is that the bond polarizabilities only depend on the bond length R. This allows the calculation of the derivative with respect to atomic displacement, $\partial \alpha^b_{ij} / \partial u_{k\gamma}$, in terms of four

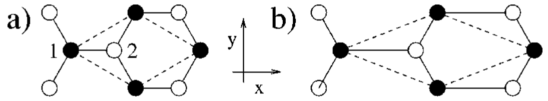

FIG. 1. Unit cell (marked by dashed line) of a BN sheet for the calculation of the bond-polarizability parameters: (a) equilibrium geometry, (b) geometry with one bond elongated.

TABLE I. Parameters of the bond polarizability model extracted from *ab initio* calculations (see text).

	R (Å)	α_l(Å^3)	α_p(Å^3)	α_l'(Å^2)	α_p'(Å^2)
BN sheet	1.44	3.31	α_{pi}:0.28 α_{po}:0.44	1.03	α_{pi}':6.60 α_{po}':0.77
c-BN	1.56	1.58	0.42	4.22	0.90
Diamond	1.53	1.69	0.71	7.43	0.37

parameters $\alpha_l(R)$, $\alpha_p(R)$, $\alpha_l'(R)$, and $\alpha_p'(R)$ (see, e.g., Ref. 17). The use of only one perpendicular parameter α_p implicitly assumes cylindrical symmetry of the bonds. That can be justified in a sp^3 bonding environment. However, in the highly anisotropic environment in a sheet of sp^2 bonded carbon or BN and the corresponding nanotubes this assumption seems hardly justified. In our model we therefore define a generalized polarizability with an in-plane (α_{pi}) and out-of-plane value (α_{po}) of α_p.

With the larger set of parameters, the polarizability tensor takes on the more general form

$$\alpha_{ij}^b = \alpha_l \hat{R}_i \hat{R}_j + \alpha_{pi} \hat{S}_i \hat{S}_j + \alpha_{po} \hat{T}_i \hat{T}_j, \tag{5}$$

where $\hat{\mathbf{S}}$ is a unit vector pointing perpendicular to the bond in plane, and $\hat{\mathbf{T}}$ pointing perpendicular to the bond out of plane. [In the case of $\alpha_{pi}=\alpha_{po}$, Eq. (5) simplifies to Eq. (4) due to the relation $\hat{S}_i\hat{S}_j+\hat{T}_i\hat{T}_j=\delta_{ij}-\hat{R}_i\hat{R}_j$.] For the derivative tensor (of a single bond), we obtain

$$\begin{aligned}\frac{\partial \alpha_{ij}^b}{\partial u_{k\gamma}} = {} & \alpha_l' \hat{R}_i \hat{R}_j \hat{R}_k + \alpha_l[(\partial_k \hat{R}_i)\hat{R}_j + \hat{R}_i(\partial_k \hat{R}_j)] \\ & + \alpha_{pi}' \hat{S}_i \hat{S}_j \hat{R}_k + \alpha_{pi}[(\partial_k \hat{S}_i)\hat{S}_j + \hat{S}_i(\partial_k \hat{S}_j)] \\ & + \alpha_{po}' \hat{T}_i \hat{T}_j \hat{R}_k + \alpha_{po}[(\partial_k \hat{T}_i)\hat{T}_j + \hat{T}_i(\partial_k \hat{T}_j)]. \end{aligned} \tag{6}$$

The total derivative tensor $B_{ij}^{k\gamma}$ is then just the sum over all $\partial\alpha_{ij}^b/\partial u_{k\gamma}$ of all bonds of the system. The orientation of the plane at the position of a particular atom is thereby defined by the three nearest-neighbor atoms.

In order to determine the six parameters of our model, we perform *ab initio* calculations of the polarizability tensor α_{ij} of a unit cell of a single BN sheet[18,19] [see Fig. 1(a)]. The geometry of the system leads to the relations $\alpha_{xx}=\alpha_{yy}=(3/2)(\alpha_l+\alpha_{pi})$ and $\alpha_{zz}=3\alpha_{po}$ (with the z axis perpendicular to the sheet). Displacing atom 2 in the y direction yields the relation $\partial\alpha_{xx}/\partial u_{2y}=(3/4)(\alpha_l'+\alpha_{pi}')+(3/2)(\alpha_l+\alpha_{pi})/R$. Finally, by changing the geometry of the unit cell such that one bond is elongated while the other two bond lengths and all the bond angles are kept constant [see Fig. 1(b)], we extract the derivatives of the bond polarizabilities: $\alpha_l'=\alpha_{xx}'$, $\alpha_{pi}'=\alpha_{yy}'$, and $\alpha_{po}'=\alpha_{zz}'$. The resulting parameters are displayed in Table I and compared to the parameters we calculated for cubic BN and diamond. The longitudinal bond polarizability α_l is considerably larger than α_p which can be intuitively explained as a consequence of the "enhanced mobility" of the electrons along the bond. For the sheet, the perpendicular polarizabilities clearly display different values in the in-plane and out-of-plane directions. Without the added flexibility of different parameters, the bond-polarizability model would lead to inconsistencies in the description of α_{ij} and its derivatives. In the sheet, α_l is about twice as large as in cubic BN (*c*-BN) due to the additional contribution of the π electrons to the longitudinal polarizability. Comparison of *c*-BN with the isoelectronic diamond shows a slightly higher polarizability of the C–C bond.

As a first application of the generalized bond-polarizability model, we present in Fig. 2 the polarizability γ (per unit length) of different BNNTs.[20] For the polarizability along the tube axis (z-direction), the model [Eq. (5)] agrees almost perfectly with our *ab initio* calculations. The polarizability is proportional to the number of bonds in the unit cell, which is proportional to the tube radius. For the perpendicular direction, the model calculations overestimate the *ab initio* values considerably. This discrepancy demonstrates the importance of *depolarization effects* in the perpendicular direction: due to the inhomogeneity of the charge distribution in this direction, an external field induces local fields that counteract the external field and thereby reduce the overall polarizability. The size of this effect can be estimated from a simple model. Imagine a dielectric hollow cylinder of radius R (measured at the midpoint between the inner and outer walls) and thickness d. The dielectric constant in the tangential direction, $\epsilon_\parallel=(d+4\pi\beta_\parallel)/d$, is different from the dielectric constant in radial direction, $\epsilon_\perp=d/(d-4\pi\beta_\perp)$. Here, $\beta_\parallel$ and $\beta_\perp$ are the polarizabilities per unit area of the BN sheet, which are extracted from the bulk calculation.[19] The polarizability γ per unit length of the cylinder due to an external homogeneous electric field perpendicular to the tube axis is[21]

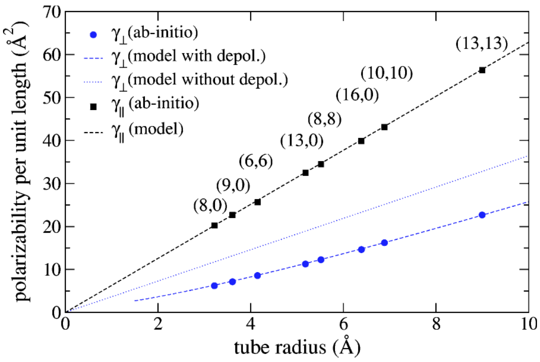

FIG. 2. Perpendicular ($\gamma_\perp$) and longitudinal ($\gamma_\parallel$) polarizabilities per unit length of different BN nanotubes: *ab initio* and our generalized bond-polarizability model. The influence of depolarization can be seen for $\gamma_\perp$.

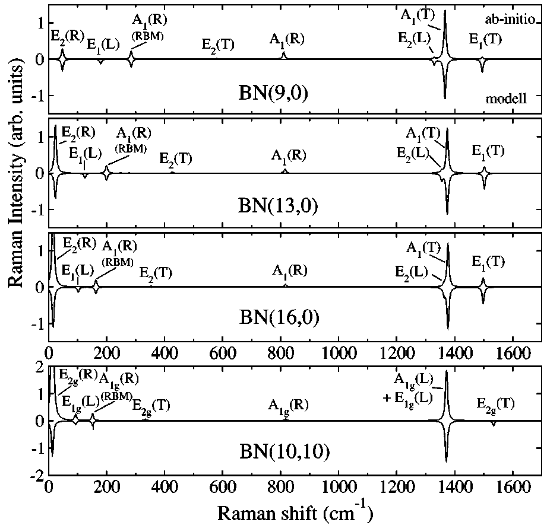

FIG. 3. Raman spectrum for different BN tubes: Comparison of *ab initio* calculations (positive axis) with the bond-polarization model (inverted axis). The symmetry assignment follows Ref. 23. The letters R, T, L denote the character of the corresponding phonon oscillation: radial, transverse, or longitudinal (see Ref. 10).

$$\gamma(R) = -\frac{1}{2}\left(R+\frac{d}{2}\right)^2 \frac{(\epsilon_\parallel\epsilon_\perp - 1)(1-\Theta^{2\nu})}{(\sqrt{\epsilon_\parallel\epsilon_\perp}-1)^2\Theta^{2\nu} - (\sqrt{\epsilon_\parallel\epsilon_\perp}+1)^2}, \quad (7)$$

with $\Theta=(R-d/2)/(R+d/2)$ and $\nu=\sqrt{\epsilon_\parallel/\epsilon_\perp}$. In the limit $R/d\rightarrow\infty$, the polarizability in Eq. (7) displays a linear dependence on the radius: $\gamma(R)\rightarrow\gamma_0(R)-\delta$, where $\gamma_0(R) = \pi(\beta_\parallel+\beta_\perp)R$. This corresponds to the polarizability without depolarization effects and coincides with the undamped model curve for $\gamma_\perp$ (dotted line in Fig. 2).

The depolarization effects are introduced into our model by multiplying the undamped model curve for the perpendicular polarizability with the "damping" factor $\Gamma(R) = \gamma(R)/\gamma_0(R)$. This factor depends on the cylinder thickness d. The value $d=3$ Å, which corresponds approximately to the full width of the charge density of a BN sheet, leads to an almost perfect agreement between model and *ab initio* calculations.[22]

To compute Raman intensities we make the further assumption

$$B_{ij}^{k\gamma} = \frac{\partial(\Gamma_{ij}\alpha_{ij})}{\partial u_{k\gamma}} \simeq \Gamma_{ij}\frac{\partial\alpha_{ij}}{\partial u_{k\gamma}}, \quad (8)$$

where $\partial\alpha_{ij}/\partial u_{k\gamma}$ is constructed according to Eq. (6). We assume here that to first order the atomic displacement does not change the depolarization. For $i=j=3$, i.e., for incoming and scattered light polarized along the tube axis, $\Gamma_{ij}=1$, otherwise $\Gamma_{ij}=\Gamma(R)$.

In Fig. 3 we present the *ab initio* and model Raman spectra for the (9,0), (13,0), and (16,0) zigzag BN nanotubes and a (10,10) armchair tube. The latter two have diameters (12.8 and 13.8 Å) in the range of experimentally produced BN tubes.[8,9] The spectra are averaged over the polarization of the incoming light and scattered light. We first discuss the spectra of the zigzag tubes. The peaks below 700 cm^{-1} are due to low-frequency phonon modes that are derived from the acoustic modes of the sheet and whose frequencies scale inversely proportional to the tube diameter [except for the $E_2(R)$ mode, which scales with the inverse square of the diameter].[10] The $E_2(R)$ mode gets quite intense with increasing tube diameter, but its frequency is so low that it will be hard to distinguish it from the strong Raleigh-scattering peak in experiments. The $E_1(L)$ peak has almost vanishing intensity in the *ab initio* spectrum and is overestimated in the model. The radial breathing mode (RBM) yields a clear peak that should be easily detectable in Raman measurements of BNNTs, just as in the case of CNTs. Both *ab initio* and model calculations yield a similar intensity for this peak. The high-frequency modes above 700 cm^{-1} are derived from the optical modes of the sheet and change weakly with diameter. The $A_1(R)$ mode at 810 cm^{-1} gives a small contribution that might be detectable. The intensity decreases, however, with increasing diameter. The model only yields a vanishingly small intensity for this peak. At 1370 cm^{-1} a clear signal is given by the $A_1(T)$ mode, which has very similar intensity both in model and *ab initio* calculations. The small side peak at slightly lower frequency is due to the $E_2(L)$ mode. The $E_1(T)$ peak at 1480 cm^{-1} is gaining intensity with increasing tube radius. The overall Raman spectrum for a (10,10) armchair tube exhibits similar trends.

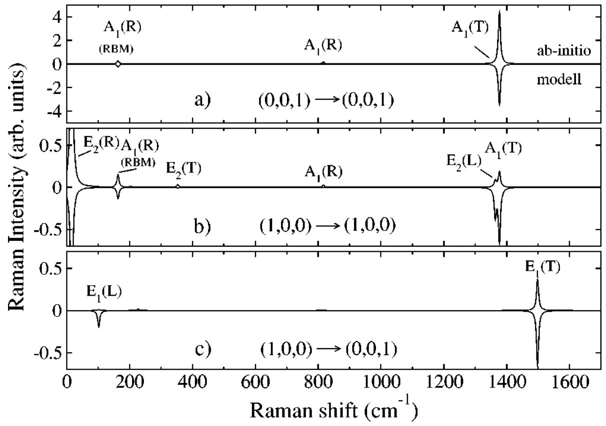

FIG. 4. Raman spectrum of a BN(16,0) tube for different light polarizations $\mathbf{e}_i\rightarrow\mathbf{e}_f$. The tube is oriented along (001).

In Fig. 4 we show for the (16,0) tube the dependence of the intensities on the light polarizations. If both $\mathbf{e}_i$ and $\mathbf{e}_f$ point along the tube axis [Fig. 4(a)], only the A_1 modes are visible and described well by the model (except the 810-cm^{-1} mode). This coincides with the finding that for the polarizability along the tube axis, depolarization does not play a role.[24] The E modes are only visible if at least one of $\mathbf{e}_i$ and $\mathbf{e}_f$ has a component perpendicular to the tube axis [Figs. 4(b) and 4(c)]. The bond-polarizability model reproduces these peaks, but tends to overestimate the E modes. The inclusion of depolarization effects is absolutely mandatory. Without depolarization, the model overestimates the Raman intensities for perpendicular polarization by about a factor of 15. The remaining discrepancies are mainly due to the assumption in Eq. (8).

In conclusion, we implemented the bond-polarizability model for BN nanotubes with parameters taken from *ab initio* calculations and under inclusion of depolarization effects. Going beyond previous models for graphitic systems, our calculations yield different parameters for the in-plane and out-of-plane perpendicular polarizabilities. Good agreement between model and *ab initio* calculations of the nonresonant Raman spectra of BN nanotubes is obtained for light polarization along the tube axis. For perpendicular polarization, the inclusion of depolarization effects leads to a reasonable agreement between model and *ab initio* spectra. The model is implemented for single-wall BN tubes but can be extended to multiwall tubes if the strength of the depolarization effects is modeled accordingly. A similar bond-polarizability model can also be developed for the nonresonant Raman spectra of semiconducting carbon NTs. However, due to the metallic behavior, a bond-polarizability model is not applicable to the graphene sheet. Consequently, the modeling of the polarizability of semiconducting tubes is very sensitive to the band structure,[25] in particular to the bandgap that depends on the radius and chirality of the tubes.

This work was supported by EU Network of Excellence NANOQUANTA, Grant No. NMP4-CT-2004-500198 and Spanish-MCyT. Calculations were performed at IDRIS (grant 051202) and CEPBA supercomputer centers.

---

*Permanent address: IEMN (CNRS-UMR 8520), Boîte Postale 60069, 59652 Villeneuve d'Ascq Cedex, France.

[1] *Light Scattering in Solids II*, edited by M. Cardona and G. Güntherodth (Springer-Verlag, Berlin, 1982).

[2] A. M. Rao, E. Richter, S. Bandow, B. Chase, P. C. Eklund, K. A. Williams, S. Fang, K. R. Subbaswamy, M. Menon, A. Thess, R. E. Smalley, G. Dresselhaus, and M. S. Dresselhaus, Science **275**, 187 (1997).

[3] A. M. Rao, A. Jorio, M. A. Pimenta, M. S. S. Dantas, R. Saito, G. Dresselhaus, and M. S. Dresselhaus, Phys. Rev. Lett. **84**, 1820 (2000).

[4] G. S. Duesberg, I. Loa, M. Burghard, K. Syassen, and S. Roth, Phys. Rev. Lett. **85**, 5436 (2000).

[5] R. Saito, T. Takeya, T. Kimura, G. Dresselhaus, and M. S. Dresselhaus, Phys. Rev. B **57**, 4145 (1998).

[6] R. Saito, G. Dresselhaus, and M. S. Dresselhaus, *Physical Properties of Carbon Nanotubes* (Imperial College Press, London, 1998).

[7] A. Rubio, J. L. Corkill, and M. L. Cohen, Phys. Rev. B **49**, 5081 (1994); X. Blase, A. Rubio, S. G. Louie, and M. L. Cohen, Europhys. Lett. **28**, 335 (1994).

[8] N. G. Chopra, J. Luyken, K. Cherry, V. H. Crespi, M. L. Cohen, S. G. Louie, and A. Zettl, Science **269**, 966 (1995).

[9] R. S. Lee, J. Gavillet, M. Lamy de la Chapelle, A. Loiseau, J.-L. Cochon, D. Pigache, J. Thibault, and F. Willaime, Phys. Rev. B **64**, 121405(R) (2001).

[10] L. Wirtz, A. Rubio, R. Arenal de la Concha, and A. Loiseau, Phys. Rev. B **68**, 045425 (2003); L. Wirtz and A. Rubio, IEEE Trans. Nanotechnol. **2**, 341 (2003).

[11] D. Sánchez-Portal and E. Hernández, Phys. Rev. B **66**, 235415 (2002).

[12] V. N. Popov, Phys. Rev. B **67**, 085408 (2003).

[13] S. Baroni, S. de Gironcoli, A. Dal Corso, and P. Giannozzi, Rev. Mod. Phys. **73**, 515 (2001).

[14] X. Gonze, J.-M. Beuken, R. Caracas, F. Detraux, M. Fuchs, G.-M. Rignanese, L. Sindic, M. Verstraete, G. Zerah, F. Jollet, M. Torrent, A. Roy, M. Mikami, Ph. Ghosez, J.-Y. Raty, and D. C. Allan, Comput. Mater. Sci. **25**, 478 (2002).

[15] M. Lazzeri and F. Mauri, Phys. Rev. Lett. **90**, 036401 (2003).

[16] M. V. Wolkenstein, C. R. Acad. Sci. URSS **30**, 791 (1941).

[17] P. Umari, A. Pasquarello, and A. Dal Corso, Phys. Rev. B **63**, 094305 (2001).

[18] We use a periodic supercell with an intersheet distance of 12 a.u. We use Troullier-Martins pseudopotentials. The two-dimensional Brillouin zone is sampled by a 12×12 Monckhorst-Pack grid. Local density approximation is used.

[19] The polarizability perpendicular to the sheet is calculated through the 1-dimensional Clausius-Mossotti relation $\alpha_\perp=\alpha_{zz}=(\Omega/4\pi)(\epsilon_{zz}-1)/\epsilon_{zz}$ while the parallel polarizability obeys the relation $\alpha_{xx}=(\Omega/4\pi)(\epsilon_{xx}-1)$. Ω is the unit-cell volume. We checked numerically that the thus-obtained α_{zz} and α_{xx} are independent of the intersheet distance. The polarizability per unit area, β, is $\beta=\alpha/A$, where A is the unit-cell area in the x-y plane.

[20] The perpendicular tube polarizability is extracted from the bulk dielectric tensor through the 2D Clausius-Mossotti relation $\alpha_\perp=(2\Omega/4\pi)(\epsilon_\perp-1)/(\epsilon_\perp+1)$. We checked numerically that the calculated $\alpha_\perp$ is approximately independent of the intertube distance.

[21] L. Henrard and Ph. Lambin, J. Phys. B **29**, 5127 (1996).

[22] The dependence on the empirical parameter d is weak: For the (16,0) tube, changing d from 2.2 to 4 Å gives rise to a change of 2% in the perpendicular polarizability.

[23] O. E. Alon, Phys. Rev. B **64**, 153408 (2001).

[24] A. G. Marinopoulos, L. Wirtz, A. Marini, V. Olevano, A. Rubio, and L. Reining, Appl. Phys. A **78**, 1157 (2004).

[25] L. X. Benedict, S. G. Louie, and M. L. Cohen, Phys. Rev. B **52**, 8541 (1995).

1.5.8 Experimental results on Raman and IR spectroscopy

Experimental Raman spectra

The essential test on the performance of Raman spectroscopy for the characterization of BN nanotubes is the comparison of the spectra of nanotube samples with the spectra of crystalline hBN. At high frequency, bulk hBN displays a single Raman line due to the E$_{2g}$ LO/TO mode. (This mode does not display an LO-TO splitting, contrary to the IR active E$_{1u}$ mode which has almost the same frequency). Originally, its frequency was measured at 1370 cm^{-1} [59]. However, later Nemanich et al.[60] showed that this mode depends sensitively on the domain size in polycrystalline samples: the finite domain size leads to an uncertainty for the phonon wave-vector q. This leads to a a superposition of the bulk E$_{2g}$ mode with q averaged over a region in the first Brillouin zone around Γ. Since the E$_{2g}$ LO-mode displays a strong overbending, the resulting Raman peak not only broadened but also shifted towards higher frequency[60]. Nemanich et al. extrapolated the value of the infinite crystal as 1366 cm^{-1}. Recently, the E$_{2g}$ LO/TO mode was measured at 1364 cm^{-1}[61]. The domain-size dependence of the Raman spectra needs to be taken into account when one analyzes the Raman spectra of nanotube raw-products that may contain both nanotubes and microcrystallites of hBN at the same time.

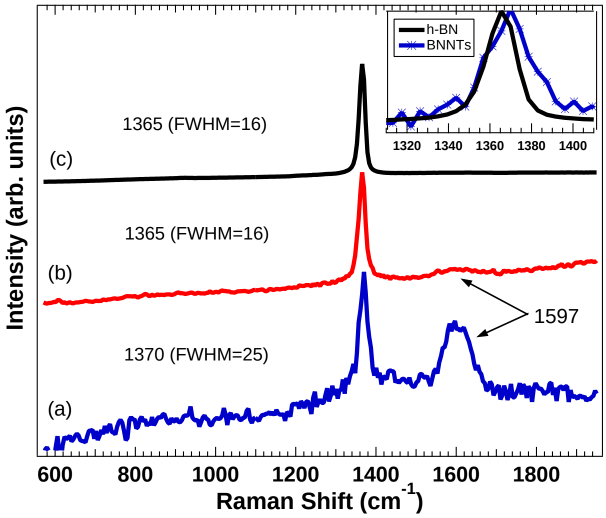

Figure 1.24: Raman spectra excited at 229 nm on (a) a BNNTs, (b) a particle of hBN in the raw product of BNNTs, (c) highly crystalline powder h-BN. The inset shows and enlargement and demonstrates the upshift of the dominant peak in the tubes as compared to bulk hBN. Figure reprinted from Ref. [22].

Before we discuss the measured Raman spectra of multi- and single-walled BN nanotubes, we would like to point out a further important detail in the theoretical calculations of frequencies of the E$_{2g}$ mode in bulk h-BN and of the E$_{2g}$ mode in the sheet: The value for the bulk is 3.8 cm^{-1} lower than the value for the sheet [22]. This lower frequency is related to an increase of the calculated in-plane lattice constant which is 4.718 a.u. for bulk h-BN and 4.714 a.u. for the single sheet. The difference stems from the - small but non-negligible - interaction of neighboring sheets in bulk h-BN. The interaction leads to a small elongation of the B-N bond-length and consequently a softening of the phonons.

The Raman spectra of multi-wall tubes (with 2-8 walls and an average outer diameter of 8 nm) were measured by Wu et al.[39] They measured the bulk E_{2g} peak at 1366 cm^{-1} (corresponding to the limit of infinite size crystallites) and found an upshift of 2.1 cm^{-1} with respect to this value for the BNNT sample. (Note that IR spectra on multi-walled tubes have also displayed an upshift of the E_{1u} mode with respect to the bulk value[53] (see below)). Wu et al. took the tube diameter as a measure for the "crystal size" and used the theory of Nemanich et al.[60] to explain the upshift of the Raman peak. It is not clear if this argument is admissible, since the phonon calculations for (single-wall) nanotubes show unanimously a softening of the dominant Raman peak with respect to the phonon value of the infinite sheet[54] [56] [12]. An alternative explanation may be given by the increased inter-layer distance and the non-commensurate stacking in multi-wall tubes. Both effects reduce the inter-layer interaction and may explain why the E_{2g} mode in multi-walled tubes displays a similar upshift as the isolated sheet.

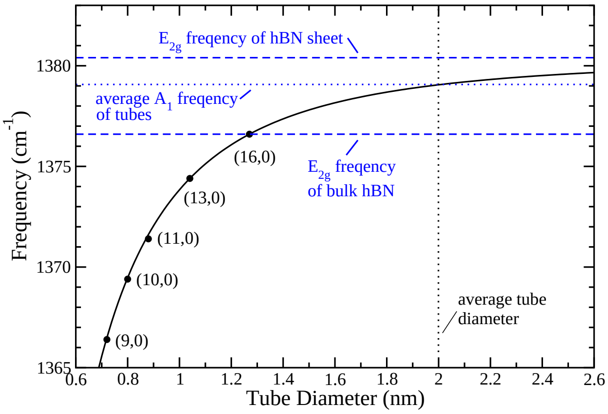

Figure 1.25: Calculated frequencies of the Raman active optical A_1 mode for different (n,0) zigzag BN nanotubes (symbols). The solid line is a fit (see text) that describes the convergence of the mode frequency with increasing tube diameter towards the value for the isolated sheet.

For single-walled nanotubes (with an average diameter of 2 nm), an upshift of 5 cm^{-1} with respect to the bulk E_{2g} frequency has been measured [22] (see Fig. 1.24. To understand this upshift, we compare with ab-initio calculations of the phonon frequencies of nanotubes and bulk h-BN. Fig. 1.25 shows the convergence of the A_1 mode in zigzag nanotubes towards the E_{2g} mode of the single sheet. A fit of the calculated tube frequencies as a function of the diameter d yields $\omega(d) = \omega_{E_{2g}}^{\text{sheet}} - 1268.3/d^{2.29}$ cm^{-1} (with d given in Å)[54]. This functional form is also displayed in Fig. 1.25. For the tubes with average diameter of 2 nm, the A_1 mode frequency is just 1.3 cm^{-1} below the value for the sheet and thus 2.5 cm^{-1} above the value of the bulk. While *ab-initio* calculations using DFT cannot reproduce properly the Van-der-Waals part of the interactions between the layers, they nevertheless give a qualitative indication of the origin of the Raman peak shift in single- and multi-wall tube samples (as already proven for the case of interlayer modes in hexagonal BN including exchange-correlation effects on the level of GW which includes the description of Van-der Waals interactions[62]).

IR spectra

IR spectroscopy on bulk hBN[59] yielded the TO E_{1u} mode at 1367 cm^{-1} and the LO E_{1u} mode at 1610 cm^{-1}. The latter one is shifted due to the coupling with the electric-field of the laser. Furthermore, the ZO A_{2u} mode (which also couples to the electric-field) was measured at 783 cm^{-1}.

Relatively little is known on the IR spectra of BN tubes. IR measurements of single-wall BN tubes have so far be impeded by the presence of boric-acid in the sample which dominated the IR absorption spectrum [22]. Experimental IR data is available, however, for samples of multiwalled BN tubes (2-10 walls, diameter: 30 ± 10 Å)[53]: Absorption peaks were measured at 800 cm^{-1} and at 1372 cm^{-1} with a shoulder at 1540 cm^{-1}. At the same time, for polycrystalline h-BN, they measured peaks at 811 cm^{-1} and at 1377 cm^{-1} with a shoulder at 1514 cm^{-1}. The interpretation of both results is not straight-forward, because in finite-size samples of polar materials, the induced electric field depends not only on the direction of light propagation but also on the boundary conditions at the surface of the sample[72], i.e., the sample geometry. Furthermore, the dielectric properties of the surrounding medium (KBr pellets) can play a role. Both effects strongly influence the position of the A_{2u} mode and the LO E_{1u} mode. The upshift of the TO E_{1u} mode in the polycrystalline sample with respect to the bulk sample is due to the finite size of the crystal domains[60]. The upshift by 5 cm^{-1} of the TO E_{1u} mode in the multi-wall tubes with respect to the bulk stems probably from the increased inter-wall distance in multi-wall tubes as compared to the bulk phase[53]. This upshift corresponds to a similar upshift (of 2.1 cm^{-1}) in the Raman spectra of BN multi-wall nanotubes[39] (see above).

1.6 Summary and conclusions

In this chapter we have reviewed the spectroscopic properties of BN nanotubes covering the basic principles of electronic and vibrational excitations from the theoretical view-point. Comparing the electronic properties of BN and C nanotubes, the most striking difference between the two classes of tubes is the constancy of the quasi-particle gap for BN tubes. The band-gap constancy may be of importance for technological applications because samples containing many different sizes could be grown with predictable electronic properties. Applications as field-emission devices have been envisioned and a first prototype field-effect transistor has been constructed[4].

The optical spectra of BN nanotubes - as well as the spectrum of bulk hBN and of a single sheet of BN - are dominated by a strongly bound exciton that collects most of the oscillator strength in the spectrum. The binding energy of this exciton increases strongly as the dimensionality is reduced from the 3-D bulk over the 2-D sheet to the 1-D tubes. At the same time, however, the quasi-particle gap increases and the resulting spectra thus display an almost constant "optical gap". Due to the similarity in the spectra of the tubes and bulk BN we expect the tubes to exhibit strong ultraviolet lasing behavior as already observed for bulk BN[5]. The fact that this luminescence response would be rather insensitive to tube diameter and chirality makes the BN tubes ideal candidates for optical devices in the UV regime while

---

[72] E. Balan, A.M. Saitta, F. Mauri, and G. Calas, American Mineralogist **86**, 1321 (2001).

carbon nanotubes are in the infrared regime. The photoluminescence quantum yield of BN tubes should surpass the efficiency of carbon. Furthermore we have shown how defects control the luminescence and the impact of an external electric field perpendicular to the tube axis: While the gap decreases as a function of the electric field strength, the optical spectra of BN nanotubes are quite robust to the application of external fields. On the contrary, an external field affects the defect energy levels due to impurities. These defects gives rise to strong luminescence withing the gap, in particular in the visible region as well as modification of the shape of the main absorption peak. Therefore an external electric field can be used as tool to discriminate the photoemission due to exciton recombination in pure systems with respect to the one due to defects. BN nanotubes may thus be very good candidates for tunable nanoscale optoelectronic devices in the UV regime and below.

The flexibility of composite nanotubes during bending in a wide range of practical conditions shows substantial promise for structural, fiber applications (the “ultimate” lightweight-high-strength flexible and quite inert fiber) and nanotube-reinforced materials. This is due to the remarkable flexibility of the hexagonal network, which resists bond breaking and bond switching up to very high strain values. The lattice dynamics of BN tubes is similar to that of carbon nanotubes. The most important difference is the polarity of the system which leads to softer bonds and lower phonon frequencies. Furthermore, the lower symmetry of BN tubes gives rise to a higher number of Raman- and IR-active modes than in C tubes. As in the case of carbon nanotubes, the lattice dynamics of BN nanotubes can be explained to a large extent by the zonefolding method. The strong overbending of the LO-branch of the single sheet is responsible for the strongly non-monotonic diameter scaling of the transverse high-frequency modes in the tubes. Combined study of BN tubes by Raman and IR spectroscopy can serve to distinguish armchair tubes, where IR and Raman-active modes are disjoint, from chiral and zigzag tubes, where the IR-active modes are a subset of the Raman active modes. In particular, the radial breathing mode is both Raman and IR active for chiral and zigzag tubes but only Raman active for armchair nanotubes.

Improvements in the synthesis of BN nanotubes and their unique electronic properties (luminescence, inertness, piezoelectricity, field emission, robustness, etc) make them ideal candidates to confront - together with carbon nanotubes - the future of real active components in nanoelectronic devices.

Chapter 2

Excitations in Graphene and Graphite

2.1 Introduction

Since graphene, i.e., a single layer of graphite, is the 2-dimensional building block for 3-dimensional graphite and for 1-D nanotubes, it has for a long time attracted the interest of theorists. Recently, it has been demonstrated that single layers of graphene can indeed be produced and can be used to build ambipolar transistors with a high charge carrier mobility[1]. Furthermore, the linear dispersion around the K-point of the first Brillouin zone has interesting consequences for magneto-transport experiments such as a half-integer quantum-Hall effect.[2]

2.2 The phonon dispersion of graphite

While the phonon dispersion relations of most materials are very well known and routinely calculated by means of density-functional perturbation theory[3], the phonon dispersion of graphite has been under debate until very recently. Even though ab-initio calculations had been performed [4] [5], the experimentalists of the graphite and nanotube communities continued to use semi-empirical models fitted to selected experimental data on the phonon dispersions. Fig. 2.1 demonstrates that the existing 4th-nearest-neighbor force-constant (4NNFC) fits[6] [7] and valence-force field fits[8] [9] strongly deviated from each other and from ab-initio calculations.

In Ref. [17] we have reviewed the experimental data that existed in 2004 and compared with both ab-initio and semi-empirical phonon dispersion relations. Fig. 2.2 demonstrates that

---

[1] K.S. Novoselov et al., Science **306** 666 (2004).

[2] K.S. Novoselov et al., Nature **438**, 197 (2005); Y. Zhang et al., Nature **438**, 201 (2005).

[3] S. Baroni, S. de Gironcoli, A. Dal Corso and P. Giannozzi, Rev. Mod. Phys. **73**, 515 (2001).

[4] G. Kresse, J. Furthmüller, and J. Hafner, Europhys. Lett. **32**, 729 (1995).

[5] P. Pavone, R. Bauer, K. Karch, O. Schütt, S. Vent, W. Windl, D. Strauch, S. Baroni, and S. de Gironcoli, Physica B **219 & 220**, 439 (1996).

[6] R. A. Jishi, L. Venkataraman, M. S. Dresselhaus, and G. Dresselhaus, Chem. Phys. Lett. **209**, 77 (1993).

[7] A. Grüneis, R. Saito, T. Kimura, L. C. Cancado, M. A. Pimenta, A. Jorio, A. G. Souza Filho, G. Dresselhaus, and M. S. Dresselhaus, Phys. Rev. B **65**, 155405 (2002).

[8] T. Aizawa, R. Souda, S. Otani, Y. Ishizawa, and C. Oshima, Phys. Rev. B **42**, 11469 (1990).

[9] S. Siebentritt, R. Pues, K-H. Rieder, and A. M. Shikin, Phys. Rev. B **55**, 7927 (1997).

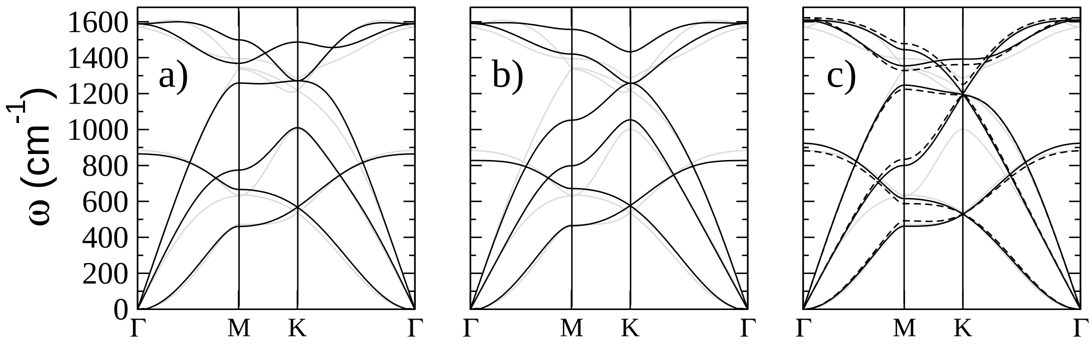

Figure 2.1: Semi-empirical fits of the phonon dispersion of graphene: a) 4NNFC fit[6], 4NNFC fit[7], VFF fit[8] (solid line) and[9] (dashed line). Comparison with ab-initio calculation [17] (grey lines).

ab-initio calculations (here we show a curve obtained within DFT-GGA) describe quite well the core of the experimental data with one notable exception that will be discussed below.

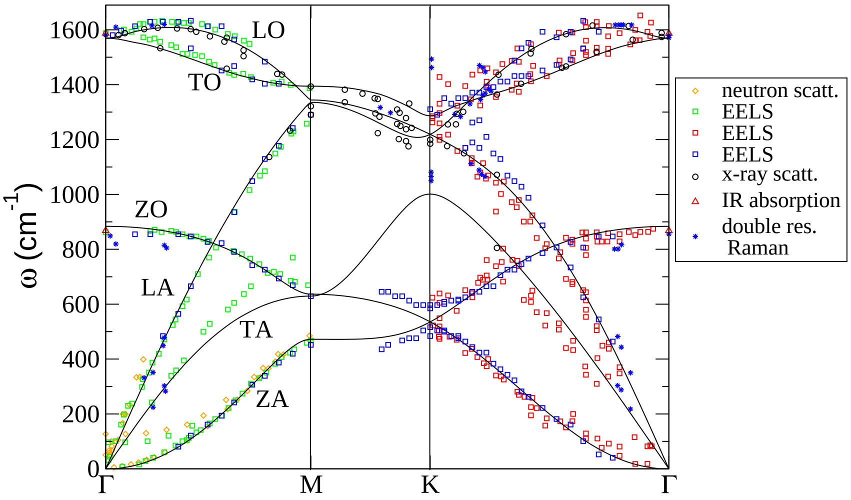

Figure 2.2: Comparison of ab-initio calculations (solid lines) with experimental data (symbols) [17].

Since the semi-empirical approaches for the phonons were widely used by the nanotube community, we have performed in Ref. [17] a fitting of the models to the ab-initio calculations. The valence-force field model of Aizawa et al.[8] parameterizes the inter-atomic forces quite intuitively in terms of spring constants for bond-stretching, bond-bending and bond-torsion. However, the restriction to only 5 parameters poses limitations to the quantitative validity of the model. The 4NNFC model of Dresselhaus et al.[6] contains 12 free parameters. They restricted the model to diagonal force constants, i.e., displacement of an atom parallel/perpendicular to the line that connects the atom to its nth neighbor causes only a parallel/perpendicular force on the neighbor. Fig 2.3 c) demonstrates that the diagonal approximation breaks down for the second-nearest neighbor interaction: The angular spring-constant γ_1 which tries to preserve the 120 degree bonding angle at atom 1 gives rise to a horizontal and vertical force component acting on atom 2 as atom 0 is displaced in the direction towards atom 2. In Fig 2.3 we show our 4NNFC fit with (a) and without (b) inclusion of the off-diagonal force constants for the second-nearest neighbor interaction. The off-diagonal term considerably improves the fit and leads to and almost perfect agreement with the ab-initio calculations for the acoustic modes. We also obtain a general good agreement for the optical modes. Two discrepancies remain, however, and can only be solved through the inclusion of long-range force constants: The overbending of the LO mode at Γ and the strong dip of the highest optical branch around K.

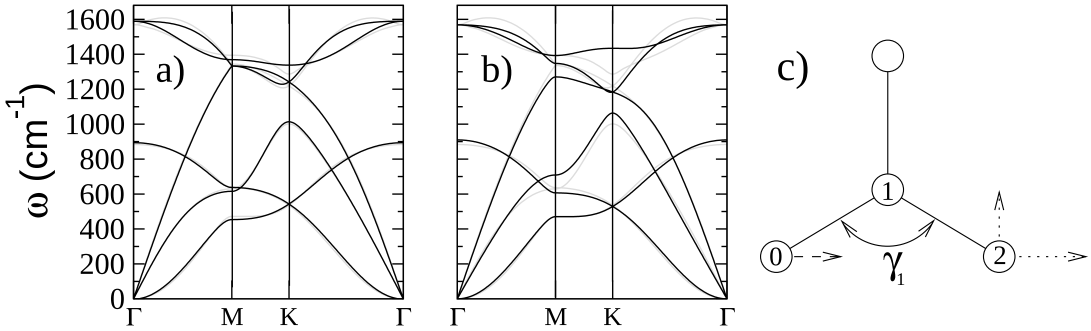

Figure 2.3: 4NNFC fit (black solid lines) to the ab-initio phonon dispersion of graphene (grey lines), a) including off-diagonal force constants, b) excluding off-diagonal force constants. c.) Demonstration of the off-diagonal force-constants for the second-nearest neighbor interaction in graphene.

2.3 Double resonant Raman scattering of single- and few-layer graphene

Raman spectroscopy has been a frequently used tool for the characterization of graphite and of carbon nanotubes. The typical spectrum of graphite displays three prominent peaks. The peak around 1582 cm^{-1}, commonly called the G line, is due to 1st order inelastic scattering of a photon, exciting a Raman active E_{2g} phonon (in-plane optical mode), at the Γ point. The position of the G line is independent of the laser energy. In contrast, the D line around 1350 cm^{-1} shifts to higher frequencies with increasing incident laser excitation energies. Furthermore, its relative signal strength (compared to the G line) depends strongly on the amount of disorder in the graphitic material. The associated overtone 2D around 2700 cm^{-1} is present even in the absence of a D signal.

The different experimental findings related to the dispersive D and 2D bands were explained by Thomsen and Reich within the framework of double resonant Raman scattering.[10] We recall the mechanism in Fig. 2.4: In the ordinary (single-resonant) Raman mechanism, a photon is absorbed through vertical excitation of an electron. The electron falls vertically back to the ground state through the emission/absorption of a phonon with zero wave-vector and emission of a photon with lower/higher energy than the initial photon. The energy shift thus corresponds directly to the energy of the zone-center phonon which has E_{2g} symmetry in the

---

[10] S. Reich and C. Thomsen, Phil. Trans. R. Soc. Lond. A **362**, 2271 (2004).

case of graphene and graphite. Due to the linear crossing of the π bands around the high symmetry point K, this process is possible in the whole infrared and visible range of light. Since both excitation and de-excitation of the electron are vertical, it is always the zone-center phonon that is excited. Consequently, the Raman peak position does not depend on the incoming laser light frequency and is always located at 1582 cm^{-1}.

An example for a double-resonant process is depicted in Fig. 2.4 b): an electron is excited vertically from A to B by the incoming photon. It is then scattered elastically through the influence of a defect to another point (C) in the band structure of graphite. The transition between B and C is "horizontal" because no energy is lost during the elastic collision. Since the intensity of the corresponding Raman peak depends on the presence of defects (or disorder), it has been named the D line. The electron can recombine with the hole at A through a non-vertical transition, i.e., by emitting a phonon with the corresponding wave-vector difference $\mathbf{q}$. If B and C are located on the cones around two inequivalent high symmetry points K and K', the excited phonon is on the highest optical branch (HOB) along the high-symmetry line K $\rightarrow$ M and has a frequency around 1350 cm^{-1}. A change of the incoming photon frequency changes the phonon momentum from $\mathbf{q}$ to $\mathbf{q}'$ and thus its frequency (see Fig. 2.4 c). The D-line thus disperses as a function of the incoming laser energy. It can be easily verified from Fig. 2.4 that the dispersion is proportional to the slope of the HOB around K and inversely proportional to the slope of the electronic bands around K. The 2D line is caused by the

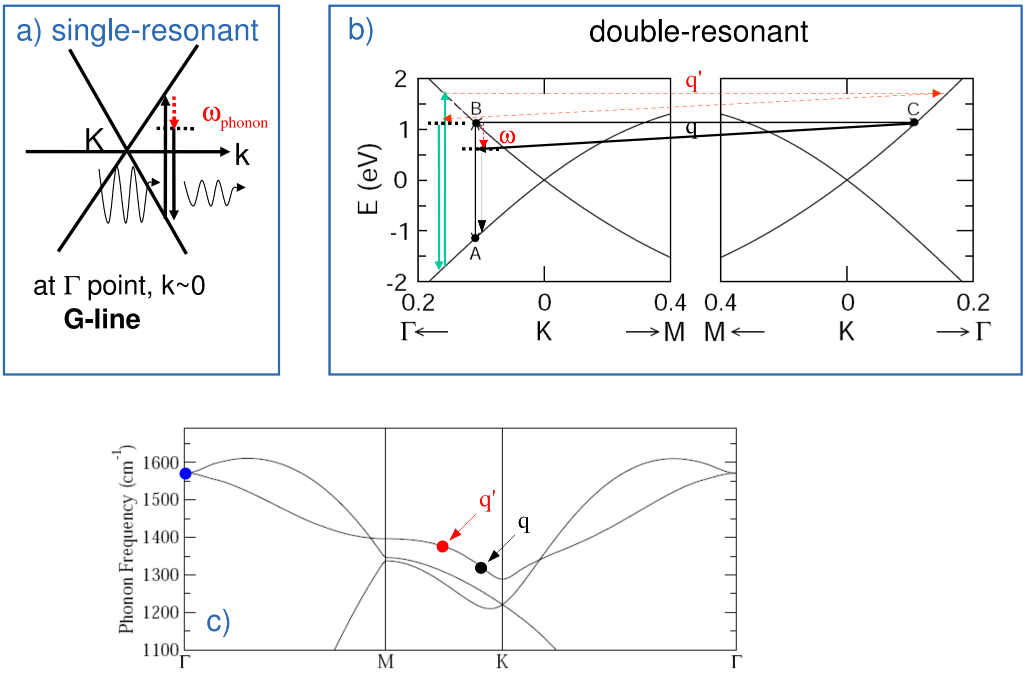

Figure 2.4: Scheme of the resonant Raman model: a) Single-resonant Raman scattering due to vertical electron excitation and de-excitation near the linear crossing of the π bands at K; b) double-resonant Raman scattering involving non-vertical electronic transitions; c) high-frequency phonon mode dispersion of graphene. The circles mark the phonons that are excited in the single and double-resonant processes.

emission (or absorption) of two phonons with finite momentum $\mathbf{q}$. In the picture of Fig. 2.4 b) this means that the defect mediated horizontal transition between B and C is replaced by an (almost horizontal) transition involving the emission of a phonon. The mechanism is independent of the presence of defects which explain why the 2D line is visible also in very pure graphite/graphene. The 2D line is located around 2700 cm^{-1}.

In the original paper on the double-resonant Raman effect[11] good quantitative agreement with the experimentally measured D-line dispersion of about 50 cm^{-1}/eV was claimed. However, we found during our work on the Raman spectra of single and multi-layer graphene [23] that the double-resonant Raman model underestimates the experimental D-line dispersion by about a factor of 2 if one uses standard ab-initio calculations of the electronic band structure and phonon dispersion. This discrepancy could be due to
(i) an overestimation of the Fermi velocity, i.e., the slope of the electronic π bands around K by a factor of 2,
(ii) an underestimation of the slope of the highest optical phonon branch around K by factor of 2, or
(iii) a failure of the double-resonant Raman model (e.g., the neglect of electron-electron and electron-hole correlation).
In section 2.6, we will show that option (i) can be ruled out since evaluation of the quasi-particle band-structure on the level of the GW-approximation renders renders an even higher value for the Fermi velocity than standard DFT-LDA calculations. We checked for the importance of electron-hole interaction by calculating the optical absorption spectrum of graphite with the Bethe-Salpeter equation. We found a slight red-shift of the spectrum (which almost cancels the blue-shift of the spectrum due to electron-electron correlation), but very weak mixing between different electron-hole pairs. Thus option (iii) could be ruled out as well. In section 2.4, we will show that it is indeed a failure of standard DFT calculations for phonons in graphite that lead to the observed discrepancy between measured and calculated D-line dispersion.

In collaboration with the group of K. Ensslin at ETH Zürich, we have investigated the differences in the Raman spectra of graphite, single-layer graphene, and multi-layer graphene [23,25,28]. The most prominent difference between the spectra of the single and the double-layer is the width of the 2D line which splits into different sub-peaks for the double-layer. For the interpretation of the splitting[12], we used the double-resonant Raman model, taking into account the splitting of the electronic π-bands as one goes from the single layer to the double layer of graphene. (See Fig. 5 of Ref. [23] which is reprinted on the following pages.). The use of ab-initio electronic bands and phonon dispersion enabled us to quantitatively explain the splitting of the 2D line, but the amount of the splitting was underestimated by a factor of 2. As in the case of the D-line dispersion, we know now that this factor of 2 can be explained, if the phonon dispersion of the highest optical branch around K is calculated including the effects of electron-electron correlation (see section 2.4).

---

[11] C. Thomsen and S. Reich, Phys. Rev. Lett. **85**, 5214 (2000).

[12] The interpretation was motivated by A.C. Ferrari, J.C. Meyer, V. Scardaci, C. Casiraghi, M. Lazzeri, F. Mauri, S. Piscanec, D. Jiang, K.S. Novoselov, S. Roth, and A.K. Geim, Phys. Rev. Lett. **97**, 187401 (2006).

NANO
LETTERS

2007
Vol. 7, No. 2
238−242

Spatially Resolved Raman Spectroscopy of Single- and Few-Layer Graphene

D. Graf,*,† F. Molitor,† K. Ensslin,† C. Stampfer,‡ A. Jungen,‡ C. Hierold,‡ and L. Wirtz§

Solid State Physics Laboratory, ETH Zurich, 8093 Zurich, Switzerland, Micro and Nanosystems, ETH Zurich, 8092 Zurich, Switzerland, and Institute for Electronics, Microelectronics, and Nanotechnology (IEMN), CNRS-UMR 8520, B.P. 60069, 59652 Villeneuve d'Ascq Cedex, France

Received July 21, 2006; Revised Manuscript Received October 7, 2006

ABSTRACT

We present Raman spectroscopy measurements on single- and few-layer graphene flakes. By using a scanning confocal approach, we collect spectral data with spatial resolution, which allows us to directly compare Raman images with scanning force micrographs. Single-layer graphene can be distinguished from double- and few-layer by the width of the D′ line: the single peak for single-layer graphene splits into different peaks for the double-layer. These findings are explained using the double-resonant Raman model based on ab initio calculations of the electronic structure and of the phonon dispersion. We investigate the D line intensity and find no defects within the flake. A finite D line response originating from the edges can be attributed either to defects or to the breakdown of translational symmetry.

The interest in graphite has been revived in the last two decades with the advent of fullerenes[1] and carbon nanotubes.[2] However, only recently, single- and few-layer graphene could be transferred to a substrate.[3] Transport measurements revealed a highly tunable two-dimensional electron−hole gas with a linear energy dispersion around the Fermi energy embedded in a solid-state environment.[4,5] Going to few-layer graphene, however, disturbs this unique system in such a way that the usual parabolic energy dispersion is recovered. The large structural anisotropy makes few-layer graphene therefore a promising candidate to study the rich physics at the crossover from bulk to purely two-dimensional systems. Turning on the weak interlayer coupling while stacking a second layer onto a graphene sheet leads to a branching of the electronic bands and the phonon dispersion at the K point. Double-resonant Raman scattering,[6] which depends on electronic and vibrational properties, turns out to be an ingenious tool to probe the lifting of that specific degeneracy.

We report on Raman mapping of single- and few-layer graphene flakes resting on a silicon oxide substrate. Lateral resolution of 400 nm allows one to address neighboring sections with various layers of graphene down to a single graphene sheet, previously determined with the scanning force microscope (SFM). We find that the integrated G line signal is directly correlated with the thickness of the graphitic flake and is shifted upward in frequency for double- and single-layer graphene compared to that of bulk graphite. The mapping of the peak width of the D′ line shows a strong contrast between single- and few-layer graphene. Such a pronounced sensitivity to the transition to the very last layer offers an optical and nondestructive method to unambiguously detect single-layer graphene. In addition, we locally resolve the structural quality of the flake by investigating the D band, which is related to elastic backscattering. The map of the integrated D line signal of a graphitic flake with double- and single-layer sections shows that the inner part of the flake is quasi-defect-free, whereas edges and steps serve as scatterers. Finally, we calculate the splitting of the D′ line as a function of the number of graphene layers by following the recent work of Ferrari et al.,[7] who explained the splitting within the double-resonant Raman model.[6] The comparison between experimental data and theory confirms the qualitative validity of the double-resonant Raman model but demonstrates quantitative differences between theory and experiment. In particular, the model, when based on first-principles calculations, predicts a much smaller splitting of the peaks.

The graphite films were prepared by mechanical exfoliation of highly oriented pyrolytic graphite (HOPG) and subsequent transfer to a highly doped Si wafer with a 300 nm SiO_2 (atomic oxidation process) cap layer.[3,8] The combination of optical microscopy using phase contrast and SFM makes it possible to locate flakes with various thicknesses down to a monolayer with lateral extensions in the micrometer range. The Raman spectra were acquired using

---

* Corresponding author. E-mail: grafdavy@phys.ethz.ch.
† Solid State Physics Laboratory, ETH Zurich.
‡ Micro and Nanosystems, ETH Zurich.
§ Institute for Electronics, Microelectronics, and Nanotechnology (IEMN).

10.1021/nl061702a CCC: $37.00

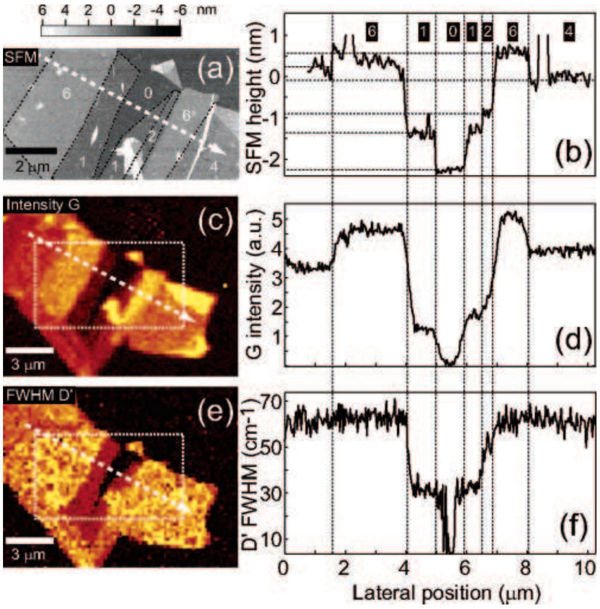

Figure 1. (a,b) SFM micrograph and cross-sectional plot (indicated with the white dashed arrow; lateral average over 400 nm) of a few-layer graphene flake with central sections down to a single layer. Raman maps (dashed square corresponding to the SFM image in (a)) showing (c) the integrated intensity of the G line and (e) the fwhm of the D′ line. The related cross sections (d,f) are aligned (vertical dashed lines) with the height trace.

a laser excitation of 532 nm (2.33 eV) delivered through a single-mode optical fiber, whose spot size is limited by diffraction. Using a long working distance focusing lens with a numerical aperture NA = 0.80, we obtained a spot size of about 400 nm. With a very low incident power of 4−7 μW, heating effects can be neglected.

The Raman spectrum of graphite has four prominent peaks (Figure 3: for a recent review, see ref 9). The peak around 1582 cm^{-1}, commonly called the G line, is caused by the Raman active E_{2g} phonon (in-plane optical mode), close to the Γ point. The D line around 1350 cm^{-1} exhibits two remarkable features: its position shifts to higher frequencies with increasing incident laser excitation energies[10] and its relative signal strength (compared to the G line) depends strongly on the amount of disorder in the graphitic material.[10,11] The associated overtone D′ around 2700 cm^{-1} is pronounced even in the absence of a D signal. Finally, the overtone of the G line, the G′ line, is located at 3248 cm^{-1}, which is more than twice the energy of the G line. The different experimental findings related to the dispersive D, D′ bands could be explained by Thomsen and Reich within the framework of double resonant Raman scattering,[6] which was extended to other phonon branches by Saito et al.[12] The electronic and vibrational properties of graphite are dominated by the sp^2 nature of the strong intraplane covalent bonds. Raman spectra for multiple graphene layers can be compared qualitatively and quantitatively while investigating flakes with sections of various thicknesses. In Figure 1a, the SFM micrograph of a graphite flake with different layers is presented: the bare SiO_2 (indicated by “0”) is surrounded by single-layer sections with steps of up to two, four, and six layers. The different step heights are clearly depicted in Figure 1b, where a cross section of Figure 1a (see white dashed arrow) is shown. By scanning the flake and collecting for each spot the complete Raman spectrum, we can subsequently filter specific spectral data for a spatially resolved data point and construct false-color 2D plots. In Figure 1c, the intensity of the G peak is integrated from 1537 to 1622 cm^{-1}. We find a remarkable correlation with the SFM graph: brighter regions correspond to thicker sections. The cross section in Figure 1d shows a steplike behavior, perfectly correlated with the topographical changes shown in Figure 1b. In Figure 1e, we plot the fwhm (full width at half-maximum) of the D′ line. It shows the narrowing at the transition to a single-layer (see, e.g., Figure 3) and gives an evident contrast between single- and few-layer graphene sections. The two discrete levels in the fwhm of the D′ line shown in Figure 1f related to a single layer (∼30 cm^{-1}) and two and more layers (∼60 cm^{-1}) suggest that the width of the D′ line can be used as a detector for single-layer graphene. Raman spectroscopy can therefore be used to count the layers of a thin graphite stack and to discriminate between single and double layers. Combined with the double-resonant Raman scattering mechanism, an optical setup using light in the visible range turns out to be an alternative to scanning force microscopy, which requires stacking folds as height references.

Transport measurements show that the quality of the finite graphitic flakes on the silicon oxide matrix obtained with the technique explained above is remarkable: electronic mobilities up to 15 000 $\mathrm{cm}^2\,(\mathrm{Vs})^{-1}$ were estimated from transport experiments.[4,5] We point out also that the Raman spectroscopy reveals quasi-defect-free graphitic sheets via the absence of a D band signal. First experiments have related the intensity of the D band to the structural coherence of the graphite material. In fact, it is inversely proportional to the crystallite grain size.[11] The appearance of the D band can, however, be related to the occurrence of defects and disorder in general, as shown in experiments with boron-doped and electrochemically oxidized HOPG.[13] With micro-Raman mapping, we are able to localize the spatial origin of the defects, which can have important consequences for the electronic properties.[14] From cross-correlating the SFM micrograph in Figure 2a with the Raman map of the integrated D line (1300−1383 cm^{-1}) intensity in Figure 2c, we infer directly that the edges of the flake and also the borderline between sections of different heights contribute to the D band signal, whereas the inner parts of the flakes do not. This is somewhat surprising because, for thinner flakes, the influence of a nearby substrate on the structural quality should be increasingly important. In the cross-section in Figure 2d, we see clearly that the D line intensity is maximal at the section boundaries, which can be assigned to translational symmetry breaking or to defects. However, we want to emphasize that the D line is still 1 order of magnitude smaller than the G line. In Figure 2e, spatially averaged D mode spectra from the two steps shown in Figure 2d are presented. The frequency fits well into the linear dispersion relation of peak shift and excitation energy found

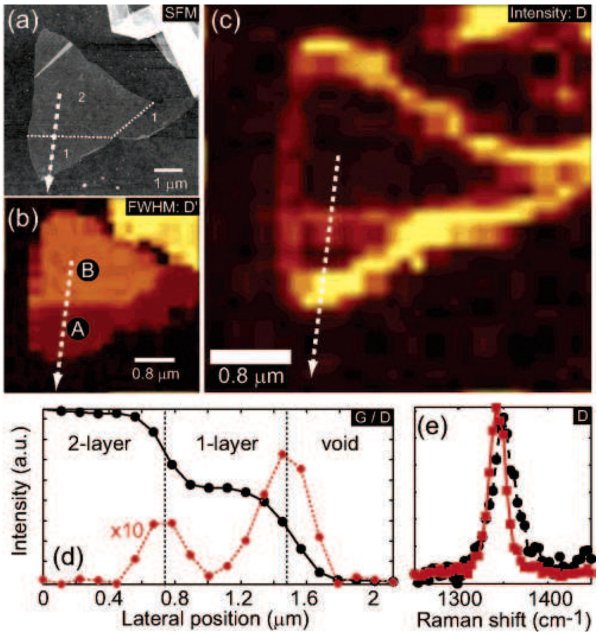

Figure 2. (a) SFM micrograph of a graphitic flake consisting of one double- and two single-layer sections (white dashed line along the boundaries), highlighted in the Raman map (b) showing the fwhm of the D′ line. (c) Raman mapping of the integrated intensity of the D line: A strong signal is detected along the edge of the flake and at the steps from double- to single-layer sections. (d) Raman cross section (white dashed arrow in (c)): staircase behavior of the integrated intensity of the G peak (solid line) and pronounced peaks at the steps for the integrated intensity of the D line (dashed line). (e) Spatially averaged D peak for the crossover from double to single layer (disk, dashed line) and from single layer to the SiO_2 substrate (square, solid line).

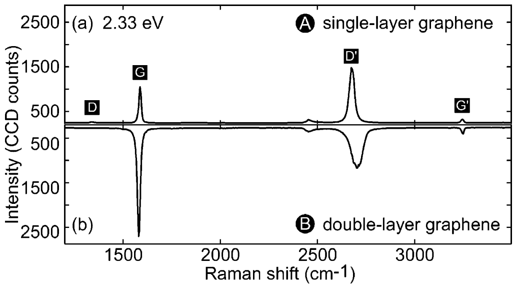

Figure 3. Raman spectra of (a) single- and (b) double-layer graphene (collected at spots A and B, see Figure 2b).

in earlier experiments.[10] In addition, we find that the peak is narrower and downshifted at the edge of the single layer, while it is somewhat broader and displays a shoulder at the crossover from the double to the single layer.

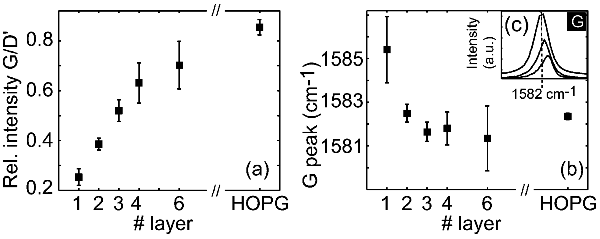

Figure 4. (a) Plot of the ratio of the integrated intensities of the G and D′ peak vs number of stacked layers (average value and standard deviation). (b) G line frequency vs number of stacked layers (average value and standard deviation). (c) G peak for HOPG (upper peak), double- (middle peak), and single-layer (lower peak) graphene. The vertical dashed line indicates the reference value for bulk graphite.

In parts a and b of Figure 3, we compare the Raman spectra of the double- and single-layer graphene shown in Figure 2b and labeled with A and B. The Raman signal is significantly altered when peeling off the penultimate layer: the G peak decreases strongly in intensity and shifts toward higher wave numbers. In connection with Figure 1b, we already stated that the integrated G line signal is monotonically increasing with increasing flake thickness. To compare data of different flakes and measurement runs, we turn our attention to the ratio of the integrated intensities of the G and D′ line, plotted in Figure 4a. Most of the changes can be attributed to the decrease of the G line because the spectral weight of the D′ band changes only slightly. The intensity ratio increases almost linearly from one to four layers. In Figure 4b, the dependence of the G peak position on the layer number is investigated. Spectral data of various sections on different flakes were averaged. The frequency shifts toward higher wave numbers at the crossover to the double- and especially to the single-layer graphene. However, in the case of single-layer graphene, it is accompanied by an important statistical spread of the collected data. In Figure 4c, representative G peak spectra for single-, double-layer graphene, and HOPG are presented. It is important to note that, in contrast to the G line, the corresponding overtone band, the G′ line, does not change its spectral position as a function of the number of layers.

The most prominent difference in the spectra of single-layer, few-layer, and bulk graphite lies in the D′ line: the integrated intensity of the D′ line stays almost constant, even though it narrows to a single peak at a lower wave number at the crossover to a single layer (Figure 3). The width of the D′ peak or, at high resolution, its splitting into different subpeaks (Figure 5) is explained in the following in the framework of the double-resonant Raman model.[6,7] The model explains the D′ line in the following way (see Figure 6a): an electron is vertically excited from point A in the π band to point B in the π^* band by absorbing a photon. The excited electron is inelastically scattered to point C by emission of a phonon with wave vector q. Because the energy of this phonon ($\approx$ 150 meV) is small compared with the photon energy of 2.33 eV, we have drawn the line horizontally for simplicity. Inelastic backscattering to the vicinity of point A by emission of another phonon with wave vector $\approx q$ and electron−hole recombination leads to emission of a photon with an energy about 300 meV less than the energy of the incident photon. In principle, two other double-resonant Raman processes, involving the phonons q' and q'', are possible as well. However, it was argued in ref 7 that their weight is very low.[15]

In Figure 6, we compare the electronic band structure of the single layer with the ones of the double layer and of bulk graphite. All three dispersion relations were calculated

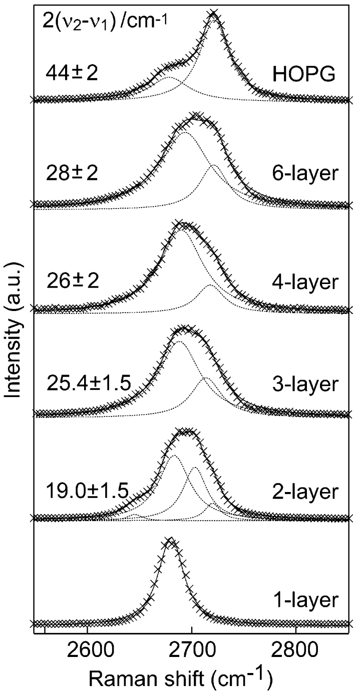

Figure 5. D′ peaks for an increasing number of graphene layers along with HOPG as a bulk reference. The dashed lines show the Lorentzian peaks used to fit the data, the solid lines are the fitted results. The single peak position for the single-layer graphene is at 2678.8 ± 1.0 cm^{-1}. The peak position of the two innermost peaks for double-layer graphene are 2683.0 ± 1.5 and 2701.8 ± 1.0 cm^{-1}. On the left, the value for the splitting from double-layer graphene up to HOPG is presented. All peaks are normalized in amplitude and vertically offset.

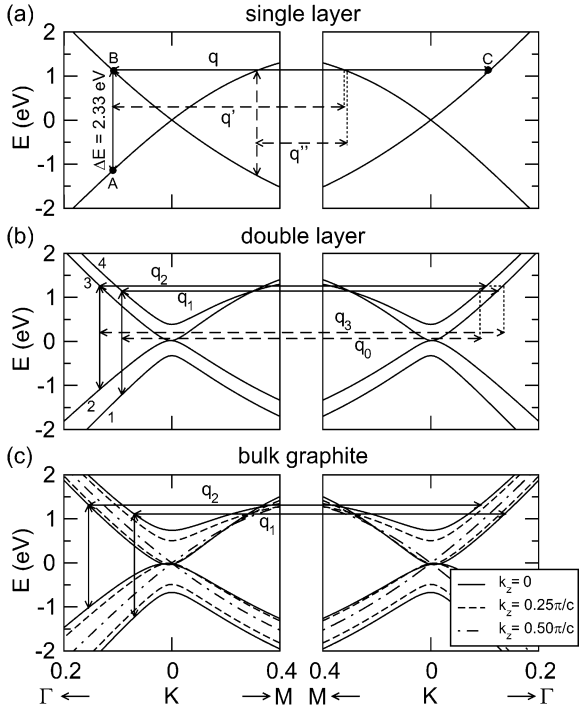

Figure 6. Electronic band structure along the high-symmetry lines Γ−K and K−M: (a) single-layer graphene, (b) double-layer graphene, and (c) bulk graphite. For bulk graphite, we display the band structure in the direction parallel to the graphene planes for different values of the transverse wave vector k_z. Vertical arrows denote vertical transitions by 2.33 eV from a valence (π) band to a conductance (π*) band. Horizontal arrows denote transitions between two states of almost equal energy by coupling to a phonon of wave vector q_i (the corresponding phonon frequencies are displayed in Table 1). Dashed horizontal lines denote transitions with considerably less weight than the solid horizontal lines (see text).

Table 1. Frequencies of the Optical Phonons Involved in the Double-Resonant Raman Model[a]

	ν_1/cm^{-1}	ν_2/cm^{-1}	$2(\nu_2 - \nu_1)$/cm^{-1}
bulk	1393.2/1393.6	1402.9/1403.1	19.4/19.0
double layer	1395.6/1395.6	1400.0/1400.6	8.8/10.0
single layer	1398.1		

[a] The corresponding phonon wave vectors q_1 and q_2 are determined from the ab initio electronic band structures of Figure 6. The splitting of the frequencies in the double-layer and bulk is due to the (weak) interlayer interaction.

from first principles, using density-functional theory in the local density approximation.[16] In the double layer, the π and π* bands split into two bands each. This gives rise to four different possible excitations. We have calculated the corresponding oscillator strengths[19] and found that, for the excitation energy of 2.33 eV, transitions 1−3 and 2−4 have negligible weight, while transitions 1−4 and 2−3 (displayed in Figure 6b) have almost equal weight. For each of the two dominant vertical transitions, there are two possible horizontal transitions. The corresponding electron−phonon coupling matrix elements for the phonons q_0 to q_3 are almost equal.[20] In theory, we therefore expect a splitting of the D′ band into four peaks of almost equal height. Our experimental data (Figure 5) shows indeed that the D′ line for the double layer can be decomposed into four peaks. However, the outer two peaks (corresponding to the phonons q_0 and q_3) have very low weight in the experimental data. We calculated from first principles[21] the phonon frequencies ν_1 and ν_2, corresponding to the wave vectors q_1 and q_2. The frequencies of the highest optical branch are given in Table 1. Because of the weak interlayer coupling, the degeneracy of this branch is lifted. However, the frequency difference remains weak (<1 cm^{-1}) and does not significantly contribute to the experimentally observed splitting of about 19 cm^{-1} of the D′ line (see Figure 5). Table 1 furthermore gives the value for $2(\nu_2 - \nu_1)$. We note that the value obtained from our first-principles calculation is only half as large as the experimentally observed splitting of about 19 cm^{-1}. This discrepancy is related to the fact that the double-resonant Raman model based on ab initio calculations also predicts a value for the dispersion of the D′ line with incident laser energy that amounts only to about half of the experimentally observed value of 99 cm^{-1}/eV.[25] We conclude therefore that the double-resonant Raman model can qualitatively explain the fourfold splitting of the D′ line in the double layer, but the amount of the splitting and the relative heights of the peaks are not properly described within this model.[26]

In bulk graphite, the π and π* bands split into a continuum of bands, i.e., they disperse in the direction k_z perpendicular to the layer. In Figure 6c, we display the bands for three different values of k_z. In the joint density of states, the vertical transitions for $k_z = 0$ have the dominant weight and are thus considered in our calculations. Because the splitting between the bands is much more pronounced than for the double layer, the value for $2(\nu_2 - \nu_1)$ is about a factor of 2 higher than for the double layer. This is in agreement with the experimental data, see Figure 5, where the splitting increases likewise by about a factor of 2 between the double layer and bulk graphite. As in the case of the double layer, there are quantitative differences between theory and experiment for graphite as well: First-principles calculations of the oscillator strengths and of the electron−phonon coupling matrix elements predict an almost equal height of the peaks, whereas the experiment shows that the lower-frequency peak has a strongly reduced weight. The peaks corresponding to the horizontal transitions q_0 and q_3 are both missing in the experimental spectrum.

Even though some quantitative differences remain, the double-resonant Raman model explains well the observed differences in the D′ line as we go from the single-layer via few-layer systems to the bulk limit. The quantitative differences may be an indicator that some essential effects are not properly included in the model. e.g., the role of excitonic effects during the electron−hole pair excitation in the double-resonance process remains to be understood. The importance of these effects has been recently demonstrated for electronic excitations in carbon nanotubes (both semiconducting and metallic).[27,28] A similar importance may be therefore expected for processes that involve electronic excitations in graphite.[29]

In conclusion, Raman mapping is a powerful tool to investigate single- and few-layer graphene flakes. It turns out that the width of the D′ line is highly sensitive to the crossover from single- to double-layer graphene, which is explained by a peak splitting following the double-resonant Raman model together with ab initio electronic band structure calculations. A remaining question is the decrease of the G line intensity with decreasing layer number compared to the almost constant spectral weight of the D′ line and the accompanied upshift of its frequency for double- and single-layer graphene. The structural quality of the flakes is studied by analyzing the D line intensity: no defects are detected in the inner part of the flake. The D line signal from the boundaries of the individual sections of the flake suggest that they act as an elastic scatterer.

Acknowledgment. We are grateful to A. Geim for the stimulation to start working on graphene and H. Heersche for useful advice on sample preparation. We acknowledge stimulating discussions with M. Haluska, A. Rubio, and M. Lazzeri. Calculations were performed at IDRIS (project 061827). Financial support from the Swiss Science Foundation (Schweizerischer Nationalfonds) is gratefully acknowledged. L.W. acknowledges support from the French National Research Agency.

References

(1) Kroto, H. W.; Heath, J. R.; O'Brien, S. C.; Curl, R. F.; Smalley, R. E. *Nature* **1985**, *318*, 162.
(2) Iijima, S. *Nature* **1991**, *354*, 56.
(3) Novoselov, K. S.; Geim, A. K.; Morozov, S. V.; Jiang, D.; Zhang, Y.; Dubonos, S. V.; Grigorieva, I. V.; Firsov, A. A. *Science* **2004**, *306*, 666.
(4) Novoselov, K. S.; Geim, A. K.; Morozov, S. V.; Jiang, D.; Katsnelson, M. I.; Grigorieva, I. V.; Dubonos, S. V.; Firsov, A. A. *Nature* **2005**, *438*, 197.
(5) Zhang, Y.; Tan, Y.-W.; Stormer, H. L.; Kim, P. *Nature* **2005**, *438*, 201.
(6) Thomsen, C.; Reich, S. *Phys. Rev. Lett.* **2000**, *85*, 5214.
(7) Ferrari, A. C.; Meyer, J. C.; Scardaci, V.; Casiraghi, C.; Lazzeri, M.; Mauri, F.; Piscanec, S.; Da Jiang; Novoselov, K. S.; Roth, S.; Geim, A. K. *Phys. Rev. Lett.* **2006**, *97*, 187401, cond-mat/0606284.
(8) Novoselov, K. S.; Jiang, D.; Schedin, F.; Booth, T. J.; Khotkevich, V. V.; Morozov, S. V.; Geim, A. K. *Proc. Natl. Acad. Sci. U.S.A.* **2005**, *102*, 10451.
(9) Reich, S.; Thomsen, C. *Philos. Trans. R. Soc. London, Ser. A* **2004**, *362*, 2271.
(10) Vidano, R. P.; Fischbach, D. B.; Willis, L. J.; Loehr, T. M. *Solid State Commun.* **1981**, *39*, 341.
(11) Tuinstra, F.; Koenig, J. L. *J. Chem. Phys.* **1970**, *53*, 1126.
(12) Saito, R.; Jorio, A.; Souza Filho, A. G.; Dresselhaus, G.; Dresselhaus, M. S.; Pimenta, M. A. *Phys. Rev. Lett.* **2002**, *88*, 027401.
(13) Wang, Y.; Alsmeyer, D. C.; McCreery, R. L. *Chem. Mater.* **1990**, *2*, 557.
(14) Peres, N. M. R.; Guinea, F.; Castro Neto, A. H. *Phys. Rev. B* **2006**, *73*, 125411.
(15) The process involving q' (a phonon very close to the K-point) does not occur because the corresponding electron−phonon coupling matrix element is approximately 0 (see footnote 24 of ref 23), and the process involving q'' has a low weight because, due to the "trigonal warping" effect, the corresponding phase space volume in the two-dimensional Brillouin zone is small compared to the phase space volume for the process involving q.
(16) We use the code ABINIT (ref 17). Wave functions are expanded in plane waves with an energy cutoff at 30 Hartrees. Core electrons are replaced by Trouiller−Martins pseudopotentials in the Kleinman−Bylander form. We use the experimental lattice constant $a = 2.459$ Å.[18]
(17) Gonze, X. et al. *Comput. Mater. Sci.* **2002**, *25*, 478.
(18) Baskin, Y.; Meyer, L. *Phys. Rev.* **1955**, *100*, 544.
(19) We use the computer code SELF written by A. Marini (http://www.fisica.uniroma2.it/~self/).
(20) Lazzeri, M. Private communication.
(21) Details of the calculations are given in ref 22. We note that the slope of the TO mode in the region between K and M where phonons are excited according to the double-resonant Raman model agrees with other recent ab initio calculations.[23,24]
(22) Wirtz, L.; Rubio, A. *Solid State Commun.* **2004**, *131*, 141.
(23) Piscanec, S.; Lazzeri, M.; Mauri, F.; Ferrari, A. C.; Robertson, J. *Phys. Rev. Lett.* **2004**, *93*, 185503.
(24) Maultzsch, J.; Reich, S.; Thomsen, C.; Requardt, H.; Ordejón, P. *Phys. Rev. Lett.* **2004**, *92*, 075501.
(25) We note that Ferrari et al.[7] overcome this difficulty by using the semiempirical parameter dω/dq (caption of Table I of ref 7), which is fitted to the experimental dispersion of the D′ peak. We have avoided the use of this semiempirical parameter in order to assess the quantitative validity of the double-resonant Raman model based on first-principles calculations. The good agreement between experimental and theoretical D peak dispersion in ref 6 is based on a corresponding fit of the hopping parameter in the tight-binding band structure and on the parametrization of the phonon dispersion relation.
(26) For an exact quantitative evaluation of the peak heights, an integration in the two-dimensional Brillouin zone for all transitions of energy $\Delta E = 2.33$ eV would have to be performed.
(27) Spataru, C. D.; Ismail-Beigi, S.; Benedict, L. X.; Louie, S. G. *Phys. Rev. Lett.* **2004**, *92*, 077402.
(28) Chang, E.; Bussi, G.; Ruini, A.; Molinari, E. *Phys. Rev. Lett.* **2004**, *92*, 196401.
(29) We note that the picture of independent electron−hole pair excitations has been quantitatively very successful for the assignment of nanotube spectra to the chiral indices (m,n). However, this success was based on the use of tight-binding band structures with correspondingly fitted parameters. A parameter-free, first-principles calculation of the optical spectra of carbon nanotubes must take into account electron−electron and electron−hole interaction, and we suggest that this may be true for graphite as well.

NL061702A

2.4 Effects of electron-electron correlation on the electron-phonon coupling in graphite

In general, for both metals and insulators, density-functional perturbation theory[3] using LDA (local-density approximation) or GGA (generalized-gradient approximation) gives phonon dispersions in close agreement with experimental results. For graphene and graphite, we have seen in section 2.2 that DFT-GGA or DFT-LDA calculation are in excellent agreement with experimental data. Only the highest optical phonon branch (HOB) around the high-symmetry point K seems to display a pronounced deviation from the most recent measurement using inelastic X-ray scattering[13]. But what is special about this particular branch around K? Why does standard DFT work for all branches all over the Brillouin zone but fails at this particular point? Since the HOB around K is responsible for the D and 2D lines in the Raman spectra, the understanding of this failure is particularly important. As we mentioned in section 2.3: If the frequently used double-resonant Raman model[10] is to explain quantitatively the dispersion of the D line and the splitting of the 2D line for double and multi-layer graphene, the slope of the HOB around K should be factor 2 higher than obtained in standard DFT-LDA or DFT-GGA calculations.

The problem was solved in collaboration with M. Lazzeri, and F. Mauri (IMPMC, Université Pierre et Marie Curie, Paris) [34]. Starting point of the work was the observation that the HOB displays a Kohn anomaly at K, i.e., a kink in the phonon dispersion.[14] Furthermore, it had been shown[14] that the linear slope of the HOB around K is proportional to the square of the electron-phonon coupling matrix element (EPC) between the HOB and the π bands. We have evaluated in Ref. [34] the EPC in the GW-approximation, i.e., taking into account the electron-electron correlation. We found a strong renormalization of the EPC, which almost doubles the slope of the HOB around K (with respect to standard DFT calculations). This explains the missing factor 2 in the ab-initio description of the D line dispersion and the 2D line splitting and yields a phonon dispersion in good agreement with recent inelastic X-ray scattering measurements[15].

The failure of GGA and LDA to describe the HOB around K seems to be related to the fact that these functionals are not self-interaction (SI) free: Since v_{xc}, the correlation and exchange energy functional, depends on the total electron density, a particular electron interacts not only with all the other electrons but also with itself. This self-interaction is often negligible. But it can become important for localized states which tend to be artificially delocalized by functionals without SI correction.[16]. Why does self-interaction affect in particular the HOB at K? The answer lies in the particular displacement pattern (see Fig. 3 of Ref. [34] which is reprinted on the following pages). In the equilibrium geometry, the π electrons are delocalized and equally shared by all bonds (which all have the same length and have a character intermediate between single and double). The HOB at K leaves all bond angles unchanged at 120 degrees but leads to alternating shorter and longer bonds. The shorter bonds acquire slightly more double bond character and the longer bonds become more single-bond like (panel c of Fig. 3). A self-interaction free functional renders the localization of electrons in the "double" bonds

---

[13] J. Maultzsch, S. Reich, C. Thomsen, H. Requardt, and P. Ordejón, Phys. Rev. Lett. **92**, 075501 (2004).

[14] Piscanec, M. Lazzeri, F. Mauri, A.C. Ferrari, and J. Robertson, Phys. Rev. Lett. **93**, 185503 (2004).

[15] A. Grüneis et al., to be published.

[16] See, e.g., S. Kümmel and L. Kronik, Rev. Mod. Phys. **80**, 3 (2008).

energetically more favorable than the LDA or GGA functional. Consequently, the total energy of the lattice with displaced atoms is lowered in SI free calculation with respect to LDA or GGA calculations. Consequently, the HOB frequency at K is considerably lower if one uses a self-interaction free approach.

Some indication that the above explanation for the failure of the LDA and GGA functionals is correct is given by our phonon calculations with the hybrid B3LYP functional. While B3LYP is not completely self-interaction free either, it contains at least a partial contribution of non-local (and self-interaction free) Fock-exchange. Indeed, the B3LYP leads to a considerably lower HOB frequency at K while giving results in good agreement with LDA and GGA everywhere else. By "tuning" the percentage of admixture of Fock-exchange to the exchange-correlation functional, it is possible to obtain the same HOB frequency as within the GW approximation. In the limit of the pure Hartree-Fock approximation, the HOB becomes imaginary. This means that within Hartree-Fock, the most stable configuration of graphene would be the distorted configuration of Fig. 3 c).

RAPID COMMUNICATIONS

PHYSICAL REVIEW B **78**, 081406(R) (2008)

Impact of the electron-electron correlation on phonon dispersion: Failure of LDA and GGA DFT functionals in graphene and graphite

Michele Lazzeri,[1] Claudio Attaccalite,[2] Ludger Wirtz,[3] and Francesco Mauri[1]
[1]*IMPMC, Universités Paris 6 et 7, IPGP, CNRS, 140 rue de Lourmel, 75015 Paris, France*
[2]*Unidad de Fisica de Materiales, European Theoretical Spectroscopy Facility (ETSF), Universidad del Pais Vasco, 20018 San Sebastian, Spain*
[3]*Institute for Electronics, Microelectronics, and Nanotechnology, CNRS, 59652 Villeneuve d'Ascq, France*

(Received 29 May 2008; published 26 August 2008)

We compute the electron-phonon coupling (EPC) of selected phonon modes in graphene and graphite using various *ab initio* methods. The inclusion of nonlocal exchange-correlation effects within the *GW* approach strongly renormalizes the square EPC of the A_1' **K** mode by almost 80% with respect to density-functional theory in the LDA and GGA approximations. Within GW, the phonon slope of the A_1' **K** mode is almost two times larger than in GGA and LDA, in agreement with phonon dispersions from inelastic x-ray scattering and Raman spectroscopy. The hybrid B3LYP functional overestimates the EPC at **K** by about 30%. Within the Hartree-Fock approximation, the graphene structure displays an instability under a distortion following the A_1' phonon at **K**.

DOI: 10.1103/PhysRevB.78.081406 PACS number(s): 78.30.Na, 71.15.Mb, 63.20.kd, 81.05.Uw

The electron-phonon coupling (EPC) is one of the fundamental quantities in condensed matter. It determines phonon dispersions and Kohn anomalies, phonon-mediated superconductivity, electrical resistivity, Jahn-Teller distortions, etc. Nowadays, density-functional theory (DFT) within local and semilocal approximations is considered the "standard model" to compute *ab initio* the electron-phonon interaction and phonon dispersions.[1] Thus, a failure of DFT would have major consequences in a broad context. In GGA and LDA approximations,[2] the electron exchange-correlation energy is a local functional of the charge density, and the long-range character of the electron-electron interaction is neglected. These effects are taken into account by Green's-function approaches based on the screened electron-electron interaction *W* such as the *GW* method.[3] *GW* is considered the most precise *ab initio* approach to determine electronic bands, but so far it has never been used to compute EPCs nor phonon dispersions. The semiempirical B3LYP functional[2] partially includes long-range Hartree-Fock (HF) exchange. B3LYP has been used to compute phonon frequencies but, so far, not the EPC.

The EPC is a key quantity for graphene, graphite, and carbon nanotubes. It determines the Raman spectrum, which is the most common characterization technique for graphene and nanotubes[4,5] and the high-bias electron transport in nanotubes.[6] Graphene and graphite are quite unique systems in which the actual value of the EPC for some phonons can be obtained almost directly from measurements. In particular, the square of the EPC of the highest optical-phonon branch (HOB) at the symmetry **K** point is proportional to the HOB slope near **K**.[7] The HOB **K** slope can be measured by inelastic x-ray scattering (IXS)[8,9] or by the dispersion of the D and 2D lines as a function of the excitation energy in a Raman experiment.[5,10–13] A careful look at the most recent data suggests that the experimental phonon slopes (and thus the EPC) are underestimated by DFT.[5] The ability of DFT (LDA and GGA) in describing the EPC of graphene was also questioned by a recent theoretical work.[14]

Here, we show that: (i) the *GW* approach, which provides the most accurate *ab initio* treatment of electron correlation, can be used to compute the electron-phonon interaction and the phonon dispersion; (ii) in graphite and graphene, DFT (LDA and GGA) underestimates, by a factor of 2, the slope

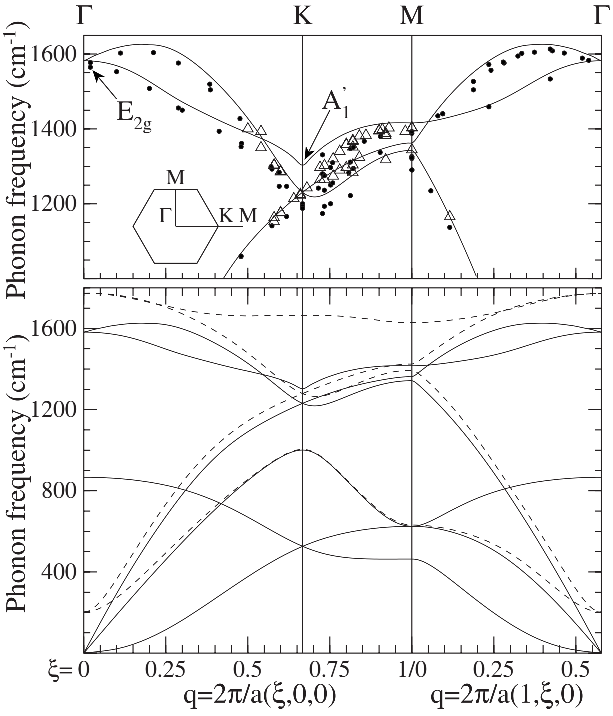

FIG. 1. Upper panel: Phonon dispersion of graphite. Lines are DFT calculations, dots and triangles are IXS measurements from Refs. 8 and 9, respectively. Lower panel: Phonon dispersion of graphene from DFT calculations. Dashed lines are obtained by subtracting, from the dynamical matrix, the phonon self-energy between the π bands ($\widetilde{\omega_{\mathbf{q}}}$ in the text).

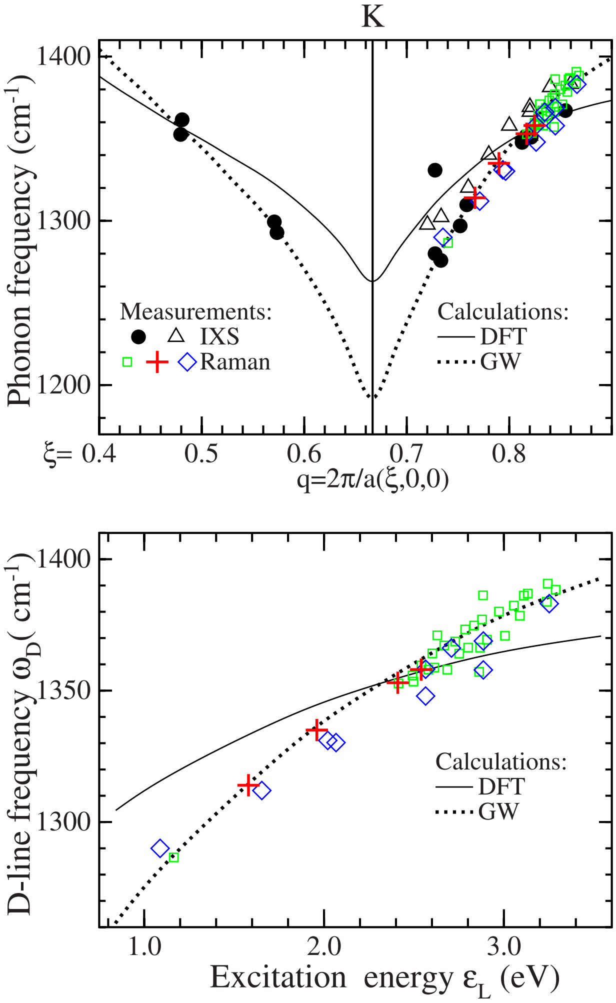

FIG. 2. (Color online). Upper panel: Dispersion of the highest optical phonon in graphite near **K**. Calculations are from DFT or corrected to include *GW* renormalization of the EPC. Here, the DFT dispersion is vertically shifted by -40 cm^{-1} to fit measurements. Dots and triangles are IXS data from Refs. 8 and 9, respectively. Squares, plus, and diamonds are obtained from Raman data of Refs. 10–12, respectively, using the double-resonance model (Refs. 12 and 13). Lower panel: Dispersion of the Raman D line.

of the phonon dispersion of the highest optical branch at the zone boundary and the square of its EPC by almost 80%; (iii) *GW* reproduces the experimental phonon dispersion near **K**, the value of the EPC, and the electronic band dispersion; (iv) the B3LYP hybrid functional[2] gives phonons close to *GW* but overestimates the EPC at **K** by about 30%; and (v) within HF the graphite structure is unstable.

In Fig. 1, we show the phonon dispersion of graphite computed with DFT$_{\text{GGA}}$.[15] In spite of the general good agreement with IXS data, the situation is not clear for the HOB near **K**. In fact, despite the scattering among experimental data, the theoretical HOB is always higher in energy with respect to measurements, and the theoretical phonon slope (for the HOB near **K**) is underestimating the measured one. It is also remarkable that while the DFT **K** frequency is $\sim$1300 cm^{-1}, the highest measured is much lower at $\sim$1200 cm^{-1}.

The dispersion of the HOB near **K** can also be obtained by Raman measurements of the graphene and graphite D line ($\sim$1350 cm^{-1}).[12] The D-line frequency ω_D depends on the energy of the exciting laser ϵ_L. According to the double-resonance model,[12,13] ϵ_L activates a phonon of the HOB with momentum $\mathbf{q}=\mathbf{K}+2\Delta\mathbf{q}$ along the **K**-**M** line[5] and energy $\hbar\omega_D$. $\Delta\mathbf{q}$ is determined by $\epsilon_{\mathbf{K}-\Delta\mathbf{q},\pi^*}-\epsilon_{\mathbf{K}-\Delta\mathbf{q},\pi}=\epsilon_L-\hbar\omega_D/2$ where $\epsilon_{\mathbf{k},\pi/\pi^*}$ is the energy of the π/π^* electronic state with momentum **k**. Thus, by measuring ω_D vs ϵ_L and considering the electronic π bands dispersion from DFT, one can obtain the phonon dispersion ω_D vs **q**.[12] The phonon dispersion thus obtained is very similar to the one from IXS data and its slope is clearly underestimated by DFT (Fig. 2, upper panel). The same conclusion is reached by comparing the D-line dispersion ω_D vs ϵ_L (directly obtained from measurements) with calculations (Fig. 2, lower panel). Note that the dispersions of the Raman 2D line[5] is consistent with that of the D line and thus in disagreement with DFT (LDA and GGA) as well.

The steep slope of the HOB near **K** is due to the presence of a Kohn anomaly for this phonon.[7] In particular, in Ref. 7, it was shown that the HOB slope is entirely determined by the contribution of the phonon self-energy between π bands ($P_{\mathbf{q}}$) to the dynamical matrix $\mathcal{D}_{\mathbf{q}}$. $\omega_{\mathbf{q}}=\sqrt{\mathcal{D}_{\mathbf{q}}/m}$ is the phonon pulsation, where m is the mass. For a given phonon with momentum **q**,

$$\mathcal{D}_{\mathbf{q}}=B_{\mathbf{q}}+P_{\mathbf{q}}, \qquad P_{\mathbf{q}}=\frac{4}{N_k}\sum_{\mathbf{k}}\frac{|D_{(\mathbf{k+q})\pi^*,\mathbf{k}\pi}|^2}{\epsilon_{\mathbf{k},\pi}-\epsilon_{\mathbf{k+q},\pi^*}}, \tag{1}$$

where the sum is performed on N_k wave vectors all over the Brillouin zone; $D_{(\mathbf{k+q})i,\mathbf{k}j}=\langle\mathbf{k}+\mathbf{q},i|\Delta V_{\mathbf{q}}|\mathbf{k},j\rangle$ is the EPC; $\Delta V_{\mathbf{q}}$ is the derivative of the Kohn-Sham potential with respect to the phonon mode; and $|\mathbf{k},i\rangle$ is the Bloch eigenstate with momentum **k**, band index i, and energy $\epsilon_{\mathbf{k},i}$. $\pi(\pi^*)$ identifies the occupied (empty) π band. In Fig. 1 we show a fictitious phonon dispersion $\tilde{\omega}_{\mathbf{q}}$ obtained by subtracting $P_{\mathbf{q}}$ from the dynamical matrix ($\tilde{\omega}_{\mathbf{q}}=\sqrt{B_{\mathbf{q}}/m}$) for each phonon. The HOB is the branch which is mostly affected and, for the HOB, $\tilde{\omega}_{\mathbf{q}}$ becomes almost flat near **K**. Thus, DFT (LDA or GGA) fails in describing the HOB slope near **K**, the slope which is determined by $P_{\mathbf{q}}$. $P_{\mathbf{q}}$ is given by the square of EPC divided by π-band energies. Thus, the DFT failure can be attributed to a poor description of the EPC or of the π-band dispersion.

In graphene and graphite, it is known that standard DFT provides an underestimation of the π- and π^*-band slopes of $\sim$10–20%.[16,17] A very precise description of the bands, in better agreement with measurements, is obtained using *GW*.[16,17] We thus computed the π bands with DFT (both LDA and GGA)[18] and *GW* (Ref. 19) and compared with HF (Ref. 20) and B3LYP.[20] Details are in Ref. 21. The different methods provide band dispersions whose overall behavior can be described by a scaling of the π energies.[16] The different scaling factors can be obtained by comparing $\Delta\epsilon_g$, the energy difference between the π^* and π bands at the symmetry point **M** (**L**) for graphene (graphite). $\Delta\epsilon_g$ is larger in

TABLE I. EPC of the $\mathbf{\Gamma}$-E$_{2g}$ and **K**-A$_1'$ phonons computed with various approximations. $\Delta\epsilon_g$ (eV), $\langle D_{\mathbf{q}}^2\rangle_F$ (eV^2/Å^2), and $\alpha_{\mathbf{q}}$ (eV/Å^2) are defined in the text. ω_Γ ($\omega_{\mathbf{K}}$) is the phonon frequency of the E$_{2g}$ A$_1'$ mode (cm^{-1}). The *GW* $\omega_{\mathbf{K}}$ for graphite (in parenthesis) is not computed directly (see the text). $i=\sqrt{-1}$ is the imaginary unit.

	Graphene						
	$\Delta\epsilon_g$	$\langle D_\Gamma^2\rangle_F$	α_Γ	ω_Γ	$\langle D_{\mathbf{K}}^2\rangle_F$	$\alpha_{\mathbf{K}}$	$\omega_{\mathbf{K}}$
DFT$_{\text{LDA}}$	4.03	44.4	11.0	1568	89.9	22.3	1275
DFT$_{\text{GGA}}$	4.08	45.4	11.1	1583	92.0	22.5	1303
GW	4.89	62.8	12.8	–	193	39.5	–
B3LYP	6.14	82.3	13.4	1588	256	41.7	1172
HF	12.1	321	26.6	1705	6020	498	960 × *i*
	Graphite						
	$\Delta\epsilon_g$	$\overline{\langle D_\Gamma^2\rangle_F}$	α_Γ	ω_Γ	$\overline{\langle D_{\mathbf{K}}^2\rangle_F}$	$\alpha_{\mathbf{K}}$	$\omega_{\mathbf{K}}$
DFT$_{\text{LDA}}$	4.06	43.6	10.7	1568	88.9	21.8	1299
DFT$_{\text{GGA}}$	4.07	44.9	11.0	1581	91.5	22.5	1319
GW	4.57	58.6	12.8	–	164.2	35.9	(1192)

GW than in DFT (Table I). Thus, inclusion of the *GW* correction to the electronic bands alone results in a larger denominator in Eq. (1), providing a smaller phonon slope and a worse agreement with experiments. The underestimation of the **K** phonon slope in DFT is thus due to the EPC.

The EPC can be computed with linear response as, e.g., in Ref. 7 but, at present, the use of this technique within *GW* is not feasible. Alternatively, the EPC associated with a phonon mode can be determined by the variation of the electronic band energies by displacing the atoms according to the considered mode. In graphene, at **K**, there are doubly degenerate π electronic states at the Fermi level. The HOB corresponds to the E$_{2g}$ phonon at $\mathbf{\Gamma}$ and to the A$_1'$ at **K**. As an example, we consider the EPC associated with the $\mathbf{\Gamma}$-E$_{2g}$ phonon and we displace the atoms according to its phonon pattern (see Fig. 3). Following symmetry arguments,[22] one can show that, in an arbitrary base of the two-dimensional space of the π bands at **K**, the Hamiltonian is the 2 × 2 matrix

$$H = 2\sqrt{\langle D_\Gamma^2\rangle_F}\begin{pmatrix} a & b \\ b^* & -a \end{pmatrix} d + \mathcal{O}(d^2), \qquad (2)$$

where *each atom is displaced by d*, $|a|^2+|b|^2=1$, and $\langle D_\Gamma^2\rangle_F = \Sigma_{i,j}^{\pi,\pi^*}|D_{\mathbf{K}i,\mathbf{K}j}|^2/4$, where the sum is performed on the two degenerate π bands. Diagonalizing Eq. (2), we see that an atomic displacement following the $\mathbf{\Gamma}$-E$_{2g}$ phonon induces the splitting $\Delta E_\Gamma = \epsilon_{\mathbf{K},\pi^*} - \epsilon_{\mathbf{K},\pi}$ and

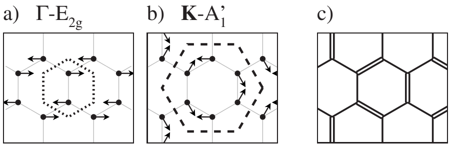

FIG. 3. (a) and (b) Patterns of the $\mathbf{\Gamma}$-E$_{2g}$ and **K**-A$_1'$ phonons of graphene. Dotted and dashed lines are the Wigner-Seitz cells of the unit cell and of the $\sqrt{3}\times\sqrt{3}$ supercell. (c) HF equilibrium structure.

$$\langle D_\Gamma^2\rangle_F = \lim_{d\to 0}\frac{1}{16}\left(\frac{\Delta E_\Gamma}{d}\right)^2. \qquad (3)$$

In analogous way, we define $\langle D_{\mathbf{K}}^2\rangle_F = \Sigma_{i,j}^{\pi,\pi^*}|D_{(2\mathbf{K})i,\mathbf{K}j}|^2/4$ for the A$_1'$ phonon at **K**. Let us consider a $\sqrt{3}\times\sqrt{3}$ graphene supercell. Such a cell can be used to displace the atoms following the **K**-A$_1'$ phonon (Fig. 3) since the **K** point is refolded in $\mathbf{\Gamma}$. Let us call $\Delta E_{\mathbf{K}}$ the splitting of the $\epsilon_{\mathbf{K},\pi}$ bands induced by this displacement (since **K** is refolded in $\mathbf{\Gamma}$, here $\epsilon_{\mathbf{K},\pi}$ denotes the energies of the $\mathbf{\Gamma}$ band of the supercell corresponding to the π band at **K** in the unit cell). Considering the atomic distortion of Fig. 3 and displacing each atom by *d*, one can show that

$$\langle D_{\mathbf{K}}^2\rangle_F = \lim_{d\to 0}\frac{1}{8}\left(\frac{\Delta E_{\mathbf{K}}}{d}\right)^2. \qquad (4)$$

In practice, by calculating band energies in the distorted structures of Fig. 3 and using Eqs. (3) and (4), one obtains the EPCs of the $\mathbf{\Gamma}$-E$_{2g}$ and **K**-A_1' phonons between π states. Similar equations can be used for graphite.[23] Results are in Table I together with the computed phonon frequencies. The EPCs from DFT$_{\text{GGA}}$ are in agreement with those from linear response.[7] We also remark that, within the present "frozen-phonon" approach, the Coulomb vertex corrections are implicitly included within *GW*.

To study the effect of the different computational methods on the phonon slope (which is determined by $P_{\mathbf{q}}$) we recall that $P_{\mathbf{q}}$ is the ratio of the square EPC and band energies [Eq. (1)]. Thus, we have to compare $\alpha_{\mathbf{q}} = \langle D_{\mathbf{q}}^2\rangle_F/\Delta\epsilon_g$. As an example, assuming that the change in $P_{\mathbf{q}}$ from DFT to *GW* is constant for **q** near **K**,

$$\frac{P_{\mathbf{q}}^{GW}}{P_{\mathbf{q}}^{\text{DFT}}} \simeq \frac{\alpha_{\mathbf{K}}^{GW}}{\alpha_{\mathbf{K}}^{\text{DFT}}} = r^{GW} \qquad (5)$$

and r^{GW} provides the change in the **K** phonon slope going from DFT to *GW*. To understand the results, we recall that in standard DFT the exchange-correlation depends only on the local electron density. In contrast, the exchange interaction in HF and *GW* is nonlocal. Furthermore, in *GW*, correlation effects are nonlocal since they are described through a dynamically screened Coulomb interaction. The hybrid functional B3LYP gives results intermediate between DFT and HF.

Both α_Γ and $\alpha_{\mathbf{K}}$ are heavily overestimated by HF, the **K**-EPC being so huge that graphene is no more stable (the **K**A$_1'$ phonon frequency is not real). Indeed, the HF equilibrium geometry is a $\sqrt{3}\times\sqrt{3}$ reconstruction with alternating double and single bonds of 1.40 and 1.43 Å lengths as in Fig. 3 (with a gain of 0.9 meV/atom). These results not only demonstrate the major effect of the long-range character of the exchange for the **K**-EPC (Ref. 14) but also the importance of the proper inclusion of the screening (included in *GW* but neglected in HF). Notice also that $\alpha_{\mathbf{K}}^{GW}$ of graphite is smaller with respect to graphene by ~10%. This is explained by the larger screening of the exchange in graphite (due to the presence of adjacent layers) than in graphene. On the contrary, within GGA and LDA, the graphite phonon frequencies and EPCs are very similar to those of graphene since these functionals do not take into account the electron-electron interaction screening.

Concerning the phonon slope, $\alpha_{\mathbf{\Gamma}}^{GW}$ is only 15% larger than $\alpha_{\mathbf{\Gamma}}^{\mathrm{DFT}}$. Indeed, DFT reproduces with this precision the phonon frequency and dispersion of the HOB at $\mathbf{\Gamma}$. On the contrary, $\alpha_{\mathbf{K}}^{GW}$ is 60% larger than $\alpha_{\mathbf{K}}^{\mathrm{DFT}}$ for graphite. This large increase with respect to DFT could explain the disagreement between DFT and the measured A_1' phonon dispersion near **K**. To test this, we need to determine the *GW* phonon dispersion that, using Eq. (5), becomes $\omega_{\mathbf{q}}^{GW} \simeq \sqrt{(B_{\mathbf{q}}^{GW}+r^{GW}P_{\mathbf{q}}^{\mathrm{DFT}})/m}$, where $r^{GW}=1.6$. Moreover, we can assume $B_{\mathbf{q}}^{GW}\simeq B_{\mathbf{K}}^{GW}$ since the $B_{\mathbf{q}}$ component of the dynamical matrix [Eq. (1)] is not expected to have an important dependence on **q** (Fig. 1). The value of $B_{\mathbf{K}}^{GW}$ is obtained as a fit to the measurements of Fig. 2.[24] The resulting **K** A_1' phonon frequency is 1192 cm^{-1}, which is our best estimation and is almost 100 cm^{-1} smaller than in DFT. The phonon dispersion thus obtained and the corresponding D-line dispersion are both in better agreement with measurements (Fig. 2).

The partial inclusion of long-range exchange within the semiempirical B3LYP functional leads to a strong increase in the EPC at **K** as compared to the LDA and GGA functionals. However, comparing to the *GW* value, the EPC is overestimated by 30% and the corresponding frequency for the **K**-A_1' mode at 1172 cm^{-1} falls well below the degenerate **K** mode, which is around 1200 cm^{-1} in the experiment[8,9] (Fig. 1) and at 1228 cm^{-1} in our phonon calculation with B3LYP. We have checked that tuning the percentage of HF exchange in the hybrid functional allows to match the EPC value of the *GW* approach (in which case, the **K**-A_1' mode remains the highest mode). This may be a good way to calculate the full phonon dispersion of graphite/graphene within DFT, yet with an accuracy close to the one of the *GW* approach.

Concluding, *GW* is a general approach to compute accurate EPC where DFT functionals fail. Such a failure in graphite/graphene is due to the interplay between the two-dimensional Dirac-type band structure and the long-range character of the Coulomb interaction.[14] However, *GW* can be also used in cases (in which the EPC is badly described by DFT) where the electron exchange and correlation are more short ranged.[25]

Calculations were done at IDRIS (Projects No. 081202 and No. 081827). C.A. and L.W. acknowledge French ANR Project No. PJC05_6741. We thank D. M. Basko, A. Rubio, J. Schamps, and C. Brouder for the discussions and A. Marini for the code YAMBO.

---

[1] S. Baroni *et al.*, Rev. Mod. Phys. **73**, 515 (2001).

[2] LDA, GGA and B3LYP refer, respectively, to D. M. Ceperley *et al.*, Phys. Rev. Lett. **45**, 566 (1980); J. P. Perdew *et al.*, *ibid.* **77**, 3865 (1996); A. D. Becke, J. Chem. Phys. **98**, 5648 (1993).

[3] F. Aryasetiawan *et al.*, Rep. Prog. Phys. **61**, 237 (1998); W. G. Aulbur *et al.*, Solid State Phys. **54**, 1 (2000); G. Onida *et al.*, Rev. Mod. Phys. **74**, 601 (2002).

[4] S. Reich *et al.*, Philos. Trans. R. Soc. London, Ser. A **362**, 2271 (2004).

[5] A. C. Ferrari *et al.*, Phys. Rev. Lett. **97**, 187401 (2006); D. Graf *et al.*, Nano Lett. **7**, 238 (2007).

[6] Z. Yao *et al.*, Phys. Rev. Lett. **84**, 2941 (2000).

[7] S. Piscanec *et al.*, Phys. Rev. Lett. **93**, 185503 (2004).

[8] J. Maultzsch *et al.*, Phys. Rev. Lett. **92**, 075501 (2004).

[9] M. Mohr *et al.*, Phys. Rev. B **76**, 035439 (2007).

[10] I. Pócsik *et al.*, J. Non-Cryst. Solids **227**, 1083 (1998).

[11] P. H. Tan *et al.*, Phys. Rev. B **66**, 245410 (2002).

[12] J. Maultzsch *et al.*, Phys. Rev. B **70**, 155403 (2004).

[13] C. Thomsen *et al.*, Phys. Rev. Lett. **85**, 5214 (2000).

[14] D. M. Basko *et al.*, Phys. Rev. B **77**, 041409(R) (2008).

[15] Calculations were done as in Ref. 1. Technical details and thus phonon dispersions are the same as in Ref. 7.

[16] S. Y. Zhou *et al.*, Phys. Rev. B **71**, 161403(R) (2005); S. G. Louie, in *Topics in Computational Materials Science*, editor by C. Y. Fong (World Scientific, Singapore, 1997), p. 96.

[17] A. Grüneis *et al.*, Phys. Rev. Lett. **100**, 037601 (2008).

[18] LDA and GGA calculations were done with the code PWSCF (http://www.quantum-espresso.org), with pseudopotentials of the type; N. Troullier *et al.*, Phys. Rev. B **43**, 1993 (1991).

[19] *GW* calculations were done with the code YAMBO (the YAMBO project, http://www.yambo-code.org/), within the nonself-consistent G_0W_0 approximation starting from DFT-LDA wave functions and using a plasmon-pole model for the screening, following; M. S. Hybertsen *et al.*, Phys. Rev. B **34**, 5390 (1986).

[20] HF and B3LYP calculations were done with the code CRYSTAL (V. R. Saunders *et al.*, *CRYSTAL03 Users Manual* (University of Torino, Torino, 2003), using the TZ basis by Dunning (without the diffuse P function).

[21] For graphite we used the experimental lattice parameters ($a=2.46$ Å, $c=6.708$ Å). For graphene we used $a=2.46$ Å and a vacuum layer of 20 a.u. EPCs were calculated on a structure distorted by $d=0.01$ a.u. For graphene, the electronic integration on the 1×1 cell was done with a $18\times18\times1$ grid for LDA/GGA, $36\times36\times1$ for GW, and $66\times66\times1$ for B3LYP/HF. For graphite it was $18\times18\times6$. For the $\sqrt{3}\times\sqrt{3}$ cell we used the nearest equivalent k grid. Plane waves are expanded up to 60-Ry cutoff. We used a Fermi-Dirac smearing with 0.002-Ry width for B3LYP/HF/*GW* and a Gaussian smearing with 0.02-Ry width for LDA/GGA.

[22] J. C. Slonczewski *et al.*, Phys. Rev. **109**, 272 (1958); See also Suppl. information to S. Pisana *et al.*, Nat. Mater. **6**, 198 (2007).

[23] In graphite, at the high-symmetry **H** point the four π bands are degenerate two by two, $\Delta\epsilon_0$ being the energy difference. By displacing the atoms according to the $\mathbf{\Gamma}$ E_{2g} phonon, these bands remain degenerate and the energy difference is $\Delta\epsilon$. In analogy to Eqs. (3) and (4) we define $\overline{\langle D_{\mathbf{\Gamma}}^2\rangle_F}=(\Delta\epsilon^2-\Delta\epsilon_0^2)/(16d^2)$. By displacing the atoms according to the **K** A_1' phonon, the four bands are no longer degenerate, being π^* (π) the two bands which are up (down) shifted and $\Delta\epsilon=\epsilon_{\pi^*}-\epsilon_{\pi}$. We define $\overline{\langle D_{\mathbf{K}}^2\rangle_F}=(\overline{\Delta\epsilon^2}-\Delta\epsilon_0^2)/(8d^2)$, where $\overline{\Delta\epsilon^2}$ indicates the average between the four possible $\pi^*-\pi$ couples.

[24] In principle, a direct calculation of $\omega_{\mathbf{K}}^{GW}$ (and thus of $B_{\mathbf{K}}^{GW}$) could be obtained, e.g., by finite differences from a prohibitively expensive *GW* total energy calculation.

[25] P. Zhang *et al.*, Phys. Rev. Lett. **98**, 067005 (2007).

2.5 Non-adiabatic effects for the phonons of excited graphite

Recently, the "breakdown of the Born-Oppenheimer approximation" for the description of phonons in charged graphene has received considerable attention in the graphene community[17]. The consequence of this non-adiabatic effect on the phonon frequencies is a pronounced upshift of the Raman G line that was measured for both positive and negative charging.[18] The non-adiabatic stiffening of the E_{2g2} phonon frequency in charged graphene is explained in Fig. 2.5. Panel A shows the electronic band-structure and band-filling in the equilibrium geometry. The conical intersection of the π and π^* bands ("Dirac point") is located at the high symmetry point K (corner of the hexagonal 1st Brillouin zone). Since the system is negatively charged, the π^* band is filled up to the (shifted) Fermi level ϵ_F. During phononic displacement of the atoms (represented in panel D), the linear crossing of the π and π^* bands remains preserved, but the crossing point ("Dirac point") is shifted away from K. In the adiabatic case the electronic occupation follows the displaced cone. The states remain filled up to ϵ_F and the Fermi surface follows the Dirac-point displacement. In the non-adiabatic case (panel C), the cone is moving so quickly that the electrons do not "have time" to readjust. The electron momentum is conserved and a state with momentum k is occupied if the state with the same k is occupied in the unperturbed case. As a consequence, the Fermi surface is the same as in the unperturbed case and does not follow the Dirac-cone displacement. Due to the movement

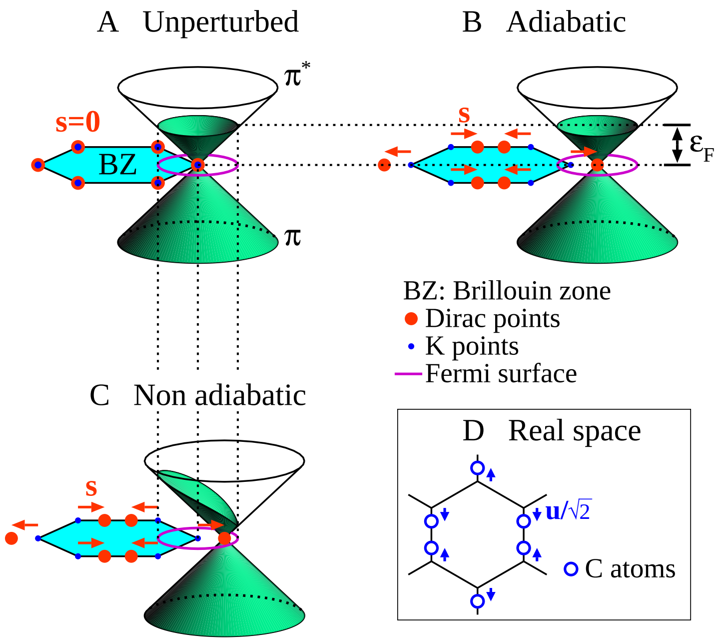

Figure 2.5: Sketch of the effect of non-adiabaticity on the electronic occupation of the π and π^* bands in charged graphene (see text). Figure reprinted from Ref.[18]

---

[17] M. Lazzeri and F. Mauri, Phys. Rev. Lett. **97**, 266407 (2006)

[18] S. Pisana, M. Lazzeri, C. Casiraghi, K.S. Novoselov, A.K. Geim, A.C. Ferrari, and F. Mauri, Nature Mat. **6**, 198 (2007).

of the cone, some electrons are shifted upwards in energy. This raises the total energy of the system with respect to the adiabatic case and leads thus to the observed stiffening of the G line. The argument works analogously for positively charged graphene where the Fermi level is shifted downwards into the π band.

Motivated by this simple picture, we have checked that non-adiabaticity can be approximately taken into account in DFT calculations by "freezing" the electronic occupation to the one of the unperturbed geometry. (The default is that, upon phononic displacement, the occupation is readjusted self-consistently.) Numerical calculations for charged graphene give results very close to the results obtained by the more precise time-dependent perturbation theory.[19]

In collaboration with the groups of H. Petek (Pittsburgh,USA) and of M. Kitajima (Tsukuba, Japan), we have studied in Ref. [31] the coherent excitation of phonons in graphite by femtosecond-laser pulses, in particular the femtosecond dynamics of the 47.5 THz coherent E_{2g} optical phonon. Upon <10 fs laser excitation, the phonon frequency upshifts proportionally to the photo-excitation density and relaxes within 0.5 ps to a stationary value through electron-phonon coupling. Our constrained DFT calculations have revealed that neutral excitations cause non-adiabatic effects on the frequency of the E_{2g} mode. Neutral excitation through laser pulses can thus have a similarly strong impact on the frequency as charging. Furthermore, the frequency upshift reflects the energy distribution of excited electrons. Thus, measuring the phonon frequency as a function of time allows to draw conclusions on the relaxation pathway of hot carriers by electron-electron and electron-phonon interaction.

---

[19] A.M. Saitta, L. Wirtz, M. Lazzeri, A. Rubio, and F. Mauri, unpublished.

RAPID COMMUNICATIONS

PHYSICAL REVIEW B **77**, 121402(R) (2008)

Ultrafast electron-phonon decoupling in graphite

Kunie Ishioka,[*] Muneaki Hase,[†] and Masahiro Kitajima
Advanced Nano-Characterization Center, National Institute for Materials Science, Tsukuba 305-0047, Japan

Ludger Wirtz
Institute for Electronics, Microelectronics, and Nanotechnology, CNRS, 59652 Villeneuve d'Ascq Cedex, France

Angel Rubio
European Theoretical Spectroscopy Facility, Universidad del País Vasco, Centro Mixto CSIC-UPV/EHU, Edificio Korta,
Avenida de Tolosa 72, 20018 Donostia, Spain
and Donostia International Physics Center, P. Manuel de Lardizabal 4, 20018 San Sebastian, Spain

Hrvoje Petek
Department of Physics and Astronomy, University of Pittsburgh, Pittsburgh, Pennsylvania 15260, USA
and Donostia International Physics Center, P. Manuel de Lardizabal 4, 20018 San Sebastian, Spain

(Received 5 December 2007; revised manuscript received 14 January 2008; published 12 March 2008)

We report the ultrafast dynamics of the 47.4 THz coherent phonons of graphite interacting with a photoinduced nonequilibrium electron-hole plasma. Unlike conventional materials, upon photoexcitation the phonon frequency of graphite upshifts, and within a few picoseconds relaxes to the stationary value. Our first-principles density functional calculations demonstrate that the phonon stiffening stems from the light-induced decoupling of the nonadiabatic electron-phonon interaction by creating a nonequilibrium electron-hole plasma. Time-resolved vibrational spectroscopy provides a window on the ultrafast nonquilibrium electron dynamics.

DOI: 10.1103/PhysRevB.77.121402 PACS number(s): 78.47.−p, 63.20.−e, 81.05.Uw

Graphite possesses highly anisotropic crystal structure, with strong covalent bonding of atoms within and weak van der Waals bonding between the hexagonal symmetry graphene sheets. The layered lattice structure translates to a quasi-two-dimensional (2D) electronic structure, in which the electronic bands disperse linearly near the Fermi level (E_F) and form pointlike Fermi surfaces. The discovery of massless relativistic behavior of quasiparticles at E_F of graphene and graphite has aroused great interest in the nature of carrier transport in these materials.[1–3] Because of the linear dispersion of the electronic bands in graphene, the quasiparticle mass associated with the charge carrier interaction with the periodic crystalline lattice nearly vanishes, leading to extremely high electron mobilities and unusual half-integer quantum Hall effect.[1,2] Since graphite has a quasi-2D band structure very similar to that of graphene, these electronic properties may be expressed also in graphite.

The electron-phonon (*e-p*) interaction contributes to the carrier mass near E_F and limits the high-field transport through the carrier scattering. The strong *e-p* interaction in graphite is a distinctive characteristic of ineffective screening of the Coulomb interaction in semimetals.[4,5] It is expressed in the phonon frequency shift by carrier doping[6] and the strong electronic renormalization of the phonon bands (Kohn anomalies).[7] Time-resolved measurements on the optically generated nonthermal electron-hole (*e-h*) plasma in graphite provide evidence for the carrier thermalization within 0.5 ps both through electron-electron (*e-e*) scattering and optical phonon emission.[8] The nonthermal carriers decay nonuniformly in phase space because of the anisotropic band structure of graphite.[5,9] Quasiparticle correlations in nonthermal plasmas can also be probed from the perspective of the coherent optical phonons. In the present work, through the time-dependent complex self-energy (frequency and lifetime) of the 47 THz E_{2g2} phonon of graphite, we study the transient changes in the *e-p* coupling induced by the optical perturbation of the nonadiabatic Kohn anomaly.

To probe the ultrafast response of the coherent phonons, we perform transient anisotropic reflectivity measurements on a natural single crystal and highly oriented pyrolytic graphite (HOPG) samples. Because the phonon properties were identical, we report the results for HOPG only, whose better surface optical quality gave superior signal-to-noise ratio. The light source for the pump-probe reflectivity measurements is a Ti:sapphire femtosecond laser oscillator with <10 fs pulse duration. The fundamental output is frequency doubled in a β-barium borate crystal to obtain 395 nm excitation light. The 3.14 eV photons excite vertical transitions from the valence (π) to the conduction (π^*) bands near the *K* point. Pump power is varied between 5 and 50 mW (pulse fluence of 0.1−1 mJ/cm), while probe power is kept at 2 mW. Details of the pump-probe measurements are described elsewhere.[10,11] The anisotropic reflectivity change ($\Delta R_{eo}=\Delta R_s-\Delta R_p$) eliminates the mostly isotropic electronic response to isolate the much weaker anisotropic contribution, which is dominated by the coherent phonon response.[10]

Figure 1(a) shows the anisotropic reflectivity change of graphite, $\Delta R_{eo}/R$, normalized to the reflectivity without pump pulse. After a fast and intense electronic response at $t=0$, the reflectivity is modulated at two disparate periods of 21 and 770 fs. The slower coherent oscillation was previously assigned to the Raman active interlayer shear phonon (E_{2g1} mode).[12] The faster oscillation of 47.4 THz or 1580 cm^{-1} is the in-plane E_{2g2} carbon stretching mode[6] corresponding to the *G* peak in the Raman spectra of gra-

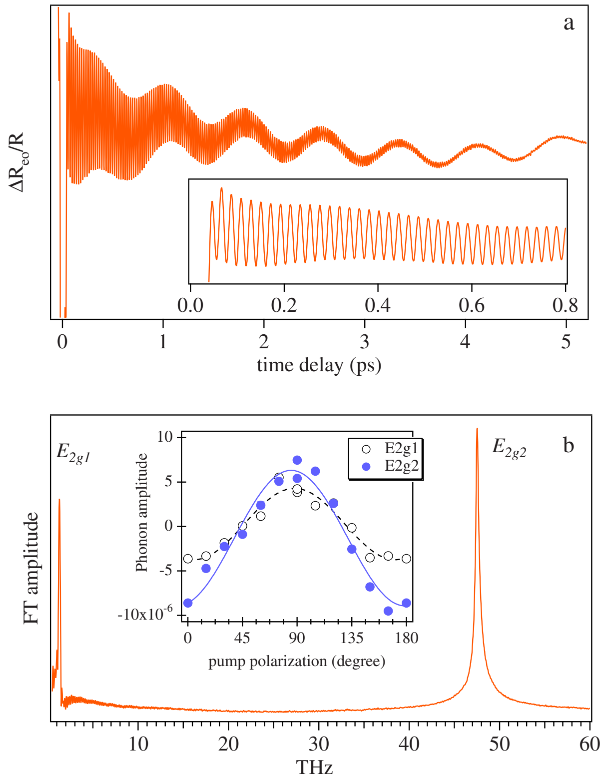

FIG. 1. (Color online) (a) Anisotropic reflectivity change $\Delta R_{eo}/R$ at pump power of 50 mW. The inset shows an enlargement of the trace to show the high-frequency modulation. (b) FT spectrum of the time-domain trace in (a). Inset shows the pump polarization dependence of the amplitudes of the two coherent phonons (A_1 and A_2) obtained from isotropic reflectivity ($\Delta R/R$) measurement. The polarization angle is measured from the plane of incidence. The probe beam is polarized at 90°. Solid and broken curves are fits to $\cos 2\theta$ function.

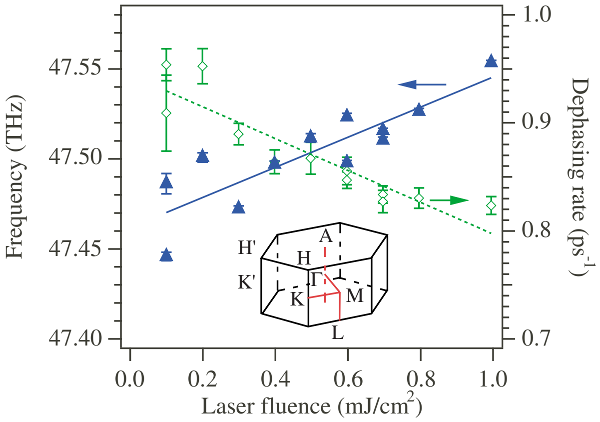

FIG. 2. (Color online) Laser fluence dependence of the dephasing rate Γ_2 and the frequency ω_2 of the coherent E_{2g2} phonon obtained from a fit to an exponentially damped oscillator function. The lines are to guide the eye. Inset shows the Brillouin zone of graphite.

phitic materials. After decay of the electronic response, the reflectivity signal can be fitted approximately to a sum of damped oscillations: $f(t)=A_1\exp(-\Gamma_1 t)\sin(2\pi\omega_1 t+\delta_1)+A_2\exp(-\Gamma_2 t)\sin(2\pi\omega_2 t+\delta_2)$. The amplitudes of both phonons, A_1 and A_2, exhibit a $\cos 2\theta$ dependence on the pump polarization angle θ with respect to the optical plane, as shown in the inset of Fig. 1(b), confirming their generation through the Raman mechanism.[12] Hereafter, we focus on the previously unobserved dynamics of the fast E_{2g2} phonon.

We measure the laser fluence dependence of the amplitude A_2, dephasing rate Γ_2, and frequency ω_2 of the E_{2g2} phonon that are extracted from the fit of $\Delta R_{eo}/R$ to the damped oscillator model. The amplitude increases linearly with the fluence as expected for a π-π^* transition with a single photon. As shown in Fig. 2, the dephasing rate decreases as the laser fluence is increased, which is contrary to the coherent phonon response observed for other materials.[13–15] The frequency upshift at higher fluence in Fig. 2 is equally exceptional. Laser heating can be excluded as the origin because the E_{2g2} frequency downshifts with temperature.[16] In fact, the frequency upshift under intense optical excitation has not been observed experimentally or predicted theoretically for graphite or any other solid.

To further characterize the unexpected frequency upshift, in Fig. 3, we analyze the transient reflectivity response with a time-windowed Fourier transform (FT). This analysis reveals that the phonon frequency blueshift occurs promptly (for delays of <100 fs its dynamics are obscured by the strong electronic response) and recovers to its near-equilibrium value after several picoseconds. With increasing laser fluence, the initial blueshift increases, while the asymptotic value converges on the 47.4 THz Raman frequency. The experimental phonon frequency for $t>100$ fs follows a biexponential recovery, $\omega(t)-\omega(t=\infty)=\Delta\omega_1\exp(-t/\tau_1)+\Delta\omega_2\exp(-t/\tau_2)$, with time constants of $\tau_1=210$ fs and $\tau_2=2.1$ ps, independent of excitation density. The time scales for the recovery are in reasonable agreement with the analysis of transient terahertz spectroscopy, which gave 0.4

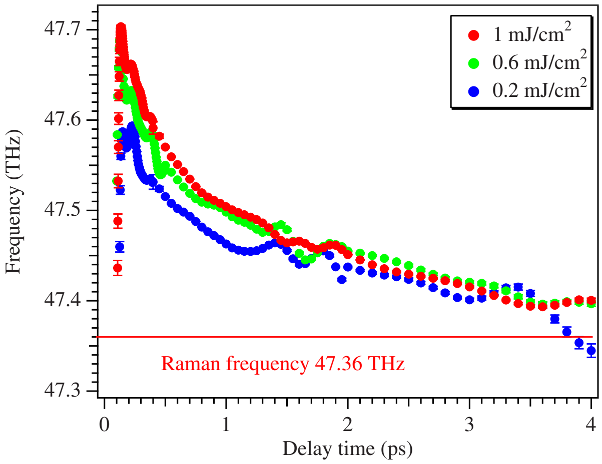

FIG. 3. (Color online) Time evolution of the E_{2g2} phonon frequency, obtained from time-windowed FT, for different laser fluences. The widths of the Gaussian time windows are 80 fs for $t<0.4$ ps, 300 fs for $0.4<t<2$ ps, and 800 fs for $t\geq 2$ ps.

and 4 ps, respectively, for the carrier thermalization and carrier-lattice equilibration.[8] The time evolution of the E_{2g2} frequency implicates the interaction of coherent phonons with the photoexcited nonequilibrium carriers, as will be discussed below.

It is only recently that the observed anomalous dispersion of the high-energy phonon branches of graphite[17] could be explained theoretically by a momentum dependent *e-p* interaction (a Kohn anomaly), which leads to the renormalization (softening) of the phonon frequency.[7] The standard use of the adiabatic approximation in the previous study, however, predicted that perturbing the electronic system by electron doping would result in a downshift of phonons at the Γ point. Recent experiments and theoretical calculations have shown this approach to be inappropriate as the "nonadiabatic" electronic effects, where electrons near E_F cannot respond instantaneously to the lattice distortion, become important for low dimensional materials such as graphene and nanotubes.[18–20]

We perform density-functional theory (DFT) calculations for a single sheet of photoexcited graphite with a computational method that accounts for the nonadiabatic effects. We use DFT in the local-density approximation as implemented in the code ABINIT.[21] Core electrons are described by Trouiller–Martins pseudopotentials and the wave functions are expanded in plane waves with energy cutoff at 35 hartree. Phonons are calculated with density-functional perturbation theory.[22] In order to ensure convergence of the E_{2g2} phonon mode to within 0.01 THz, we use a large 61×61 two-dimensional *k*-point sampling.[23] Nonadiabatic effects are accounted for by keeping the electronic population fixed when computing the dynamical matrix. We neglect the effects of lattice relaxation on the phonon frequency since we checked that the effect of neutral excitation on the bond-length is very weak (<0.001 Å) for the appropriate excitation densities. Our approach is similar to the time-dependent perturbation scheme[18–20] for the inclusion of nonadiabaticity in the combined treatment of phonons and electrons in graphite. Furthermore, it enables us to calculate the effect of an arbitrary electron occupation far from equilibrium such as created by the vertical excitation of *e-h* pairs with 3.1 eV photons. Our calculations demonstrate that nonadiabatic effects are important not only for charged graphite[18–20] but also for graphite with neutral electronic excitation.

Because the photoexcited electron distribution is time dependent and, in principle, not known exactly, we employ three different limiting electronic distributions in our phonon calculation. "As-excited" distribution (AED), corresponding to the vertical excitation of *e-h* pairs with 3.1 eV photons within an energy window of ±0.2 eV, simulates the distribution right after excitation with a laser pulse having a finite spectral width. The laser fluence determines the amount of charge transferred from π to π^* bands. Nonthermal distribution (NTD), in which electrons are completely depopulated in an small energy window from top of the valence band to the bottom of conduction band, mimics the situation after the ultrafast (<100 fs) relaxation of the *e-h* pairs toward E_F by *e-e* (Ref. 9) and *e-p* (Ref. 24) scatterings. The width of the energy window is determined by the excited charge density. Such a distribution has been predicted in a recent microscopic calculation taking into account *e-p* scattering.[24] Because of a hot phonon distribution and a phase-space bottleneck near the *K* points, a Fermi–Dirac distribution with a high electronic temperature is achieved at much later time [0.5 ps (Refs. 8 and 24)]. Hot thermal distribution (TD) simulates this situation after thermalization of the electronic system. To compare with the effect of static doping reported previously,[18–20] we also present calculations with an ionized distribution (ID), in which electrons are removed from the top of the π band.

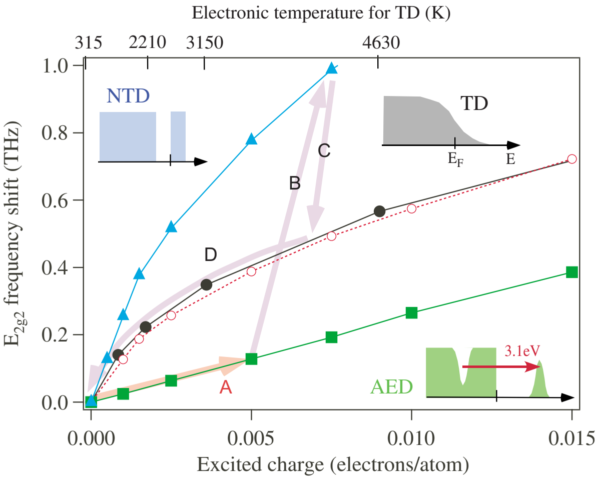

FIG. 4. (Color online) Calculated E_{2g2} frequency change as a function of the excitation charge density for the AED (square), NTD (triangle), TD (filled circle), and ID (open circle). The top axis shows the corresponding electronic temperature T_e for TD. Arrows show schematically the excitation and relaxation pathways for the *e-h* distribution: (A) quasi-instantaneous excitation by a laser pulse, (B) deexcitation within <100 fs through the creation of secondary *e-h* pairs around the Fermi level E_F, (C) thermalization of the *e-h* plasma in ~0.2 ps, and (D) cooling down of the *e-h* plasma in ~2 ps through optical phonon emission. Ultrafast phonon stiffening is ascribed to steps A and B. The highest density excitation (fluence of 1 mJ/cm^2) in our experiment corresponds to 5.8×10^{20} electron-hole pairs/cm^3 or 0.005 electrons/atom.

Figure 4 shows that all the three excited state distributions, as well as the statically doped one, lead to a stiffening of the E_{2g2} phonon. For a fixed density of the excited charge, the closer the *e-h* pairs are to the E_F, the more pronounced is their nonadiabatic interaction with the lattice, and therefore, the stronger is their effect on the phonon stiffening. We note that the stiffening is not accompanied by lattice deformation for the three excited distributions, contrary to the case of ID, for which the lattice both stiffens *and* contracts. The lattice stiffening for ID can be attributed to the depopulation of π orbitals around the *K* and *H* points, which (i) suppresses the nonadiabaticity in the *e-p* coupling and (ii) removes electrons with strong antibonding admixture.[19,18] Because effect (ii) should also lead to a lattice contraction, the C-C bond stiffening under the three excited distributions is attributed to effect (i). This implies that transfer of cold electrons and holes from near the E_F to a hot population causes the stiffening along with the inability of the electronic system to follow the ions adiabatically. In contrast to the static doping studies,[19,18] our observations on a neutral but nonequilibrium system address a phonon frequency shift solely of the electronic origin.

The strong dependence of the phonon stiffening on the *e-h* distribution in Fig. 4 justifies the interpretation of the experimental ultrafast phonon frequency changes in terms of the temporal evolution of the photoexcited *e-h* plasma. Creation of a highly nonthermal electronic population near the K point (arrow A in Fig. 4) weakens the nonadiabatic *e-p* coupling at $t=0$. Within a few tens of femtoseconds, the very efficient *e-e* (Ref. 8) and *e-p* (Ref. 24) scattering first bring the nascent *e-h* distribution toward the K point (arrow B), but still in a nonthermal distribution. The electronic thermalization (arrow C) is realized in about 0.2 ps. This hot-thermal distribution equilibrates with the lattice through optical phonon emission (arrow D) on 2 ps time scale.

In summary, we have explored the influence of the nonequilibrium *e-h* plasma on the femtosecond dynamics of the in-plane E_{2g2} coherent phonon of graphite. The time-dependent phonon frequency probes sensitively the time evolution of the transient electronic occupation distributions. The unusual electronic stiffening of the phonon can be attributed to the excitation-induced reduction of the *e-p* coupling due to quasi-2D electronic structure. The reduced real (frequency) and imaginary (decay rate) parts of the complex self-energy of the *e-p* interaction increase the frequency and reduce the dephasing rate of the E_{2g2} mode. Our results offer a paradigm of *e-p* coupling, where nonequilibrium electrons impart exceptional properties to the lattice. Similar interactions are likely to govern the *e-p* coupling in related graphitic materials, such as carbon nanotubes and graphene, which are of topical interest for high-performance, nanometer scale carbon-based electronic devices.

ACKNOWLEDGMENTS

The authors thank O.V. Misochko for supplying single crystal graphite. Calculations were performed at IDRIS (project 071827), Barcelona Supercomputing Center and UPV/EHU (SGIker Arina). This work is supported by Kakenhi 18340093, the EU Network of Excellence Nanoquanta (NMP4-CT-2004-500198), Spanish MEC (FIS2007-65702-C02-01), French ANR (PJC05–46741), SANES project (NMP4-CT-2006-017310), NSF CHE-0650756, and Ikerbasque.

---

*ishioka.kunie@nims.go.jp

†Present address: Institute of Applied Physics, University of Tsukuba.

[1] K. S. Novoselov, A. K. Geim, S. V. Morozov, D. Jiang, M. I. Katsnelson, I. V. Grigorieva, S. V. Dubonos, and A. A. Firsov, Nature (London) **438**, 197 (2005).

[2] A. K. Geim and K. S. Novoselov, Nat. Mater. **6**, 183 (2007).

[3] T. Ohta, A. Bostwick, T. Seyller, K. Horn, and E. Rotenberg, Science **313**, 951 (2006).

[4] D. P. DiVincenzo and E. J. Mele, Phys. Rev. B **29**, 1685 (1984).

[5] C. D. Spataru, M. A. Cazalilla, A. Rubio, L. X. Benedict, P. M. Echenique, and S. G. Louie, Phys. Rev. Lett. **87**, 246405 (2001).

[6] M. S. Dresselhaus and G. Dresselhaus, in *Light Scattering in Solids III*, Topics in Applied Physics Vol. 51, edited by M. Cardona and G. Güntherodt (Springer, Berlin, 1982), Chap. 2.

[7] S. Piscanec, M. Lazzeri, F. Mauri, A. C. Ferrari, and J. Robertson, Phys. Rev. Lett. **93**, 185503 (2004).

[8] T. Kampfrath, L. Perfetti, F. Schapper, C. Frischkorn, and M. Wolf, Phys. Rev. Lett. **95**, 187403 (2005).

[9] G. Moos, C. Gahl, R. Fasel, M. Wolf, and T. Hertel, Phys. Rev. Lett. **87**, 267402 (2001).

[10] M. Hase, M. Kitajima, A. M. Constantinescu, and H. Petek, Nature (London) **426**, 51 (2003).

[11] K. Ishioka, M. Hase, M. Kitajima, and H. Petek, Appl. Phys. Lett. **89**, 231916 (2006).

[12] T. Mishina, K. Nitta, and Y. Masumoto, Phys. Rev. B **62**, 2908 (2000).

[13] M. Hase, M. Kitajima, S. I. Nakashima, and K. Mizoguchi, Phys. Rev. Lett. **88**, 067401 (2002).

[14] E. D. Murray, D. M. Fritz, J. K. Wahlstrand, S. Fahy, and D. A. Reis, Phys. Rev. B **72**, 060301(R) (2005).

[15] E. S. Zijlstra, L. L. Tatarinova, and M. E. Garcia, Phys. Rev. B **74**, 220301(R) (2006).

[16] P. H. Tan, Y. M. Deng, and Q. Zhao, Phys. Rev. B **58**, 5435 (1998).

[17] J. Maultzsch, S. Reich, C. Thomsen, H. Requardt, and P. Ordejón, Phys. Rev. Lett. **92**, 075501 (2004).

[18] S. Pisana, M. Lazzeri, C. Casiraghi, K. S. Novoselov, A. K. Geim, A. Ferrari, and F. Mauri, Nat. Mater. **6**, 198 (2007).

[19] M. Lazzeri and F. Mauri, Phys. Rev. Lett. **97**, 266407 (2006).

[20] S. Piscanec, M. Lazzeri, J. Robertson, A. C. Ferrari, and F. Mauri, Phys. Rev. B **75**, 035427 (2007).

[21] X. Gonze, J.-M. Beuken, R. Caracas, F. Detraux, M. Fuchs, G.-M. Rignanese, L. Sindic, M. Verstraete, G. Zerah, F. Jollet *et al.*, Comput. Mater. Sci. **25**, 478 (2002).

[22] S. Baroni, S. de Gironcoli, A. D. Corso, and P. Giannozzi, Rev. Mod. Phys. **73**, 515 (2001).

[23] We obtain an absolute value of 47.7 THz for the E_{2g2} mode, which is within 1% of the experimental frequency. Note that in the following, we calculate a shift in the phonon frequency, which is described much more accurately than the absolute value of the frequency.

[24] S. Butscher, F. Milde, M. Hirtschulz, E. Malic, and A. Knorr, Appl. Phys. Lett. **91**, 203103 (2007).

2.6 The quasi-particle band structure of graphite

The full three-dimensional dispersion of the π-bands of graphite was measured through angle-resolved photoemission spectroscopy (ARPES) by the group of T. Pichler (University of Vienna). In collaboration with them, we performed first-principles calculations of the band-structure [30]. The band structure by density-functional theory strongly underestimates the slope of the π-bands and the trigonal warping effect. Fig. 2.6 demonstrates the increase of the π band slope around the high-symmetry point by about 17%, yielding good agreement with the ARPES measurements.

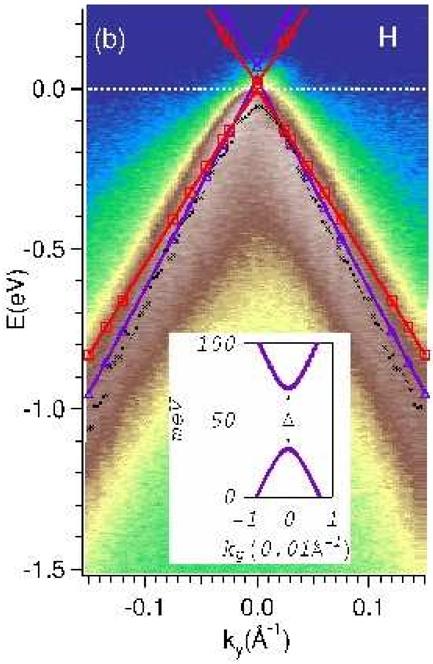

Figure 2.6: ARPES measurement of a two-dimensional cut of the π-band structure of graphite around the high symmetry point H. The maximum of the ARPES intensities is indicated by the black dotted line. Red: LDA band-structure. Violett: GW-quasiparticle band structure. The inset shows the existence of a pseudo-gap at H. Figure reprinted from Ref. [30].

We have fitted the quasi-particle band-structure with a tight-binding Hamiltonian [37]. This fit will be very useful for the description of transport properties of a wide range of carbon materials where the effect of electron correlation cannot be neglected.

Chapter 3

Outlook

Excitonic spectra of large and complex nanostructures

While for nanotubes, *ab-initio* calculations including GW-corrections to the band gap and excitonic effects are feasible, for nanowires of realistic size, the high number of atoms in the unit cell renders the ab-initio approach unfeasible. We are therefore developing a code for the calculation of excitonic effects using the Bethe-Salpeter equation in a tight-binding approximation. As input for the calculations, we first determine the occupied and unoccupied electronic states in the tight-binding approximation. Within this approximation, one can easily construct the matrix elements that enter the Bethe-Salpeter equation, i.e., the two-particle equation which describes the interaction of electrons and holes via a screened Coulomb potential. Due to the large unit-cell size of realistic nanowires (up to several hundred atoms), a large linear eigenvalue problem arises which can be solved quite efficiently with a parallelized Haydock-method, as it is already implemented, e.g. in the optical-properties code `Yambo`[1]. A key ingredient for the construction of the matrix elements is the proper screening of the electron-hole interaction. A calculation of the full static dielectric function may not be accurate enough in the tight-binding framework. We therefore propose the use of a model dielectric function that takes into account the image potentials of the electron and of the hole.[2]

The development of the project has started in the framework of a young researchers' project of the French National Research Agency in collaboration with S. Botti, Ecole Polytechnique. The code will serve for the calculation of the spectra of different nanowires (e.g., Si, Ge, GaAs, GaN) and nanocrystals. It will be interesting to investigate, how the "squeezing" of the excitons as a function of the nanowire radius influences the binding energy as we go from the quasi 3D bulk like environment in a large diameter wire to the quasi 1D limit of very thin wires and to the quasi 0D limit of nanocrystals. Furthermore, we will study the influence of defects such as vacancies, impurity atoms and surface adsorbates (functionalized wires and nanocrystals).

---

[1] A. Marini et al., the `Yambo` project, http://www.yambo-code.org/.

[2] A similar route was chosen recently for the calculation of the binding energy of impurity levels in nanowires: M. Diarra, Y.-M. Niquet, C. Delerue, and G. Allan, Phys. Rev. B **75**, 045301 (2007).

De-excitation of hot carriers in nanostructures

Another topic of fundamental and practical interest is the study of the relaxation of excited (hot) electrons in the conduction band and its radiative versus non-radiative recombination with the holes in the valence band. While these processes are relatively well understood in bulk materials, they can be drastically altered in nanostructures due to the quantum confinement of electrons and holes. A proper description involves the calculation of excitonic states in case of strong electron-hole interaction and of electron-phonon (or, more precisely, exciton-phonon interaction) for the non-radiative relaxation. This subject is the topic of the PhD thesis of Adrien Allard that started in october of this year.

As a first practical application, we will look at lead selenide (PbSe) nanocrystals. Bulk PbSe has a very small gap (280 meV at 300K). Due to quantum confinement effects, this gap can be tuned as a function of the nanocrystal radius. Having evaluated the phonons and the electron-phonon couping in bulk PbSe [39], we will calculate the electron-phonon coupling and the relaxation of hot carriers in the nanocrystals. This is the topic of the PhD thesis of Ondrej Kilian.

Quantum Heterodots

Heterodot is short for nanoscale semiconductor heterojunctions in quantum dots. The internal interface in a heteronanocrystals is characterized by a discontinuity of the electronic structure and an electrical dipole that can lead to complex optical excitations, in particular, excitonic states where the electron is separated from its hole. The project aims at modeling the structural, electronic and optical properties of herodots, working in parallel to experimental investigations, in order to optimize herodot nanomaterials for applications. The objective is to determine the parameters controlling the band alignment, to simulate the optical properties, and to predict the exciton dynamics. Simulations will combine ab initio calculations (band structure, band offsets, excitons) and semiempirical approaches (valence force field methods for strain effects, tight binding methods for optical properties). This work takes place in the framework of a European Network and I am involved through the co-supervision of a PhD thesis.

Graphene/Graphite

Last but not least, there remains a lot of work on the theory of graphene and graphite. Current and future activities include the interpretation of most recent inelastic X-ray measurements[3] which confirm the enhanced electron-phonon coupling that we have calculated in Ref. [34]. A question of high technological relevance is the electron-phonon coupling in charged graphene where the charging may be due to charge fluctuations within a flake [29] or due to backgating. We are currently investigating with the GW-approximation and with DFT using hybrid-functionals, how the electron-phonon coupling changes as a function of the charging. This may explain the observed shift of the Raman 2D line as a function of doping.

---

[3] A. Grüneis, J. Serrano, T. Pichler et al

Appendix A

List of Publications

Publications in refereed journals

[1] L. Wirtz, J.-Z. Tang, and J. Burgdörfer, *Geometry-dependent scattering through ballistic microstructures: Semiclassical theory beyond the stationary-phase approximation*, Phys. Rev. B **56**, 7589 (1997).

[2] J.-Z. Tang, L. Wirtz, J. Burgdörfer, and C. Marcus, *Oscillations in the magnetoconductance autocorrelation function for ballistic microstructures*, Phys. Rev. B **57**, 9875 (1998).

[3] L. Wirtz, J.-Z. Tang, and J. Burgdörfer, *Gauge-invariant theory for semiclassical magnetotransport through ballistic microstructures*, Phys. Rev. B **59**, 2956 (1999).

[4] G. Hayderer, M. Schmid, P. Varga, HP. Winter, F. Aumayr, L. Wirtz, C. Lemell, J. Burgdörfer, L. Hägg, and C. O. Reinhold, *Threshold for potential sputtering of LiF*, Phys. Rev. Lett **83**, 3948 (1999).

[5] K. Tökesi, L. Wirtz, C. Lemell, and J. Burgdörfer, *Charge-state evolution of highly charged ions transmitted through microcapillaries*, Phys. Rev. A **61**, 020901(R) (2000).

[6] L. Wirtz, G. Hayderer, C. Lemell, J. Burgdörfer, L. Hägg, C. O. Reinhold, P. Varga, HP. Winter, and F. Aumayr, *Curve-crossing analysis for potential sputtering of insulators*, Surf. Sci. **451**, 197 (2000).

[7] S. Rotter, J.-Z. Tang, L. Wirtz, J. Trost, and J. Burgdörfer, *Modular recursive Green's function method for ballistic quantum transport*, Phys. Rev. B **62**, 1950 (2000).

[8] G. Hayderer, S. Cernusca, M. Schmid, P. Varga, HP. Winter, F. Aumayr, D. Niemann, V. Hoffmann, N. Stolterfoht, C. Lemell, L. Wirtz, and J. Burgdörfer, *Kinetically assisted potential sputtering of insulators by highly charged ions*, Phys. Rev. Lett. **86**, 3530 (2001).

[9] K. Tökesi, L. Wirtz, C. Lemell, and J. Burgdörfer, *Hollow-Ion formation in microcapillaries*, Phys. Rev. A **64**, 042902 (2001).

[10] L. Wirtz, C. O. Reinhold, C. Lemell, and J. Burgdörfer, *Liouville master equation for multielectron dynamics: Neutralization of highly charged ions near a LiF surface*, Phys. Rev. A **67**, 012903 (2003).

[11] L. Wirtz, C. Stampfer, S. Rotter, and J. Burgdörfer, *Semiclassical theory for transmission through open quantum billiards: Convergence towards quantum transport*, Phys. Rev. E **67**, 016206 (2003).

[12] L. Wirtz, R. Arenal de la Concha, A. Loiseau, and A. Rubio, *Ab initio calculations of the lattice dynamics of BN-nanotubes*, Phys. Rev. B **68**, 045425 (2003).

[13] L. Wirtz, J. Burgdörfer, M. Dallos, T. Müller, and H. Lischka, *Potential energy surfaces for charge exchange between singly charged ions and a LiF surface*, Phys. Rev. A **68**, 032902 (2003).

[14] L. Wirtz and A. Rubio, *Vibrational properties of boron nitride nanotubes: Effects of finite length and bundling*, IEEE Trans. Nanotechn. **2**, 341 (2004).

[15] A. G. Marinopoulos, L. Wirtz, A. Marini, V. Olevano, A. Rubio, and L. Reining, *Optical absorption and electron energy loss spectra of carbon and boron nitride nanotubes: a first principles approach*, Applied Physics A **78**, 1157 (2004).

[16] L. Vitali, M. A. Schneider, K. Kern, L. Wirtz, and A. Rubio, *Phonon and plasmon excitation in inelastic electron tunneling spectroscopy of graphite*, Phys. Rev. B **69**, 121414(R) (2004).

[17] L. Wirtz and A. Rubio, *The phonon dispersion of graphite revisited*, Solid State Commun. **131**, 141 (2004).

[18] G. G. Fuentes, E. Borowiak-Palen, M. Knupfer, T. Pichler, J. Fink, L. Wirtz, and A. Rubio, *Formation and electronic properties of BC3 single-wall nanotubes upon boron substitution of carbon nanotubes*, Phys. Rev. B **69**, 245403 (2004).

[19] L. Wirtz, M. Lazzeri, F. Mauri, and A. Rubio, *Raman spectra of BN-nanotubes: Ab-initio and bond-polarizability model calculations*, Phys. Rev. B **71**, 241402(R) (2005).

[20] C. Stampfer, L. Wirtz, S. Rotter, and J. Burgdörfer, *Pseudo-Path Semiclassical Approximation to Transport through Open Quantum Billiards: Dyson Equation for Diffractive Scattering*, Phys. Rev. E **72**, 036223 (2005).

[21] L. Wirtz, A. Marini, and A. Rubio, *Excitons in boron nitride nanotubes: dimensionality effects*, Phys. Rev. Lett. **96**, 126104 (2006).

[22] R. Arenal, A.C. Ferrari, S. Reich, L. Wirtz, J.-Y. Mevellec, S. Lefrant, A. Rubio, and A. Loiseau, *Raman Spectroscopy of Single-Wall Boron Nitride Nanotubes*, Nano Lett. **6**, 1812 (2006).

[23] D. Graf, F. Molitor, K. Ensslin, C. Stampfer, A. Jungen, C. Hierold, and L. Wirtz, *Spatially Resolved Raman Spectroscopy of Single- and Few-Layer Graphene*, Nano Lett. **7**, 238 (2007).

[24] J. Serrano, A. Bosak, R. Arenal, M. Krisch, K. Watanabe, T. Taniguchi, H. Kanda, A. Rubio, and L. Wirtz, *Vibrational properties of hexagonal boron nitride: Inelastic x-ray scattering and ab-initio calculations* , Phys. Rev. Lett. **98**, 095503 (2007).

[25] D. Graf, F. Molitor, K. Ensslin, C. Stampfer, A. Jungen, C. Hierold, and L. Wirtz, *Raman Imaging of Graphene*, Solid State Commun. **143**, 44 (2007).

[26] A. Grüneis, T. Pichler, H. Shiozawa, C. Attaccalite, L. Wirtz, S.L. Molodtsov, R. Follath, R. Weber, and A. Rubio, *Low energy quasiparticle dispersion of graphite by angle-resolved photoemission spectroscopy*, phys. stat. sol. (b) **244**, 4129 (2007).

[27] C. Attaccalite, L. Wirtz, A. Marini, and A. Rubio, *Absorption of BN nanotubes under the influence of a perpendicular electric field*, phys. stat. sol. (b) **244**, 4288 (2007).

[28] D. Graf, F. Molitor, K. Ensslin, C. Stampfer, A. Jungen, C. Hierold, and L. Wirtz, *Raman mapping of a single-layer to double-layer graphene transition*, Eur. Phys. J. Special Topics **148**, 171 (2007).

[29] C. Stampfer, F. Molitor, D. Graf, K. Ensslin, A. Jungen, C. Hierold, and L. Wirtz, *Raman imaging of doping domains in graphene on* SiO_2, Appl. Phys. Lett. **91**, 241907 (2007).

[30] A. Grüneis, C. Attaccalite, T. Pichler, V. Zabolotnyy, H. Shiozawa, S.L. Molodtsov, D. Inosov, A. Koitzsch, M. Knupfer, J. Schiessling, R. Follath, R. Weber, P. Rudolf, L. Wirtz, and A. Rubio, *Electron-electron correlation in graphite: A combined angle-resolved photoemission and first-principles study*, Phys. Rev. Lett. **100**, 037601 (2008).

[31] K. Ishioka, M. Hase, M. Kitajima, L. Wirtz, A. Rubio, and H. Petek, *Ultrafast electron-phonon decoupling in graphite*, Phys. Rev. B **77**, 121402(R) (2008).

[32] I. Brezinova, C. Stampfer, L. Wirtz, S. Rotter, and J. Burgdörfer, *Diffractive paths for weak localization in quantum billiards*, Phys. Rev. B **77**, 165321 (2008).

[33] L. Wirtz, A. Marini, M. Grüning, C. Attaccalite, G. Kresse, and A. Rubio, *Comment on "Huge excitonic effects in layered hexagonal boron nitride"*, Phys. Rev. Lett. **100**, 189701 (2008).

[34] M. Lazzeri, C. Attaccalite, L. Wirtz, and F. Mauri, *Impact of the electron-electron correlation on phonon dispersions: failure of LDA and GGA functionals in graphene and graphite*, Phys. Rev. B **78**, 081406(R) (2008).

[35] B. Solleder, L. Wirtz, and J. Burgdörfer, *Excitation energy and pair correlation function of trions near an LiF surface*, Phys. Rev. B **78**, 155432 (2008).

[36] F. Aigner, N. Simonović, B. Solleder, L. Wirtz, and J. Burgdörfer, *Suppression of decoherence in fast-atom diffraction at surfaces*, accepted for publication in Phys. Rev. Lett. (2008).

[37] A. Grüneis, C. Attaccalite, L. Wirtz, H. Shiozawa, R. Saito, T. Pichler, and A. Rubio, *Tight-binding description of the quasiparticle dispersion of graphite and few-layer graphene*, accepted for publication in Phys. Rev. B (2008).

Submitted Articles

[38] B. Solleder, L. Wirtz, and J. Burgdörfer, *Vanishing gap in LiF for electronic excitations by slow antiprotons*, submitted to Phys. Rev. B (2008).

[39] O. Kilian, G. Allan, and L. Wirtz, *Ab-initio calculation of the phonon dispersion relations of lead chalcogenides*, submitted to Phys. Rev. B (2008).

Conference Proceedings

[40] K. Tökesi, L. Wirtz, and J. Burgdörfer, *Interaction of highly charged ions with microcapillaries*, Nucl. Instrum. Meth. B **154**, 307 (1999).

[41] G. Hayderer, C. Lemell, L. Wirtz, M. Schmid, J. Burgdörfer, P. Varga, HP. Winter, and F. Aumayr, *Observation of a threshold in potential sputtering of LiF surfaces*, Nucl. Instrum. Meth. B **164**, 517 (2000).

[42] K. Tökesi, L. Wirtz, C. Lemell, and J. Burgdörfer, *Transmission of highly charged ions through microcapillaries*, Nucl. Instrum. Meth. B **164**, 504 (2000).

[43] L. Wirtz, C. Lemell, C. O. Reinhold, L. Hägg, and J. Burgdörfer, *Vertical incidence of slow Ne^{10+} ions on a LiF surface: suppression of the trampoline effect*, Nucl. Instrum. Meth. B **82**, 36 (2001).

[44] K. Tökesi, L. Wirtz, C. Lemell, and J. Burgdörfer, *Angular distribution of highly charged ions transmitted through metallic microcapillaries*, J. Electron Spectrosc. Relat. Phenom. **195**, 129 (2003).

[45] T. Pichler, E. Borowiak-Palen, G. G. Fuentes, M. Knupfer, A. Graff, J. Fink, L. Wirtz, and A. Rubio, *Electronic structure and optical properties of boron doped single-wall carbon nanotubes*, AIP conf. proceed. **685**, 361 (2003).

[46] R. Arenal de la Concha, L. Wirtz, J.-Y. Mevellec, S. Lefrant, A. Rubio, and A. Loiseau, *Raman spectroscopy of single-wall BN nanotubes*, AIP conf. proceed. **685**, 384 (2003).

[47] L. Wirtz and A. Rubio, *Band structure of boron doped carbon nanotubes*, AIP conf. proceed. **685**, 402 (2003); cond-mat/0311169.

[48] L. Wirtz, V. Olevano, A. G. Marinopoulos, L. Reining, and A. Rubio, *Optical absorption in small BN and C nanotubes*, AIP conf. proceed. **685**, 406 (2003); cond-mat/0311171.

[49] J. Burgdörfer, L. Wirtz, C. O. Reinhold, and C. Lemell, *Multi-electron dynamics for neutralization of highly charged ions near surfaces*, Vacuum **73**, 3 (2004).

[50] L. Wirtz, M. Dallos, H. Lischka, and J. Burgdörfer, *Ab-initio calculations of charge exchange in ion-surface collisions: an embedded-cluster approach*, In "Correlation Spectroscopy of Surfaces, Thin Films, and Nanostructures", J. Berakdar and J. Kirschner (Eds.), Wiley-VCH, Weinheim, 2004.

[51] L. Wirtz, A. Marini, and A. Rubio, *Optical Absorption of Hexagonal Boron Nitride and BN Nanotubes*, AIP Conf. Proc. **786**, 391 (2005).

[52] C. Lemell, X.-M. Tong, K. Tökesi, L. Wirtz, J. Burgdörfer, *Electron emission from surfaces induced by HCI and lasers*, Nucl. Instrum. Meth. B **235**, 425 (2005).

[53] J. Burgdörfer, C. Lemell, K. Schiessl, B. Solleder, C. Reinhold, K. Tökesi, and L. Wirtz, *Collisions of Slow Highly Charged Ions with Surfaces*, in *Proceedings of ICPEAC XXIV* (World Scientific, Singapore, 2006), arXiv:physics/0605245.

Book chapters

[54] L. Wirtz and A. Rubio, *Optical and vibrational properties of boron nitride nanotubes*, in *B-C-N Nanotubes and Related Nanostructures*, edited by Y.K. Yap, Springer (in press)

Invited talks at international workshops/conferences

- *Charge Exchange and Potential Sputtering during Impact of Slow Ions on a LiF Surface*, XIII. IISC (international workshop on ion-surface collisions), San Carlos de Bariloche, Argentina, 11/2000.
- *Interaction of highly and singly charged ions with an LiF surface*, XVII. ISIAC, (International seminar on ion-atom collisions), Tijuana, Mexico, 07/2001.
- *Raman and Infrared Active Modes of BN-nanotubes*, NT'02 (International Conference on the Science and Application of Nanotubes), Boston, USA, 07/2002. ("poster++" presentation).
- *Optical and vibrational properties of BN nanotubes*, SPIE International Symposion on "Microtechnologies for the New Millennium", Gran Canaria, Spain, 05/2003.
- *Transport through quantum billiards: a model system for ballistic transport in molecules*, CECAM-ESF/Psi-k workshop on Electronic Transport in Molecular Systems, Lyon, France, 06/2003.
- *Theory of BN-Nanotube Spectroscopy*, 305. WE-Heraeus Seminar "Carbon-Nanotubes", Bad Honnef, Germany, 11/2003.
- *Excitons in BN-nanotubes: dimensionality effects*, NANOEXC 2004, Workshop on Theory and Modeling of Electronic Excitations in Nanoscience, Maratea, Italy, 09/2004.
- *Optical Absorption of Hexagonal Boron Nitride and BN nanotubes*, IWEPNM (International Winterschool on Electronic Properties of Novel Materials), Kirchberg, Austria, 03/2005.
- *Electronic excitations in hexagonal layered systems: C and BN*, 2nd International School and Workshop on Time-Dependent Density Functional Theory, Benasque, Spain, 09/2006.

- *Optical Properties of BN Nanotubes and Hexagonal BN - Role of Defects*, MRS Fall Meeting, Boston, USA, 11/2007.

Appendix B

Curriculum Vitae of Ludger Wirtz

Birth: 24/04/1971 in Immerath (Germany)
Nationality: German
Marital status: married, 2 children

Home address: 41 rue Paul Blondeau, 59700 Marcq-en-Baroeul, France
Work address: IEMN, B.P. 60069, 59652 Villeneuve d'Ascq Cedex, France
Tel.: 0033 3 20 19 79 12
E-mail: Ludger.Wirtz@isen.iemn.univ-lille1.fr

Pre-University

05/1990	"Abitur" (High-school graduation)
07/1990 - 09/1991	Civil service

University studies

10/1991 - 07/1994	Student of physics at Bonn University, Germany
08/1994 - 05/1995	Exchange student at the University of Tennessee, Knoxville, USA
06/1995 - 06/1996	Research assistant at the Department of Physics and Astronomy, University of Tennessee, USA
08/1996 - 07/1997	Student of physics at Bonn University, Germany
10/1997 - 10/2001	PhD student in the group of J. Burgdörfer at the Institute for Theoretical Physics, Vienna University of Technology, Austria

Scholarship of the "Studienstiftung des Deutschen Volkes" (1991 - 1997).

Academic Degrees

Diplom-Physiker, Bonn University, 01/07/1997
Master's thesis: *Semiclassical scattering in mesoscopic ballistic semiconductor structures*
Supervisors: W. Sandhas (Bonn University), J. Burgdörfer (University of Tennessee)
Grade: "Sehr gut".

Doctor of natural sciences (Dr. rer. nat.), Vienna University of Technology, 10/10/2001
PhD thesis: *Interaction of Singly and Multiply Charged Ions with a Lithium-Fluoride Surface*
Supervisor: J. Burgdörfer
Grade: "Mit Auszeichnung".

Academic positions

03/2002 - 09/2004	Postdoc in the group of A. Rubio at the Donostia International Physics Center, University of the Basque Country, San Sebastián, Spain.
Since 10/2004	Chargé de Recherche CNRS, Commission 6 : Matière condensée, structures et propriétés électroniques, IEMN, Université Lille 1, France.

Research areas

- Optical properties of nanostructured materials
- Theory of ion-surface collisions
- Transport in mesoscopic systems ("quantum billiards")

Teaching

- Vienna University of Technology, 1999/2000: Exercises in Statistical Physics and Thermodynamics
- ISEN (Institut supérieur de l'Electronique et du Numérique) Lille, since 2005 : Exercises in Quantum mechanics and semiconductor physics (3rd and 4th year engineering studies).
- ISEN, 2005-2007 : Supervision of research projects (4th year engineering studies).

Research supervision

Co-supervision of Master's projects

- Stefan ROTTER (1998-1999), Vienna University of Technology
  Modular recursive Green's function method for quantum transport
  (see publ. [7]).

- Christoph STAMPFER (2002-2003), Vienna University of Technology
  Semiclassical theory for ballistic transport through semiconductor microstructures
  (see publ. [11,20]).

Supervision of Master's projects

- Ondrej KILIAN (2006), Université Lille 1
  Calcul ab-initio des phonons dans les chalcogénures de plomb
  (see publ. [38]).
- Adrien ALLARD (2008), Université Lille 1
  Phonons du graphène déposé sur un substrat de Nickel.

Co-supervision of PhD theses

- Beate SOLLEDER (2005-2008), Vienna University of Technology
  Classical and Quantum Simulations of Ion-Surface Interaction
  (see publ. [35,36,38]).
- Ondrej KILIAN (2007-2010), co-tutelle Comenius University Bratislava/ Univ. Lille 1
  Theoretical study of the optical and vibrational properties of lead chalcogenide nanocrystals (provisional title).
- Adrien ALLARD (2008-2011), Université Lille 1
  De-excitation of hot carriers in semiconductor nanocrystals (provisional title).

Postdocs

- Claudio ATTACCALITE (2006-2007), IEMN
  work on optical properties of defects in boron nitride [27,33] and on quasiparticle bandstructure [26,30,37] and phonons [34] in graphene.

Research contracts - Funding

- ANR (French National Research Agency): Young-researchers project CPONN (Calculation of optical properties of nanotubes and nanowires), 2006-2008, 140000 Euros, principal investigator.
- PHC Amadeus (French-Austrian exchange programme): "Ab-initio calculation of charge exchange during ion-surface collisions", 2007-2008, 5000 Euros, principal investigator.
- NANOQUANTA European Network of Excellence (6th framework programme), 2004-2008, associate member.
- ETSF (European Theoretical Spectroscopy Facility), I3 European network (7th framework programme), 2008-2012, leader of a working team within the ETSF.

Other activities

- Evaluator for the PNANO programme of the French National Research Agency (ANR).
- Refereeing: Physical Review Letters, Physical Review B, Nanotechnology, European Physical Journal B
- Coorganization of the annual international NANOQUANTA/ETSF workshop on electronic excitations", 2006 - 2010.